Department of Physics and Astronomy

University of Heidelberg

Master thesis

in Physics

submitted by

Marius Wilm Menzel

born in Bad Segeberg (Germany)

2023

Energy-straggling analysis of the Digital Pixel Test Structure, a MAPS prototype produced in 65 nm TPSCo CMOS technology towards ALICE ITS3

This Master thesis has been carried out by

Marius Wilm Menzel

at the

Physikalisches Institut in Heidelberg

under the supervision of

Prof. Dr. Silvia Masciocchi

Abstract

The planned upgrade of the ALICE Inner Tracking System (ITS3) aims at utilizing wafer-scale Monolithic Active Pixel Sensors (MAPS), thinned down to 20 - 40 μm and bent to form truly cylindrical half-barrels. For its realization, the feasibility of employing the novel 65 nm TPSCo technology is studied in an extensive R&D program, covering laboratory and in-beam tests. Among the first prototypes of this new technology is the Digital Pixel Test Structure (DPTS), which is the subject of this thesis. The sensor features an asynchronous readout, time-encoding hit-position and Time-over-Threshold (ToT) information on a single output line. Within this work, an algorithm was developed enabling the ToT extraction on the DPTS for clusters composed of multiple firing pixels. It features a correction of possible hit-position decoding errors, increasing the total fraction of well-extracted ToTs from about 80 to 90 % for $^{55}_{26}$Fe data and from about 60 to 70 % for in-beam data. More importantly, the correction increases the relative fraction of well-extracted ToTs per cluster-size ≥ 2 significantly, leading to more representative cluster-size distributions. The radiation hardness of the technology, assessed by the $^{55}_{26}$Fe response up to a non-ionizing dose of 10^{15} 1MeV $\mathrm{n}_{eq}\,\mathrm{cm}^{-2}$ at a temperature of 20° C, is demonstrated. Energy-straggling distributions, obtained from a data set of in-beam ToT spectra, are utilized to underline the radiation hardness under the aforementioned conditions. Finally, the active layer thickness Δ_{act} of the DPTS is estimated to be $10.5^{+1.2}_{-1.2}\,\mu$m, using in-beam data taken at CERN's Proton Synchrotron. Additionally, employing sensors under inclined illumination, Δ_{act} was independently estimated to be $10.1 \pm 0.6\,\mu$m at DESY II. Both methods agree within one standard deviation.

Zusammenfassung

Das geplante Upgrade des ALICE Inner Tracking Systems (ITS3) zielt auf die Verwendung von Monolithischen Aktiven Pixel Sensoren (MAPS) ab, die auf 20 - 40 μm gedünnt und zu zylindrischen Halbschalen gebogen werden. Hierfür wird der Einsatz der neuartigen 65 nm TPSCo Technologie in einem umfangreichen F&E-Programm untersucht, das Labor- und Strahltests umfasst. Die Digitale Pixel Test Struktur (DPTS) zählt zu den ersten Prototypen dieser Technologie und ist Gegenstand der vorliegenden Arbeit. Der Sensor verfügt über eine asynchrone Datenauslese, die Informationen über die Trefferposition und der Signalzeit über der Schwelle (ToT) auf einer einzigen Ausgangsleitung vereint. Im Rahmen dieser Arbeit wurde ein Algorithmus entwickelt, der die ToT-Extraktion auf der DPTS für Cluster ermöglicht, die aus mehreren aktivierten Pixeln bestehen. Er beinhaltet eine Korrektur möglicher Fehler in der Positionsdekodierung, wodurch sich der Anteil der extrahierten ToTs für $^{55}_{26}$Fe-Daten von ca. 80 auf 90 % und für Strahldaten von ca. 60 auf 70 % erhöht. Die Korrektur erhöht zudem den relativen Anteil extrahierter ToTs pro Clustergröße ≥ 2 signifikant, was zu repräsentativeren Clustergrößenverteilungen führt. Die Strahlungshärte in Bezug auf die $^{55}_{26}$Fe-Antwort bis zu einer Dosis von 10^{15} 1MeV $\mathrm{n}_{eq}\,\mathrm{cm}^{-2}$ bei einer Temperatur von 20 °C wird demonstriert. Es werden Energieverteilungen aus ToT-Spektren eines im Strahl aufgenommenen Datensatzes bestimmt, um die Strahlungshärte unter den genannten Bedingungen zu verdeutlichen. Schließlich wird die Dicke der aktiven Schicht Δ_{act} der DPTS anhand von Strahldaten, die am Protonen-Synchrotron des CERN aufgenommen wurden, auf $10.5^{+1.2}_{-1.2}\,\mu$m abgeschätzt. Zusätzlich wurde Δ_{act} am DESY II, unter Verwendung von schräg illuminierten Sensoren auf $10.1 \pm 0.6\,\mu$m geschätzt. Beide Methoden stimmen innerhalb von einer Standardabweichung überein.

Contents

1 Introduction

Quantum Chromodynamics (QCD) is the theory describing the fundamental strong interaction between quarks mediated by gluons. Arising from a unique property of the strong force, i.e. the reduction of its coupling strength with increasing energy scale, distinct phases of strongly interacting matter are predicted. So far, one way of experimentally probing the resulting QCD phase diagram is through nucleus-nucleus interactions such as those available in the Large Hadron Collider (LHC) at the Conseil Européen pour la Recherche Nucléaire (CERN). At the LHC, the dedicated experiment is 'A Large Ion Collider Experiment' (ALICE). Its design is optimized to study the properties of quark-gluon plasma (QGP), a state of strongly interacting matter formed at very high energy densities. Since the QGP is believed to have existed up to $10\,\mu$s after the Big Bang [1], it is not only of interest in terms of High-Energy-Physics (HEP) but also in terms of cosmology. A brief introduction of the underlying physics and the ALICE experiment is given in Sections 2.1 and 2.2.

The innermost subdetector of the experiment is the Inner Tracking System (ITS), which is responsible for a precise reconstruction of primary and secondary decay vertices arising from the collision. During the next long shutdown period of the LHC (LS3), the currently installed ITS2 will be upgraded to the ITS3. The upgrade aims at replacing the three innermost tracking layers with ultra-thin, wafer-scale and truly cylindrical Monolithic Active Pixel Sensors (MAPS). This aims at reducing the material budget per layer below $0.05\,\%X_0$ with a more homogeneous distribution over the azimuth. Additionally, the innermost tracking layer will be brought about 5 mm closer to the interaction point. With the aforementioned advancements, the tracking efficiency and pointing resolution can be improved significantly, especially for low transverse momenta. In particular, this will be advantageous for the study of heavy-flavour hadrons and low-mass dileptons. An overview of the ITS2 and the planned upgrade to the ITS3 is given in Sections 2.3 and 2.4.

One of the first crucial steps towards the ITS3 upgrade is validating the feasibility of employing the novel 65 nm TPSCo technology. This can be accomplished with laboratory and in-beam characterization studies. One of the prototypes of the first submission in this technology is the Digital Pixel Test Structure (DPTS). It hosts 32×32 pixels with a $15\times15\,\mu\mathrm{m}^2$ pitch. It features an asynchronous readout, which time-encodes the hit position and Time-over-Threshold (ToT) information on a single output line. In Chapter 3 of this thesis, a brief introduction to the underlying principles of Monolithic Active Pixel Sensors (MAPS) is provided, followed by a description of the main characteristics and functionalities of the DPTS. Additionally, an algorithm allowing for the ToT extraction of multi-pixel clusters (i.e. events involving more than one pixel firing) is introduced.

To relate the DPTS's ToT response to the collected charge, an energy calibration of the device can be performed. For this, the well-known characteristic emissions of an $^{55}_{26}\mathrm{Fe}$ source are utilized. A calibration is performed on an exemplary data set, demonstrating the linearity of the DPTS's frontend in the energy regime of the $^{55}_{26}$Fe emissions. Afterwards, a simplified calibration method is introduced, using only the dominant K_α emission. It agrees with the aforementioned method.

To demonstrate the technology's radiation hardness, the $^{55}_{26}$Fe response of a non-irradiated device is compared to the one of an irradiated device, which was exposed to a dose of 10^{15} $1\mathrm{MeV}\,\mathrm{n}_{eq}\,\mathrm{cm}^{-2}$ Non Ionizing Energy Loss (NIEL). At this irradiation level, the K_α emission of the source is still resolvable and thus, the sensor can still be energy-calibrated. The corresponding analysis can be found in Chapter 4.

With in-beam tests, the technology's performance can not only be studied in terms of tracking efficiency and spatial resolution but also in terms of charge collection. Since the energy deposition by a charged particle in the active layer of the sensor underlies a statistical process, it can not be predicted particle-by-particle. This fluctuation of the deposited energy is especially noticeable for very thin detection layers, such as silicon pixel sensors. This fluctuation is referred to as energy-straggling and leads to a certain distribution of the collected charge in response to a mono-energetic beam. In Section 5.2, different models of the energy-straggling with different application ranges in terms of the absorber thickness are discussed. To obtain the in-beam energy straggling distributions from the ToT spectra of the DPTS, a dedicated analysis chain was developed. This analysis utilizes the aforementioned ToT-energy calibration, which was performed with $^{55}_{26}$Fe spectra recorded in the same operational conditions as during the in-beam test. For an exemplary data set recorded at CERN's Proton Synchrotron in a 10 GeV positive hadron beam, the analysis chain is explained in Section 5.3.

Moreover, a non-irradiated and a NIEL irradiated device are compared in terms of their energy-straggling distributions at a temperature of $20\,°C$. This further underlines the radiation hardness of the technology up to 10^{15} $1\mathrm{MeV}\,\mathrm{n}_{eq}\,\mathrm{cm}^{-2}$. By fitting the energy-straggling distributions, the most probable value (MPV) of the energy loss in the sensor can be determined. It is used in Section 5.5 to obtain an estimation of the active layer thickness.

The MPV of the energy-straggling is expected to increase with the thickness of the active layer. This behaviour is demonstrated by inclining the DPTS with respect to the beam. Thereby, the traversing length of the beam particles through the active layer can be increased, imitating a larger active layer thickness. Using the geometrical expectation for the MPV shift with the illumination angle, the dependency is fitted treating the active layer thickness as a free parameter. This way, an additional estimation of the active layer thickness is obtained, validating the aforementioned result. The analysis corresponding to the inclined illumination of the DPTS can be found in Section 5.6.

2 The ALICE Experiment

The ALICE detector ('A Large Ion Collider Experiment') is a High Energy Physics (HEP) experiment located at Point 2 of the Large Hadron Collider (LHC) at the Conseil Européen pour la Recherche Nucléaire (CERN). It is designed to address the fundamental physics of strongly interacting matter using proton-proton, proton-nucleus, and nucleus-nucleus collisions. The following sections provide a brief outline of the main physics program and the general detector layout of ALICE. Furthermore, the Inner Tracking System and its foreseen upgrade towards Run 4 of the LHC will be discussed in more detail.

2.1 Physics Program

The aim of the ALICE detector is to study Quantum Chromodynamics (QCD), which is the theory describing the strong interaction within the Standard Model. Its study at high energy densities is the experiment's main objective [2]. The following Sections briefly introduce QCD as the current theory of strongly interacting matter. Emerging from the most important quantities of QCD, its phase diagram will be introduced and described. Furthermore, the formation of quark-gluon plasma in ultra-relativistic heavy-ion collisions will be briefly explained.

2.1.1 Quantum Chromodynamics

The Standard Model of Particle Physics (SM) [3] describes the current understanding of elementary particles and the fundamental forces interacting between them, with the exception of gravity. It comprises three generations of spin-half fermions, four integer spin gauge bosons, and the spin-zero Higgs boson. The fermions further divide into quarks and leptons, which come in six flavours each. Additionally, for each fermion, there is an antiparticle which carries opposite generalized charges. Each force described by the SM is described by a dedicated Quantum Field Theory (QFT).

The relativistic QFT of the strong interaction is the theory of Quantum Chromodynamics [3, 4]. The strong interaction is invariant under local SU(3) phase transformations. The corresponding eight generators $\hat{T}_a$ of the symmetry group are associated with eight gluons, the mediators of the strong interaction. QCD comes with one conserved charge, which can take six colour states: 'green', 'red', 'blue', or one of the corresponding anti-colours. While quarks can solely have a single colour, gluons carry, due to colour conversation at QCD vertices, a colour, and an anti-colour.

The Lagrangian density of QCD is defined as:

$$\mathscr{L}_{QCD} = \bar{q}_i^f (i\gamma_\mu \not{D}_{ij}^\mu - m_f \delta_{ij}) q_j^f - \frac{1}{4} G_a^{\mu\nu} G_{\mu\nu}^a \tag{1}$$

Here, q_i^f represents the quark field with color charge i, flavor f and mass m_f. The first term of Equation 1, known as the Dirac term, describes the dynamics of the quark fields. Here, the covariant derivative $\not{D}_{ij}^\mu$ is given through:

$$\not{D}_{ij}^\mu = \delta_{ij}\partial^\mu + ig_s \hat{T}_{ij}^a G_a^\mu \tag{2}$$

The derivative denotes the coupling between the gluon field G_a^μ and quarks with coupling strength g_s. The second term of Equation 1 is related to the dynamics of the gluon fields. Here the gluon field strength tensor $G_{\mu\nu}^a$ is given by:

$$G_{\mu\nu}^a = \partial_\mu G_\nu^a - \partial_\nu G_\mu^a + ig_s f_{abc} G_\mu^b G_\nu^c \tag{3}$$

Since $[\hat{T}^a, \hat{T}^b] = if_{abc}\hat{T}^b \neq 0$, QCD is considered a non-abelian gauge theory. Thus, gluon-gluon self-interactions are possible and described with the last term of Equation 3. Arising from the SU(3) group structure, the strong coupling constant α_s is dependent on the momentum transfer Q^2 of a strong interaction. From this dependency, two unique properties of QCD emerge: asymptotic freedom and confinement.

Confinement arises at low values of the momentum transfer Q^2 in hadron-hadron interactions in the order of 1 GeV. Here, the coupling strength α_s of the strong interaction reaches $\alpha_s \sim 1$, leading to confinement. In this regime, quarks and gluons are bound into hadronic states. At higher momentum transfers of $|Q| \sim 100$ GeV, the coupling is in the order of $\alpha_s \sim 0.1$, allowing to treat a QCD system as a group of asymptotical free particles and to apply perturbation theory.

2.1.2 Quark-Gluon Plasma

In consequence of the Q^2 dependence of α_s described in Section 2.1.1, distinct phases of strongly interacting matter are expected as sketched in the QCD phase diagram shown in Figure 1. Ordinary hadronic matter is located at low temperatures T and low baryon densities. Here, quarks and gluons are confined in colour-neutral hadrons. For very high energy densities in the order of 1-2 GeV/fm^3 [5], quarks are expected to become deconfined and can propagate freely over distances larger than the size of a nucleus. This state of strongly interacting matter is called quark-gluon plasma (QGP) [5]. The extreme case of low temperatures and very high baryon densities is believed to exist in the core of neutron stars [6].

According to the current understanding, it is assumed that QGP lasted about 10 μs [7] after the Big Bang. This makes the study of the QGP properties not only interesting for HEP but also in terms of cosmology. So far, the only way to access QGP experimentally is through nucleus-nucleus collisions. Currently, the only experiments probing the QCD phase diagram at lower baryon densities towards high temperatures are located at the LHC and the Super-Proton-Synchrotron (SPS) at CERN, and the Relativistic Heavy Ion Collider at Brookhaven National Laboratory (BNL).

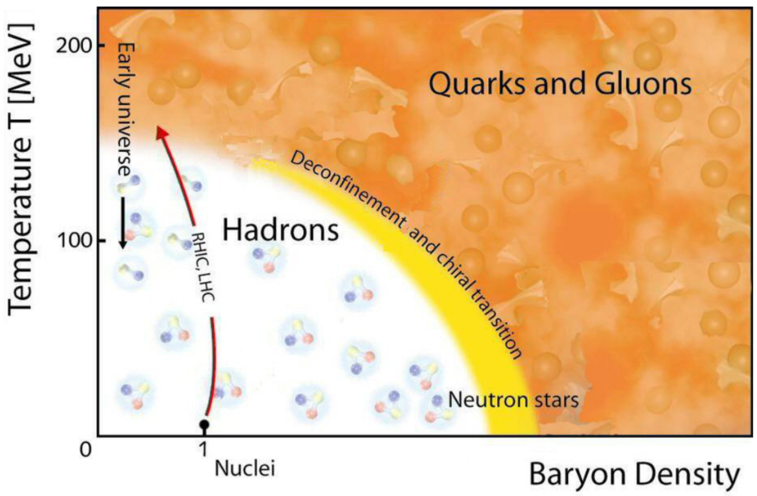

Figure 1: Illustration of the phase diagram of strongly interacting matter. Taken from [8].

2.1.3 QGP Signatures in Heavy-Ion Collisions

After an ultra-relativistic collision of heavy ions, e.g. Pb-Pb in the LHC, the resulting system undergoes a characteristic evolution, commonly subdivided into different stages. The first one is referred to as 'pre-equilibrium'. Here, partons are scattered in hard processes and the system thermalizes. Due to the high energy densities within the system, a QGP is created. This 'QGP phase' can be macroscopically described utilizing the theoretical framework of relativistic fluid dynamics. While expanding, the system cools down. Below a critical temperature, the system enters a 'hadronization phase'. Here, a hadron gas is formed. Thermal equilibrium is still maintained by inelastic collisions. Afterwards, in the 'chemical freeze-out' phase, these inelastic collisions terminate. From this point, relative hadron abundances are fixed. Finally, also the elastic collisions come to an end. This phase is referred to as 'kinetic freeze-out'. From here, the momentum spectrum of the system's constituents is fixed, and they freely move away from the interaction point.

In order to characterize the system produced in heavy-ion collisions as a state of matter, it is necessary to determine its parameters, such as temperature, chemical potential, flow velocity and equation of state. The parameters can be inferred from a wide variety of experimentally accessible observables, which can help to disentangle the different physical mechanisms that characterize the various collision stages.

2.2 Detector Layout

The ALICE detector comprises a central barrel dedicated to hadron, electron and photon measurement and a forward muon arm. The experiment contains several subdetectors, as shown in Figure 2. The central barrel is situated in a 0.5 T solenoid magnet and covers a polar angle between 45° and 135°, while the muon arm covers angles between 171° and 178° [2]. From the interaction point outwards in radial direction, the central barrel consists of the Inner Tracking System (ITS), described in detail in Section 2.3, a cylindrical Time Projection chamber (TPC), providing additional tracking and Particle Identification (PID) information, a Time-of-Flight (TOF), a Ring-Image-Cherenkov (HMPID) and Transition Radiation Detector (TRD) for further PID, and two electromagnetic calorimeters (PHOS and EMCaL). The Muon spectrometer (MFT, MCH & MID) is designed to provide acceptance for particles with transverse momentum close to zero. It consists of a dipole magnet and several tracking plates and triggering chambers. For global event characterization and tracking, several smaller detectors are utilized (AD, ZDC, V0+, T0+A, T0+C). The ACORDE detector on top of the solenoid magnet is responsible for triggering on cosmic rays.

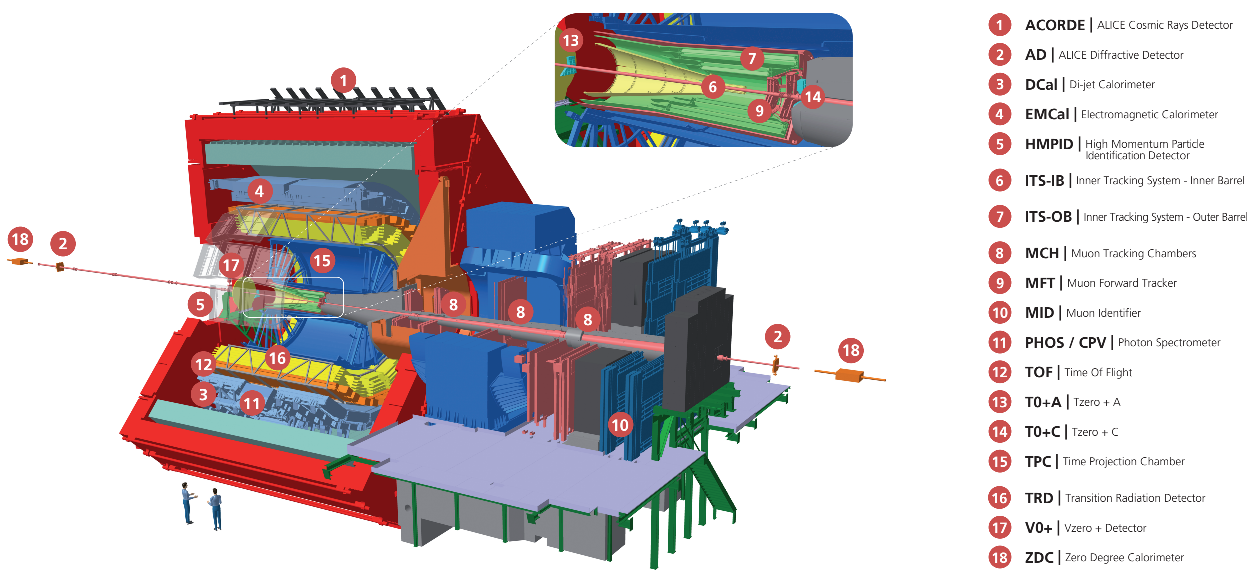

Figure 2: Detector layout of ALICE. Taken from [9].

2.3 Inner Tracking System

The Inner Tracking System (ITS) is the innermost detector of the ALICE experiment and an essential element of its physics program. It is responsible for a precise reconstruction of primary and secondary interaction vertices, a high detection efficiency, and a fast readout at high interaction rates [10]. The following Sections provide an overview of the currently installed detector and briefly discuss its key features.

2.3.1 ITS2 Layout

The during the Long Shutdown 2 installed upgrade of the Inner Tracking System (ITS2) [10, 11], illustrated in Figure 3, consists of seven layers of ALPIDE Monolithic Active Pixel Sensors (MAPS), arranged concentrically around the LHC beam pipe. The innermost three layers form the Inner Barrel (IB), while the outer four layers are referred to as the Outer Barrel (OB). With an active surface of $10\,\mathrm{m}^2$ and 12.5 GPix, the ITS2 is the largest silicon pixel detector ever built. In order to meet the requirements for ALICE in LHC Run 3, the material budget of the ITS was reduced from $1.14\,\%\,\mathrm{X}_0$ to $0.36\,\%\,\mathrm{X}_0$ per layer for the IB and maintained a low level of around $1.0\,\%\,\mathrm{X}_0$ per layer for the OB. Further, the innermost tracking layer was moved about 17 mm closer to the beam line leading to a higher vertex resolution. The pixel granularity was increased to $30 \times 30\,\mu$m while introducing an additional tracking layer compared to the ITS, increasing the tracking efficiency at low transverse momenta. Moreover, the rate capability of the system was raised by two orders of magnitude from 1 kHz to 100 kHz for Pb-Pb collisions.

Each layer is segmented in the azimuthal direction into functionally independent units, called Staves. As depicted in Figure 4, a Stave of the IB consists of the following major components: a lightweight carbon fibre support structure (Space Frame), a thermally conductive carbon plate with embedded water cooling pipes (Cold Plate), a layer of ALPIDE pixel sensors (see Section 2.3.2), and a Flex Printed Circuit hosting readout, control, and power supply of the sensors bonded to it. Also, a separate Power Bus is attached for supplying the modules with the necessary voltages. The Staves are, as shown in Figure 3, placed concentrically around the beam pipe. To ensure full coverage of the azimuth, the sensors need to be placed such that the active areas of the Staves overlap slightly.

2.3.2 The ALICE Pixel Detector

The sensor type used in the ITS2 is the ALICE PIxel DEtector (ALPIDE) [12]. It is a Complementary Metal Oxide Semiconductor (CMOS) Monolithic Active Pixel Sensor (MAPS) (see Section 3.1.3) fabricated in 180 nm TowerJazz technology [13]. The sensor's dimensions are $1.5\,\mathrm{cm} \times 3\,\mathrm{cm}$ hosting 512×1024 pixel with a pitch of $26.88\,\mu\mathrm{m} \times 29.24\,\mu\mathrm{m}$ each. Its hit-based, binary readout architecture allows for a power consumption below $40\,\mathrm{mW/cm}^2$.

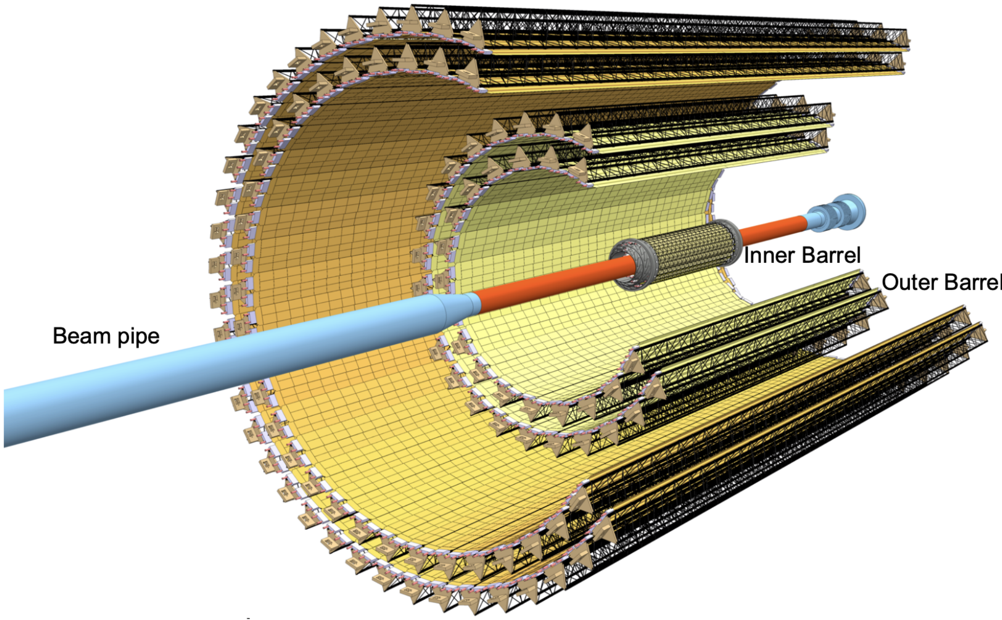

Figure 3: Layout of the ITS2. Taken from [10].

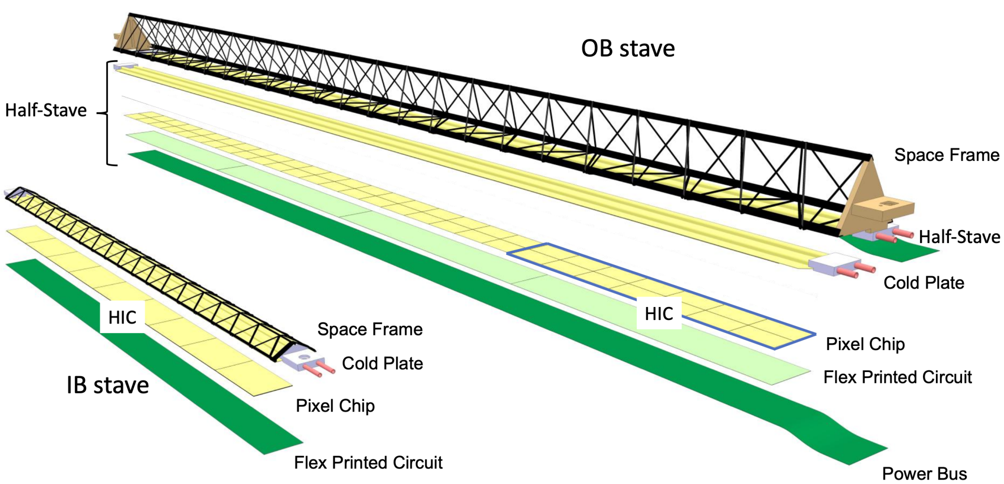

Figure 4: Schematic drawing of the Inner Barrel (left) and Outer Barrel (right) Staves. Taken from [11].

Further, it achieves a spatial resolution of around $5\,\mu$m and a readout rate of 100 MHz for Pb-Pb interactions. Moreover, the technology proved to be radiation hard up to $2.7 \cdot 10^{13}$ $1\mathrm{MeV}\,\mathrm{n}_{eq}\,\mathrm{cm}^{-2}$ NIEL [14] irradiation. More details of the sensor, which is widely used in applications beyond ITS e.g. for beam test campaigns of new hardware prototypes, can be found in [15, 12, 16].

2.4 Upgrade of the Inner Tracking System

During the next Long Shutdown period of the LHC (LS3, 2026 - 2028), the ITS2 will be upgraded to the ITS3 by replacing its three innermost layers, i.e. the IB. The proposed design aims for an even shorter distance to the interaction point while reaching a lower and more homogeneous distributed material budget. In consequence, the pointing resolution as well as the tracking efficiency will be increased. In order to achieve those improvements, an innovative design and thus, an extensive Research and Development (R&D) program is required. This includes stitched, wafer-sized, ultra-thin, and truly cylindrical MAPS obtained by wafer bending. The concept as well as its improvements will be briefly explained in the following Sections.

2.4.1 Reduction of Material Budget

Regarding the composition of the ITS2 IB material budget depicted in Figure 5, it becomes evident that just around 1/7th is due to active silicon pixel layers. Also, the distribution of material is not homogeneous over the azimuth, but is subject to fluctuations caused by the mechanical support, cooling infrastructure, and overlapping of the pixel strips (cf. Section 2.3.1).

To reduce the total material budget and its inhomogeneous distribution, the ITS3 concept features several progressive design approaches. First, the substitution of water by air cooling, which requires an upper limit of the sensor power consumption of approximately $20\,\mathrm{mW/cm^2}$ [17]. In addition, power and data services are planned to be located on-chip allowing for the removal of the integrated circuitry. Furthermore, the material budget of the support structure can be decreased profiting from the increased rigidity of bent with respect to flat silicon. In total, the cumulative reduction should lead to a material budget below $0.05\,\%\,\mathrm{X_0}$ [17].

2.4.2 Concept and Layout

Concerning the strict requirements on the material budget mentioned in Section 2.4.1, the new detector concept relies on cylindrical, bent silicon layers. A sketch of the two half-barrels, which are planned to be placed around the beam pipe, is drawn in Figure 6.

To achieve this structure with the key parameters written in Table 1, the chips forming the silicon layers must be fabricated in wafer-scale size, covering the whole active area of the half barrels. This can only be realized using the 'stitching' method. Usually, the reticle size in the standard CMOS process is limited by the field of view of the used lithographic process and covers an area of a few cm^2. Instead of individual chips of reticle size, separated by thin areas of unused silicon, stitching allows the reticles to be placed with a small overlap interconnecting and merging them into one large active area. In the case of the ITS3, such

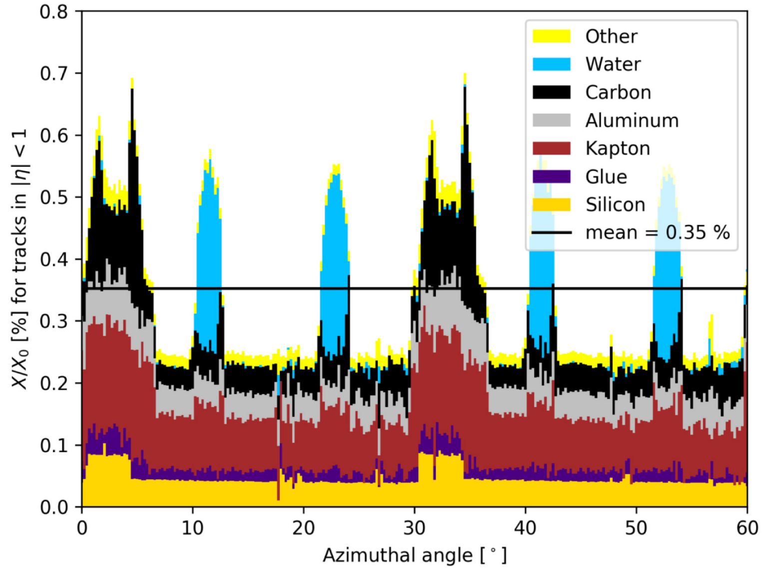

Figure 5: Azimuthal distribution of the material budget of ITS2 layer 0 averaged over $|\eta| < 1$. Taken from [18].

a stitched sensor will cover almost the full wafer.

To allow for the bending radii reported in Table 1, the sensors will be thinned down. A thickness of 50 μm is established to be sufficient for bending to these radii without performance degradation [19]. To reduce the material budget even further, thicknesses below 50 μm are considered.

To profit from larger commercially available wafer sizes with a diameter of 300 mm, the chips for ITS3 are foreseen to be produced in 65 nm TPSCo technology [13]. This allows for a lower power consumption required for moving to air-cooling (cf. Section 2.4.1). The change to a 65 nm process with stitching comes with new challenges regarding the optimization of the yield and charge collection. In addition, the technology needs to be qualified regarding radiation hardness. The requirement put on the ITS3 is 10^{13} 1MeV $\mathrm{n}_{eq}\,\mathrm{cm}^{-2}$ NIEL and 10 kGy TID (see Section 3.1.4).

2.4.3 Simulated Tracking Performance

To compare the tracking performance of ITS2 and ITS3, a simulation of its pointing resolution and its tracking efficiency in dependence on the transverse momentum was carried out using a Fast Monte Carlo Tool [18]. A crucial value of the tracking precision is the track impact parameter. It describes the capability of a vertex detector to separate secondary vertices of heavy-flavour decays from the interaction vertex [18]. A comparison of the impact parameter

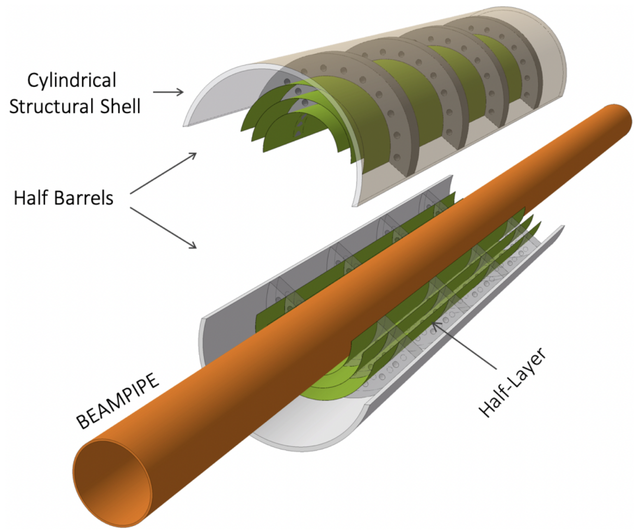

Figure 6: Layout of the ITS3 Inner Barrel. Taken from [18].

Layer parameter	**Layer 0**	**Layer 1**	**Layer 2**
Radial position (mm)	18.0	24.0	30.0
Length (mm)	270 (sensitive area) + 10 (periphery)		
Pixel sensor dimensions (mm^2)	280 × 56.5	280 × 75.5	280 × 94.0
Pixel size (μm ^{2})	$\mathcal{O}(15 \times 15)$		

Table 1: Main layer parameters of ITS3. Values taken from [17].

resolution in the transverse plane is provided by the solid lines in Figure 7a. Here, an improvement of the impact parameter by a factor of around two over most of the momentum range can be seen. For the tracking efficiency depicted in Figure 7b, a greater improvement can be obtained at low transverse momenta of $p_T < 100$ MeV/c.

2.4.4 Impact on Physics

The in Section 2.4.3 described expected tracking performance increase of ITS3, with respect to ITS2, will be especially beneficial for many low transverse momentum measurements of ALICE. Together with the reduced material budget (Section 2.4.1), significant advancements in the main objectives of the ALICE physics program are expected. In particular, the study of heavy flavour production and the study of low-mass dielectrons will profit from the upgrade to ITS3 [18].

To study the thermalization and hadronization of b and c quarks in the QCD medium, the measurements of production and azimuthal anisotropy of charmed and beauty baryons are

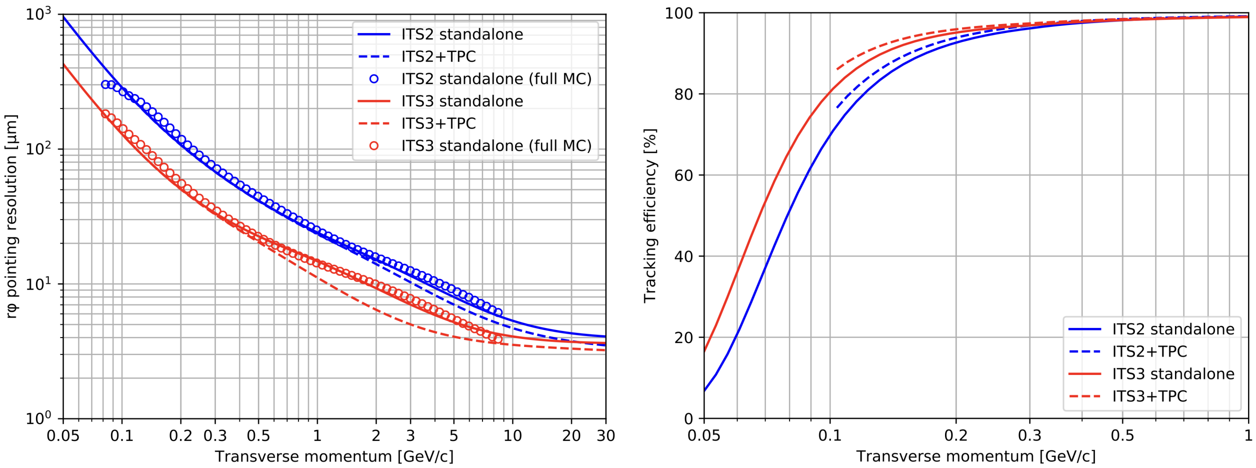

(a) Pointing resolution

(b) Tracking efficiency

Figure 7: Simulated tracking performance comparison between ITS2 and ITS3 in the transverse plane. Taken from [18].

of particular interest [18]. Due to the small lifetime of charmed baryons, as the Λ_c (with $c\tau$ =59 μm [18]), decays are displaced mostly shortly from the main interaction vertex. In addition, the benchmark channel $\Lambda_c^+ \to pK^-\pi^+$, investigated for the ITS2 [10] and ITS3 upgrades, has a large combinatorial background. Thus, its measurement requires precise tracking and impact parameter resolution. A comparison of the expected signal over background ratio between the ITS2 and 3 is shown in Figure 8. The studies are performed at the centre-of-mass energy of $\sqrt{s_{NN}} = 5.5\,\mathrm{TeV}$. From here, an improvement of about a factor of 10 for ITS3 with respect to ITS2 becomes evident. This arises directly from the improved pointing resolution of ITS3 (cf. Figure 7a), allowing for larger combinatorial background suppression and a larger efficiency in the signal selection.

Another example of physics improvements with the ITS3 is the measurement of thermal dileptons (cf. Sections 2.1.3) [18]. Electromagnetic radiation can, besides direct real photon detection, also be observed from virtual photons decaying into a dilepton pair. The production rate of thermal dileptons is suppressed proportional to α^2, where α denotes the fine-structure constant, thus, the systematic uncertainties of the measurements are strongly affected by large combinatorial background. A significant contribution to this is photon conversion, mainly arising from $\pi^0 \to \gamma\gamma$ decays. The improved tracking performance of ITS3 at low p_T (cf. Figure 7b) supports the reconstruction of photon conversions, in which one of the leptons often has a very low momentum. By this, more combinatorial background can be rejected. Reducing the material budget (cf. Section 2.4.1) determines a decrease of electrons from photon conversions. Furthermore, the improved pointing resolution (cf. Figure 7a) allows for efficient tagging of electrons from semi-leptonic charm decays reducing the combinatorial background further. As a result, the upgrade of the ITS2 towards ITS3 can decrease the systematic uncertainty from the subtraction of the combinatorial background by a factor of 2.

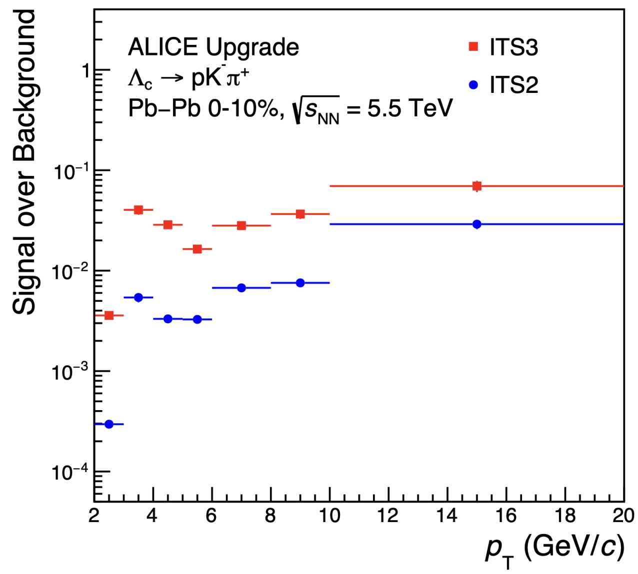

Figure 8: Signal over Background of $\Lambda_c^+ \rightarrow pK^-\pi^+$ in central Pb-Pb collisions as a function of p$_T$. Taken from [18].

The above-mentioned improvements solely represent two examples of the expected physics performance increase coming with the upgrade of the ITS. Further examples and more details can be found in [18].

3 The Digital Pixel Test Structure

To meet the requirements on the pixel sensors in the context of the ALICE ITS3 upgrade (see Section 2.4), an extensive R&D campaign is carried out, studying the pixel test structure implementations fabricated in TPSCo 65 nm [13] imaging process. The first submission in this technology is referred to as the 'Multi Layer Reticle 1' (MLR1) and consists of three different chip types. First, there is the 'Analogue Pixel Test Structure' (APTS), which contains a matrix of 4×4 pixels optimized for a detailed characterisation of the analogue signal output. Second, the 'Circuit Exploratoire 65' (CE65), housing a 64×32 pixel matrix with three different pixel architectures dedicated to the investigation of different sensing node geometries as well as different amplification schemes. Last, there is the 'Digital Pixel Test Structure' (DPTS) which features the most complex design of the submission. It consists of 32×32 pixels and contains a full in-pixel circuitry and a dedicated digital readout scheme. Its functionality and performance are the subject of this thesis. The following sections first provide an overview of the underlying concepts of silicon pixel sensors before discussing general characteristics and the most important measurement software of the DPTS.

3.1 Silicon Pixel Detectors

Silicon pixel detectors are a major category of particle and radiation sensing devices. Typically, they consist of numerous independent detection diodes, which define the pixels. Their large field of application ranges from digital cameras to sensors used for medical imaging. In high-energy physics, silicon pixel detectors can be utilized for tracking charged particles. The following sections provide an overview of the silicon pixel sensor technology.

3.1.1 Semiconductors and Silicon Properties

Depending on the electrical conductivity, a material can either be classified as an insulator, conductor or semiconductor. As shown in Figure 9, the distinction depends on the energy band structure of the material, resulting from the allowed states of the quantum mechanical wave function of the electrons in the solid-state lattice. Here, the material is characterized by the energy gap E_G between the two highest energy bands: the valence band at the energy E_V and conduction band at an energy E_C. In contrast to electrons in the valence band, electrons in the conduction band are able to move almost freely in the material. For insulators, E_G is usually in the order of 10 eV and therefore too large to be overcome by thermal excitation. On the contrary, the valence and the conduction band of conductors are overlapping leading to a constant contribution of available electrons to charge transportation. Semiconductors however show unique conduction properties in between conductors and insulators. In the case of silicon, the energy gap is $E_G = 1.12\,\mathrm{eV}$ [20], such that thermal excitation can lift electrons from the valence band to a quasi-free state in the conduction band.

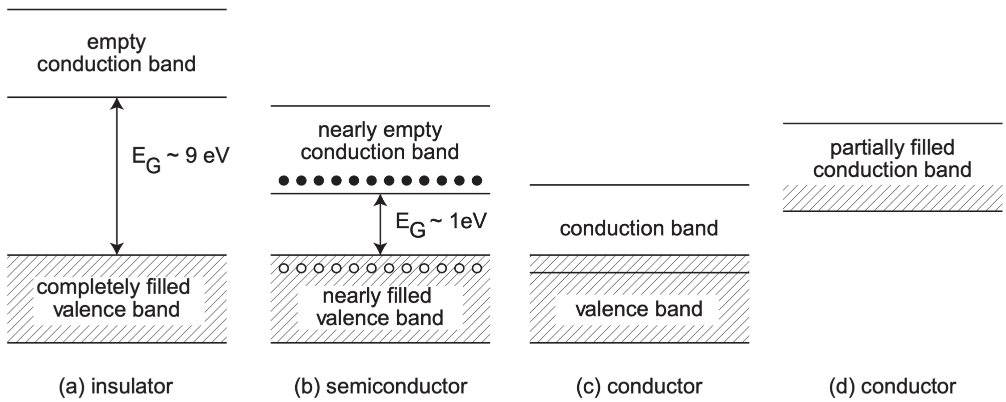

Figure 9: Sketch of the band structure of different material classifications. Taken from [20].

The charge carrier concentration n(E) of the semiconductor at equilibrium is given through the density of states Z(E) multiplied by the respective occupation probability f(E):

$$n(E)\,dE = Z(E)\,f(E)\,dE \tag{4}$$

In thermal equilibrium, the density of possible states for charge carriers is proportional to $\sqrt{E}$. A derivation of this can be found in [20]. For the Spin-1/2 electrons, the occupation probability f(E) of the states follows the Fermi-Dirac distribution:

$$f(E) = \frac{1}{exp(\frac{E-E_f}{kT}) + 1} \tag{5}$$

Here, k denotes the Boltzmann constant and T is the system's temperature. The Fermi-level E_F is defined as the energy corresponding to a 50 % occupation probability. At $T = 0\,\mathrm{K}$, all charge carriers have an energy below E_F. Note that for positive charge carriers, e.g. holes, the sign of the exponent in Equation 5 changes. A visualization of the energy bands, the density of states, the occupation probability and the population density of an intrinsic, i.e. chemically pure, semiconductor is shown in Figure 10.

The conduction properties of intrinsic semiconductors can be manipulated by doping. In the case of silicon, this process consists of inserting trivalent atoms, called acceptors, or pentavalent atoms, called donors, into the tetravalent silicon lattice. This results in n-doped or p-doped extrinsic semiconductors, respectively. In the case of n-doped semiconductors, the fifth valence electron possesses an energy band at E_D, in the order of 10^{-2} eV [20] below the lower end of the conduction band. Therefore, almost all donors are ionized at room temperature. This directly results in an increased fermi-energy E_F as illustrated in Figure 11. Following Equation 4, an excess of negative charge carriers results from the n-doping. In the case of p-doping, an additional energy level of the acceptors E_A close to the upper edge

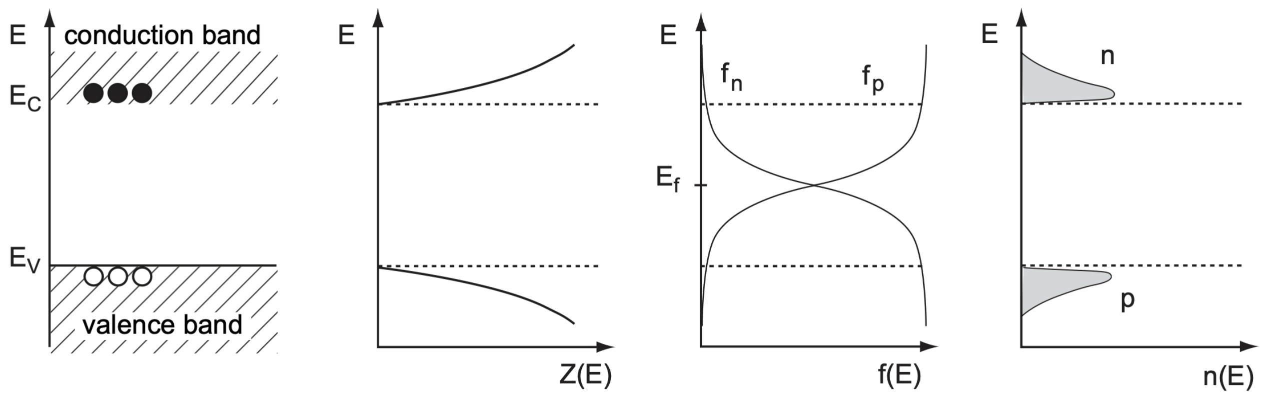

Figure 10: Band model for an intrinsic semiconductor. Taken from [20].

of the valence band is introduced. In contrast to the case of n-doping, E_F is decreased in this case leading to an excess of positive charge carriers. Doping allows to precisely control the conductivity of the semiconductor and thus allows for many technical applications.

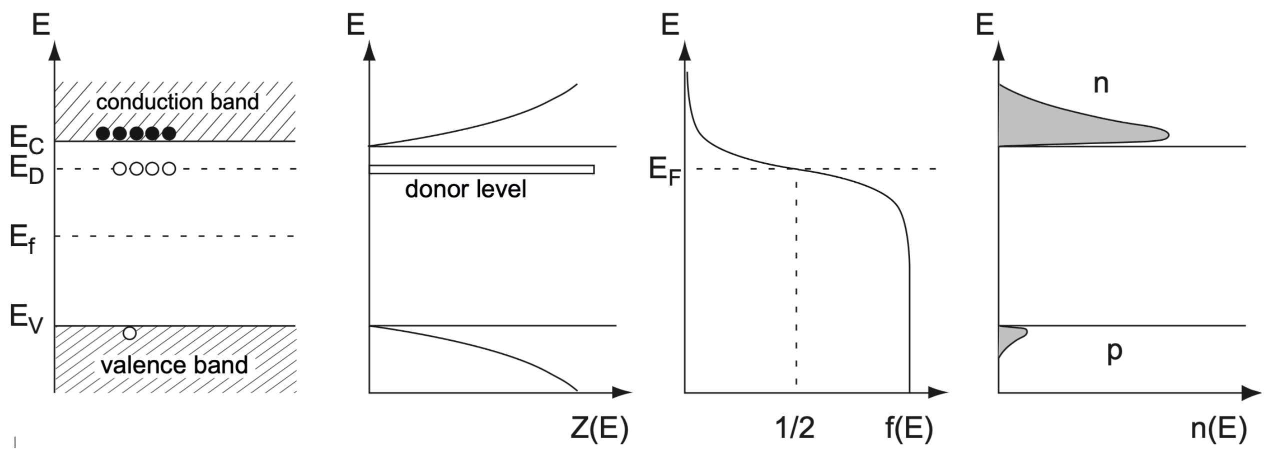

Figure 11: Band model for a n-type semiconductor. Taken from [20].

3.1.2 PN-junction

A pn-junction consists of an n-doped semiconductor in direct contact with a p-doped one as shown in Figure 12. Here, a high gradient in the doping concentration between the acceptor concentration N_A and the donor concentration N_D is established. By this, diffusion currents j_{diff} for both positive and negative charge carriers are created leading to negative electrons diffusing into the p-doped region and positive holes to the n-doped region. The diffused electrons recombine in the p-doped region, while the vacancies recombine in the n-doped bulk. This leads to a space-charge region around the pn-junction as depicted in Figure

12. As a result, an electric field E is created leading to a drift current j_{drift} counteracting j_{diff} for both types of charge carriers. With this, the diffusion is terminated establishing an equilibrium in the system. The built-in voltage V_{bi}, which is the voltage created by the space-charge region at this equilibrium, can be described by:

$$V_{bi} = \frac{kT}{e} ln\left(\frac{N_A N_D}{N_i^2}\right) \tag{6}$$

Here, e is the electron charge and N_i symbolizes the intrinsic charge carrier concentration of the semiconductor. The Poisson equation for a pn-junction with an electric potential $\Phi(x)$ and a charge density distribution $\rho(x)$ is given by:

$$\frac{d^2\Phi}{dx^2} = \frac{-\rho(x)}{\epsilon_0\epsilon} \tag{7}$$

Here, ϵ_0 and ϵ represent the vacuum and relative permittivity, respectively. From the Poisson equation, the width w of the depletion zone in equilibrium can be derived to Equation 8 for the case $N_A >> N_D$. A detailed derivation can be found in [20].

$$w \approx \sqrt{\frac{2\epsilon\epsilon_0}{e}\frac{1}{N_D}V_{bias}} \tag{8}$$

The equilibrium of the pn-junction can be modified by applying an external voltage V_{ext} between the p-doped and the n-doped region. Since the resulting external field superimposes with the field of the built-in voltage, Equation 8 has to be modified as following:

$$w \approx \sqrt{\frac{2\epsilon\epsilon_0}{e}\frac{1}{N_D}(V_{bias} - V_{ext})} \tag{9}$$

From Equation 9 the general behaviour of the junction under external voltage becomes directly evident: If the external voltage is positive, the width of the depletion zone decreases. If $V_{ext} \geq V_{bias}$, the depletion region vanishes. In this case, no insulating layer is present in the junction any more and the junction becomes conductive. This is called forward-biasing. In the situation of $V_{ext} < 0$, the width of the depletion region increases leading to a larger insulating region. This is also called back-biasing. The pn-junction is the base of the semiconductor diode and one of the standard components of general electronics. Therefore, it is also simply referred to as a diode.

3.1.3 Monolithic Active Pixel Sensors

Monolithic Active Pixel Sensors (MAPS), represent a state-of-the-art type of silicon pixel detectors. The technology is based on Active Pixel Sensors (APS), where the readout electronics of the pixels are placed directly next to an active cell inside the active layer. Due to

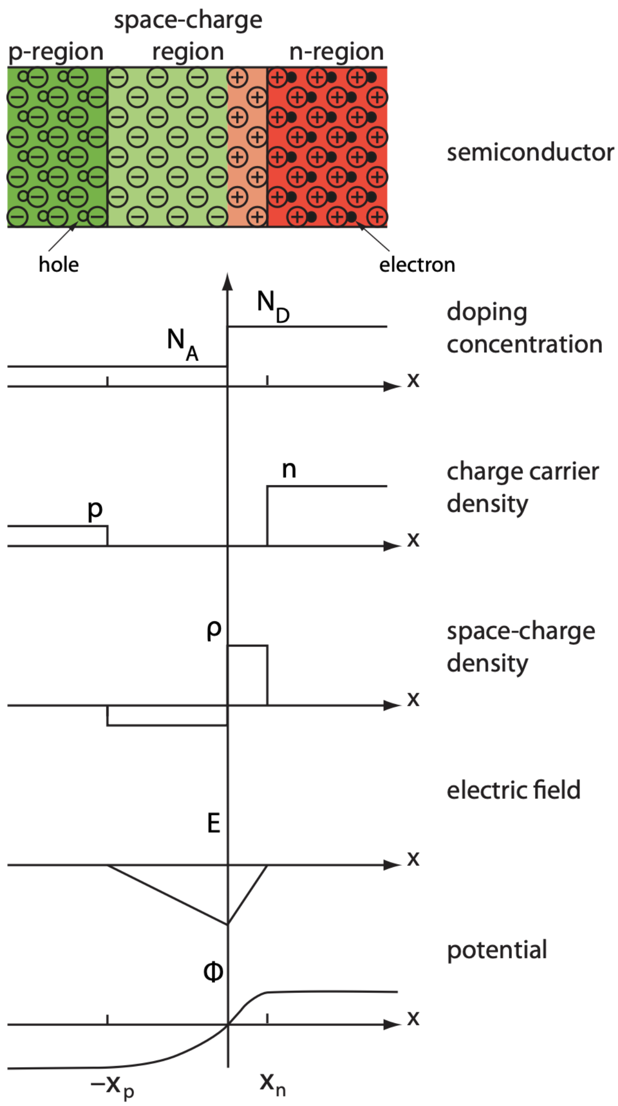

Figure 12: Sketch of a static pn-junction together with the spatial distribution of the doping concentration, the charge carrier and space-charge density, the electric field and its potential. Taken from [20].

the inactive readout cells, the sensor is not active over its whole area. This drawback can be improved by the MAPS design, where the readout electronics is placed on top of the active layer, in the same substrate, as illustrated in Figure 13. This way, a fully active sensor area can be created. A MAPS consists in general of three layers. At the bottom is a low-ohmic p-substrate acting as the mechanical carrier of the sensor. On top of it, a low p-doped, high resistive epitaxial layer is placed as the active volume of the sensor. Together with a n-well on the top layer, a pn-juction is formed creating a depletion region extending into the epitaxial layer. As described in Section 3.1.2, the width of the depletion region can be controlled by applying a back-bias voltage between n-well and the epitaxial layer. A collection electrode on top of the n-well connects to the readout electronics. Here, the NMOS-transistors are placed inside p-wells in the top-layer. The PMOS-transistors are additionally shielded from the epitaxial layers by deep p-wells, avoiding the creation of an additional depletion zone.

When a charged particle traverses the material of the sensor, it loses energy mostly due to ionization creating electron-hole pairs. Generally, the generated charge carriers diffuse across the epitaxial layer until they reach a depletion region, where they drift towards the collection diode, inducing a mirror charge. After being registered, the signal can be further processed as explained in Section 3.2.2.

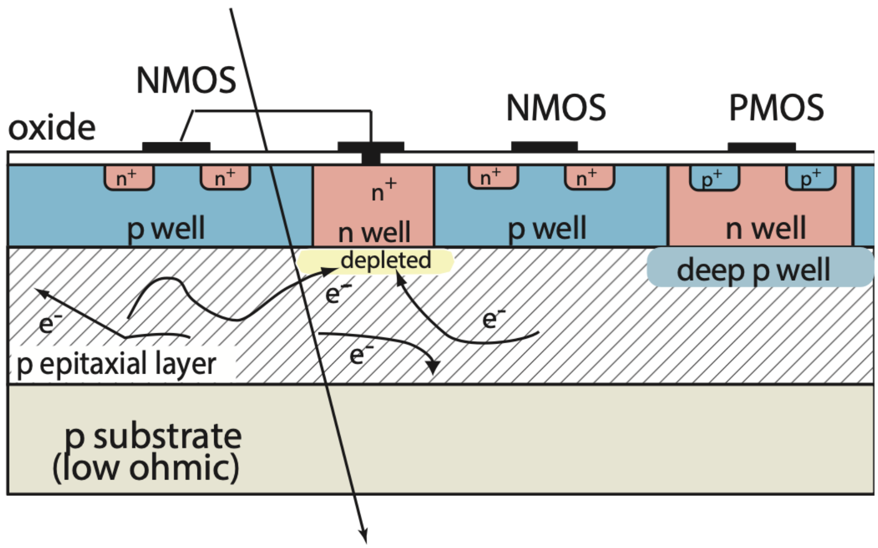

Figure 13: Sketch of the cross section of a conceptual MAPS. Taken from [20].

3.1.4 Radiation Damage

Silicon sensors, like any other radiation detector in a particle physics experiment, are by definition exposed to a level of radiation depending on the distance of the sensor to the interaction point and the material between interaction point and sensor. The radiation consists in general of charged and neutral particles, as well as of γ and X-rays, which can generate radiation damages in the sensor impacting its performance or even destroying it. A measure for radiation damage caused by ionisation is the Total Ionising Dose (TID), whereas damages caused by non-ionising radiation are expressed by the Non Ionising Energy Loss (NIEL).

In silicon sensors, TID essentially creates surface damage impacting the operation of CMOS circuitry elements, whereas NIEL produces damage in the crystal lattice of the bulk silicon.

In Figure 14, different types of lattice damages, i.e. defects, are illustrated. The smallest types are point defects. Those can be simply a vacancy or an interstitial in the crystal lattice. Also, single impurity atoms count to this type of defect. Some examples of more complex defects are depicted within the dashed lines in Figure 14. In semiconductor physics, the damage caused by NIEL radiation is typically expressed normalized to the damage level caused by 1 MeV neutrons. Therefore, the total radiation fluence is conventionally given in neutron equivalent flux, i.e. $1\mathrm{MeV}\,\mathrm{n}_{eq}\,\mathrm{cm}^{-2}$. The expected NIEL level for ITS3 (see Section 2.4), is 10^{13} $1\mathrm{MeV}\,\mathrm{n}_{eq}\,\mathrm{cm}^{-2}$ [18].

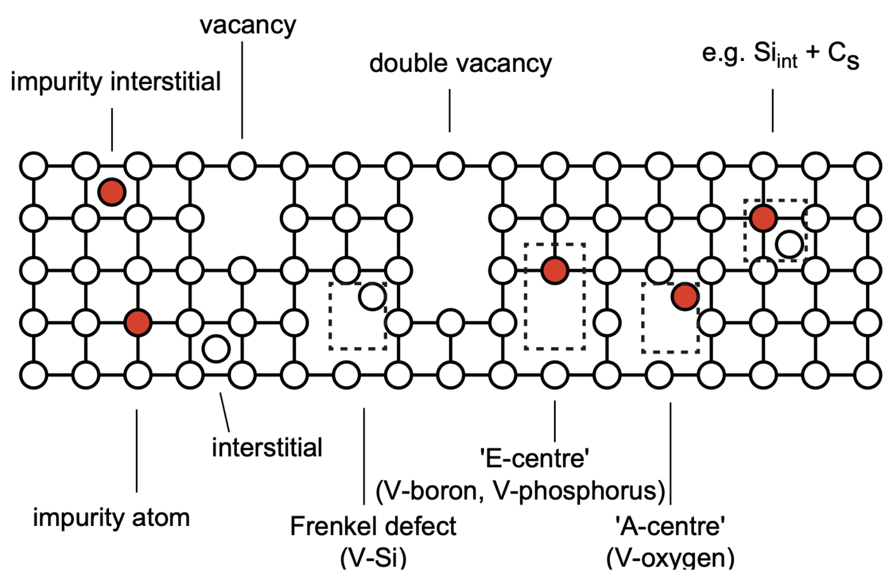

Figure 14: Sketch of different defect types in the silicon lattice. Taken from [20].

In terms of sensor operation, radiation damage can have different types of impact. Surface and boundary damage mostly affect the CMOS transistors and therefore the readout electronics of the detector by causing shifts of voltage levels and operating currents.

The impact of substrate volume damage is illustrated in Figure 15. The defects can cause additional energy levels between the valence and conduction band. Depending on their position, they can cause different unfavourable sensor effects. Charged defects lead to a distortion in the sensor's field and can result in a larger charge collection time or even charge trapping. Energy levels close to the Fermi energy may create recombination centres which increase the leakage current of the sensor. Close to the limits of the conduction or valence band, additional energy levels can act as trapping centres.

Since during the operation time of ITS3, both surface and substrate volume damage is expected, the study of radiation hardness is crucial for a successful detector operation. In this thesis, the impact of NIEL radiation on the DPTS sensor performance in terms of energy spectra will be investigated.

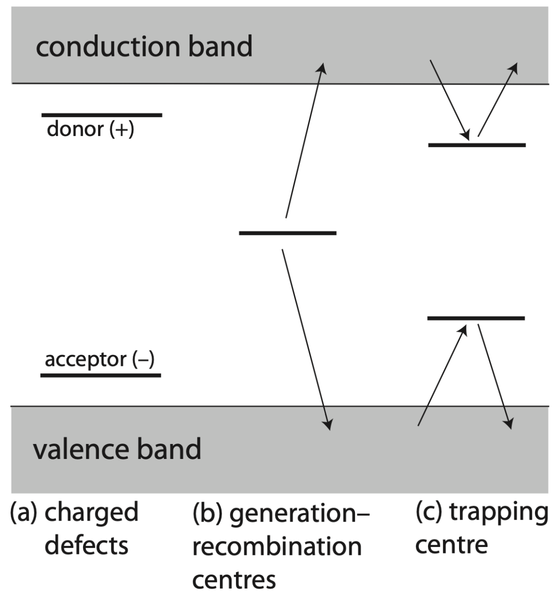

Figure 15: Sketch of typical additional energy level locations due to lattice defects. Taken from [20].

3.2 General Characteristics of the DPTS

The DPTS sensor measures in total $1.5 \times 1.5\,\text{mm}^2$ and its matrix consists of 32×32 pixels with $15 \times 15\,\mu\text{m}^2$ pixel pitch. Figure 16 shows the functional diagram with the major building blocks of the sensor.

The signal, which is either collected in the diode of a pixel or artificially created by the charging and sudden discharging of the injection capacitance C_{inj}, is amplified in the first stage. In addition to the 1024 pixels of the sensor matrix, the DPTS features one monitoring pixel for probing the analogue response after the amplification stage. For all other pixels of the matrix, the amplified signal is discriminated against a voltage level i.e. the sensor's threshold (cf. Section 3.2.2). With the exception of masked pixels specified by the shift register, the address generator of the firing pixel time-encodes the hit position and Time-over-Threshold (ToT). The encoding scheme will be described in more detail in Section 3.2.3. In the sensor periphery, the hit merger will unify the addresses of all 1024 pixels to one single output line. Finally, the Current Mode Logic (CML) sends an output signal in a positive and negative polarity. From here, the signal can be read out using the setup described in Section 3.2.4.

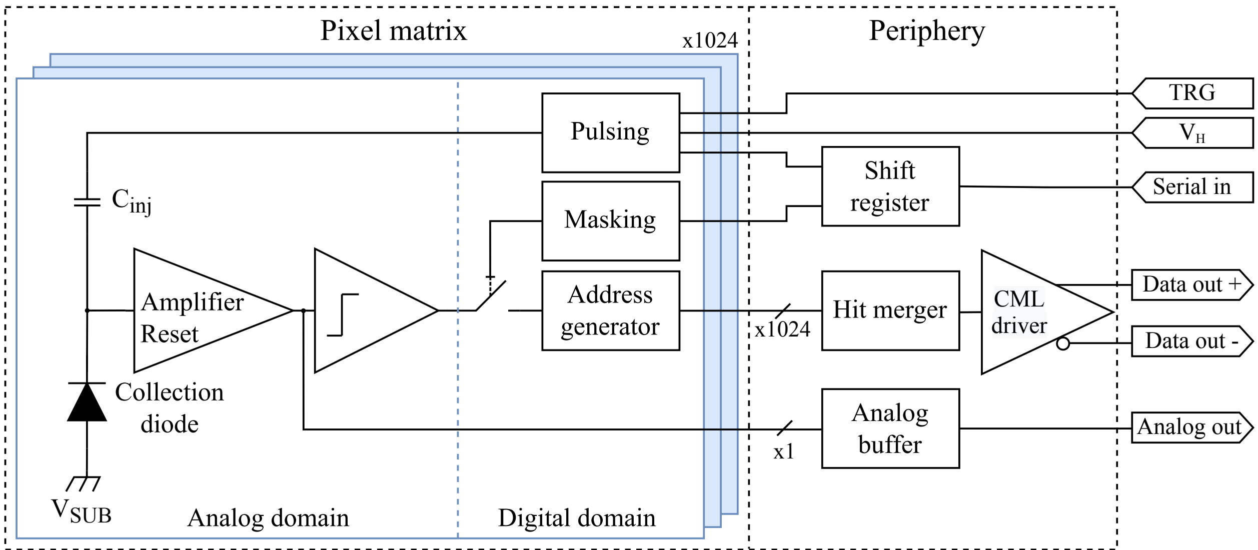

Figure 16: Functional diagram of DPTS. Taken from [21].

3.2.1 Fabrication Process

As already mentioned, DPTS is fabricated in the TPSCo 65 nm imaging process. To be able to investigate different implant geometries, the MLR1 submission includes the three different fabrication flavours which are sketched in Figure 17: the 'standard process', the 'modified process' and the 'modified process with gap'.

The standard version is based on a doping profile commonly used in MAPS including the ALPIDE 2.3.2. Here, a p^--doped epitaxial layer is placed as an active volume on top of the p^+-doped substrate, which acts as a mechanical support for the sensor. Furthermore, deep p-wells are brought into the epitaxial layers shielding the CMOS in-pixel circuitry from the active volume. Between the p-wells, a n-well collection electrode is placed. A back-bias voltage (VBB) is applied to this diode, leading to a depletion region expanding almost radially into the epitaxial layer. Even using the maximum design value for VBB, it is not foreseen that the depletion zone will completely cover the epitaxial volume.

The modified process is based on the standard one with the exception of an additional low-dose n-implant introduced in order to displace the pn-junction away from the collection electrode. This leads to a depletion zone propagating further into the epitaxial layer, which is capable of covering its entire volume. With this, it is expected to increase the sensitive volume while decreasing the charge collection time since all charges created in the epitaxial layer are collected via drift.

The modified process with gap additionally introduces a separation of the low-dose n-implant with a spacing of 2.5 μm. Its design increases the lateral field component and thus the acceleration of the signal charge towards the collecting electrode. Consequently, a reduced charge sharing is expected, resulting in a wider operating margin due to a larger seedpixel signal [21].

DPTS was produced in four different splits, gradually modifying the doping of different implants. This thesis only addresses the modified process with gap and the split with the best expected performance regarding the detection of ionizing particles (Split 4).

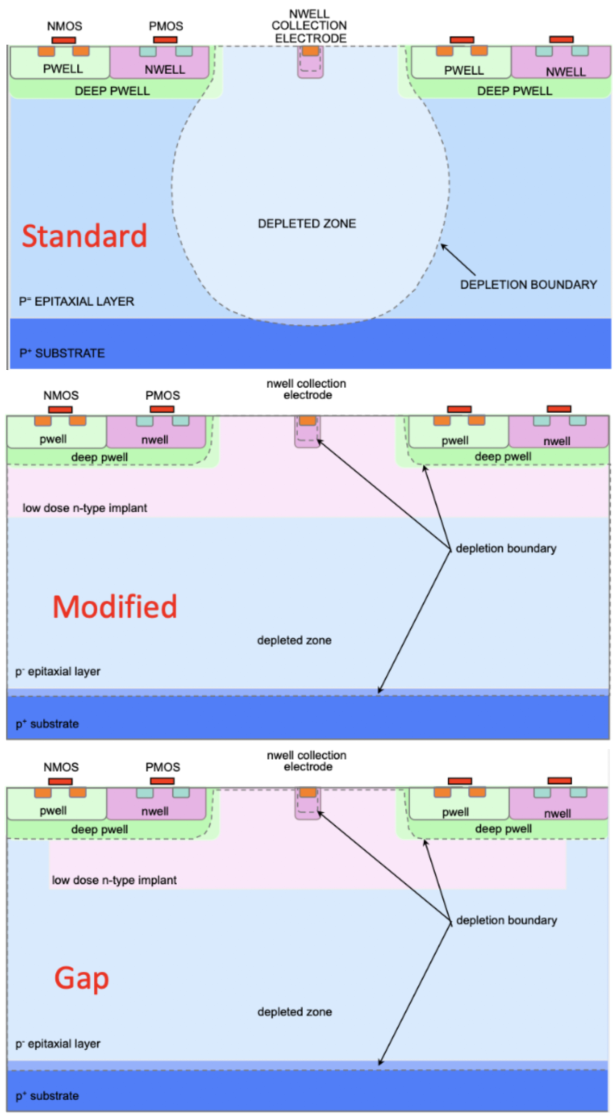

Figure 17: Pixel cross-section of the three DPTS versions. Not to scale. Modified from [8].

3.2.2 In-pixel Frontend

The analogue in-pixel frontend of DPTS, which is shown in Figure 18, is mainly controlled via four currents (I_{bias}, I_{reset}, I_{db} and I_{biasn}) as well as the two voltages V_{casb} and V_{casn}. All of them are externally generated and supplied via the MLR1 DAQ-Board and the Proximity Board (see Section 3.2.4). In addition to the controlling voltages, there is the pulsing voltage VH for creating test pulses through a discharge of the injection capacitance C_{inj} and the circuit supply voltage AVDD. Further, the substrate voltage SUB is externally supplied. Figure 18 shows that the initial signal is processed in two stages. In the first stage, it is amplified. Here, the return to baseline of the signal can be controlled directly by the I_{reset} current. In the second stage, the signal will be discriminated against the threshold for further processing in the periphery.

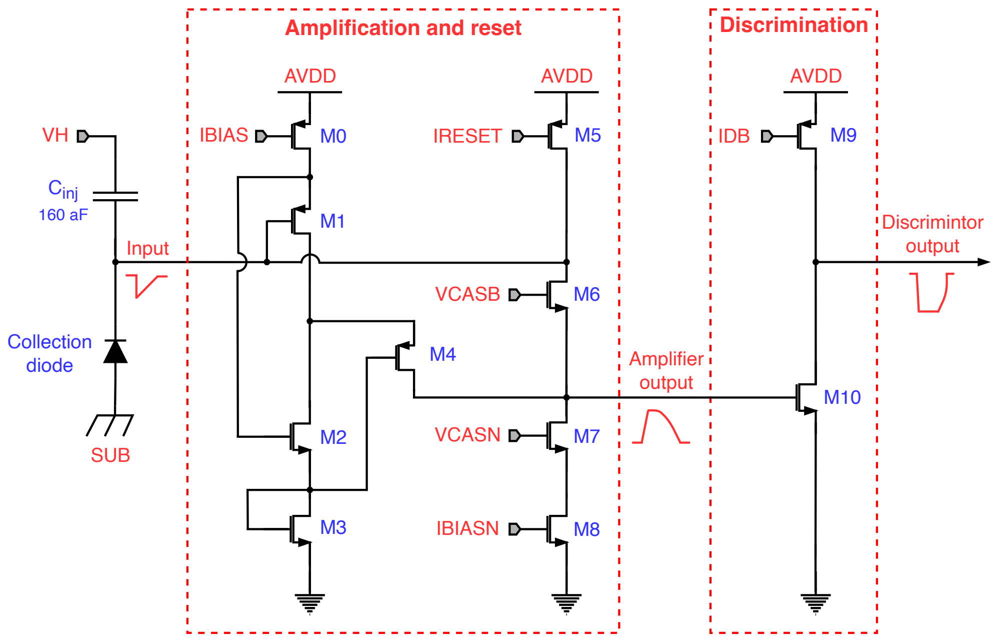

Figure 18: Schematic of the in-pixel amplification and discrimination circuit. Taken from [21].

3.2.3 Hit Position and Time over Threshold Encoding

The edges of the discriminated output signal of the pixel frontend described in Section 3.2.2 will trigger the address generator to send out two pulse trains on the CML output: one at the rising edge and one at the falling edge of the signal. In this work, they will be referred to as rising edge train and falling edge train, respectively. Each pulse train carries the time-encoded position information of the hit.

As sketched in Figure 19, each pulse train consists of two consecutive pulses. The first one acts as a reference pulse with a well-defined length. The second pulse has a variable length depending on the hit position. The time distance between the rising edge of the normed pulse and the rising edge of the second pulse encodes the hit position within a group of columns, i.e. the Pixel Identification (PID). The duration of the second pulse within a train encodes the position of the column group, i.e. the Group Identification (GID). The ToT information is encoded in the time difference between the two rising edges of the first and the second pulse train. The sensor's frontend is designed such that the pulse length is monotonically increasing with the input signal. Thereby, the ToT provides information on the collected or injected charge [21].

Since the addresses of all pixels are multiplexed and driven to the same output line, simultaneous firing pixels can lead to signal collisions. This results in a non-decodable output. To mitigate this effect in the case of charge sharing between neighbouring pixels, the output signal of pixels in one column is delayed by a fixed time with respect to the neighbouring columns. Additionally, a checkered arrangement of the GID in the readout allows to mitigate further the influence of pulse train collisions. More details can be found in [21, 8].

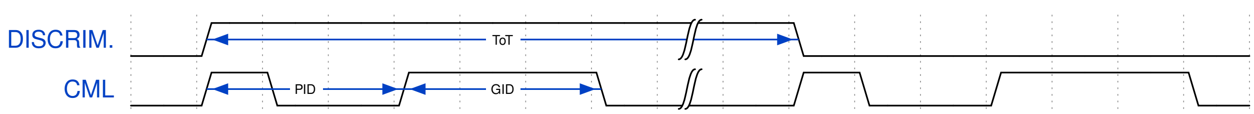

Figure 19: Hit position and ToT encoding scheme of DPTS. Taken from [21].

3.2.4 Data Acquisition Setup

The data acquisition setup for the DPTS is depicted in Figure 20. It consists of three main parts: the carrier card, the proximity board and the Data Acquisition board (DAQ-Board).

The sensor is bonded to the Carrier card using aluminium wires. On its backside, a 10 mm thick aluminium cooling jig connected to a water chiller can be placed for chip temperature control. The carrier card also hosts two SMA connectors for both polarities of the CML output (see Section 3.2). The CML output is then read out via an oscilloscope of the PicoScope® 6000E series [22] with a sampling rate of 5 GS/s and a bandwidth of 500 MHz [21]. In the beam test as well as in the laboratory setup, it reads the waveforms and saves them to a data-taking computer connected to it. Each waveform consists of a variable number of frames (nominal: 200.000) with a length of 0.2 ns. In this work, the term 'event' refers to one single acquired waveform.

The operational parameters of the DPTS, such as registers, voltages and supply currents, are set by sending corresponding commands to a Field Programmable Gate Array (FPGA) on the MLR1 DAQ board. It can be programmed via a Universal Serial Bus (USB) connection. The board is designed for universal usage for all sensors of the MLR1 submission as well as for the use with ALPIDE detectors. In order to adapt to the specific MLR1 chip type (e.g. the DPTS or the APTS), a Proximity board is used to connect the DAQ-Board with the corresponding Carrier card.

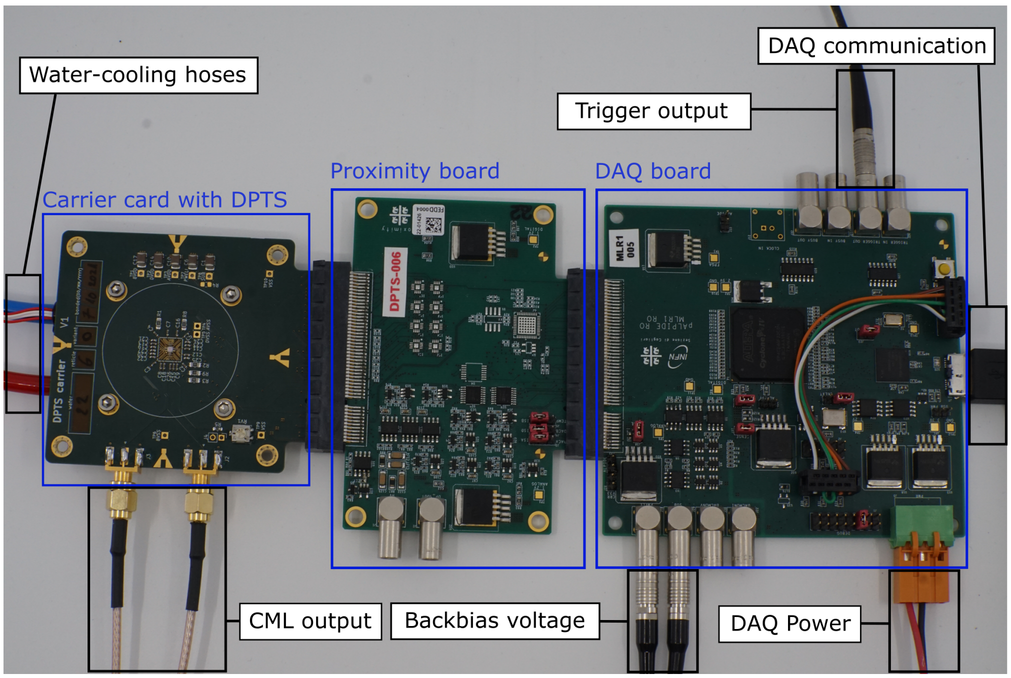

Figure 20: Picture of the single-DPTS setup.

3.3 Measurement and Analysis Software

For the processing of DPTS data, several dedicated analysis tools were developed. The basic scripts used for this work are described in the following Sections.

3.3.1 Hit Position Decoding

As described in Section 3.2.3, the hit position information of a firing pixel is encoded into PID and GID values. The exact conversion factor is observed to be dependent on the specific chip, arising from uncertainties in the sensor fabrication. Also, it depends on the operation conditions of the sensor i.e. the set frontend parameters and the device's temperature. Therefore, a decoding calibration is required to convert a recorded (PID, GID) pair back to its corresponding pixel position. To mitigate the influence of the operation conditions, the calibrations used in this thesis are always taken in situ, right before or after the corresponding measurement.

A decoding calibration is obtained by pulsing every pixel one by one 100 times, recording their PID/GID values. This will result in 1024 clusters of 100 points each in PID/GID space as depicted in Figure 21a. For each cluster, the centre of gravity (CoG) will be determined and used as a calibration point. The resulting set of 1024 CoG points will be referred to as a calibration map in this work. A calibration map can be obtained using (PID, GID) pairs either of the rising edge or of the falling edge trains (see Section 3.2.3). As exemplarily depicted in Figure 21b, it was observed that rising edge clusters do not necessarily overlap with the falling edge ones. Therefore, it is required to obtain different calibration maps to decode rising edge or falling edge trains, respectively.

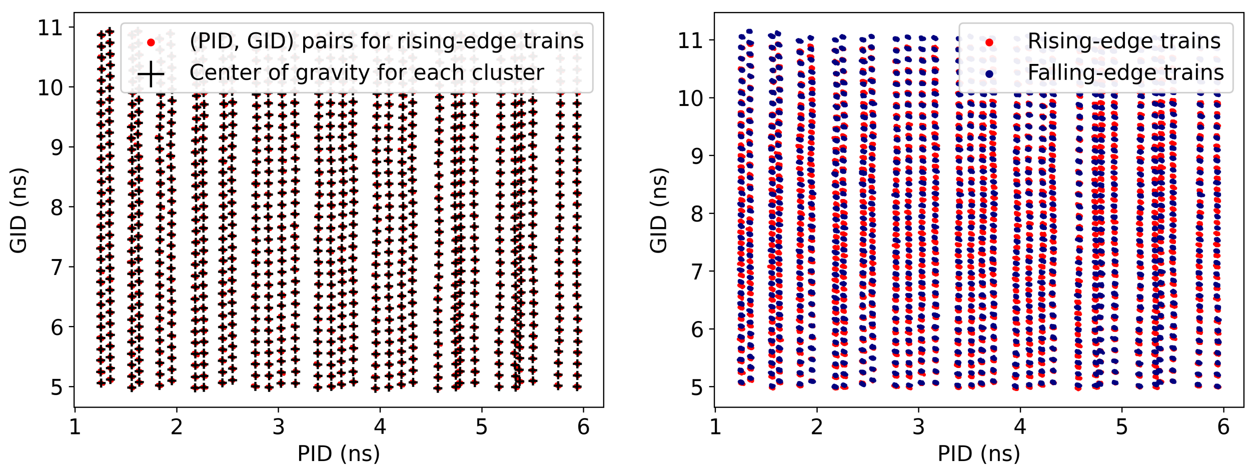

(a) Rising edge decoding calibration with associated Center-of-Gravity points for each cluster.

(b) Comparison of the rising edge and falling edge decoding calibration.

Figure 21: Exemplary decoding calibrations.

The influence of different operation conditions on the decoding calibration, such as for temperature and back-bias voltage (VBB), is demonstrated in Figure 22. For the provided example, the mean (PID, GID) position shifts around 8 ps/K while VBB leads to a larger shift of 0.55 ns/V.

To decode the hit position of a recorded train, the corresponding (PID, GID) tuple will be associated with the nearest calibration point. During this association process, decoding errors, i.e. associations to a wrong calibration point, can occur. This can happen e.g. due to very close calibration points in the (PID, GID) space. This way, a train will be associated with a wrong pixel position.

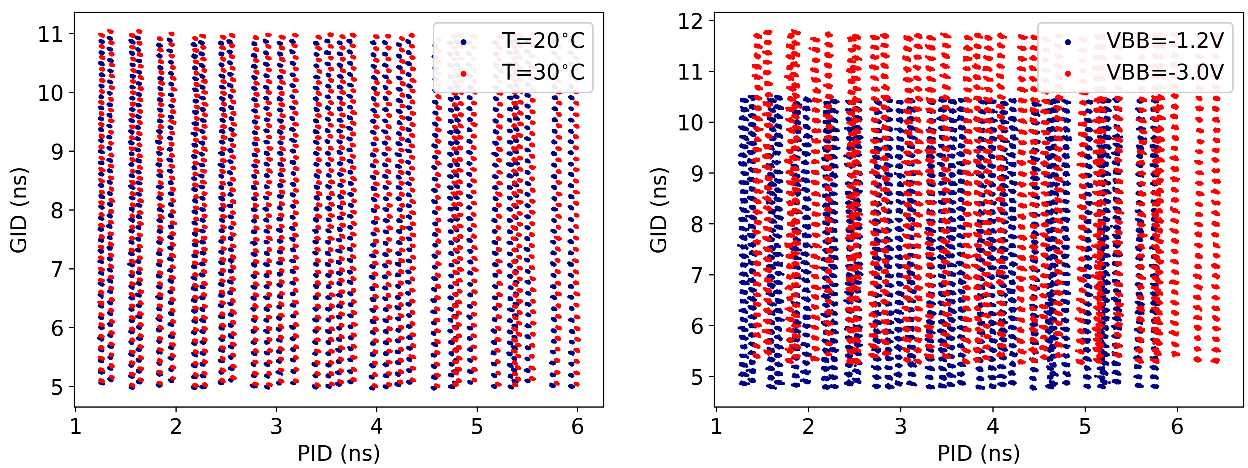

(a) Temperature dependence

(b) Backbias voltage comparison

Figure 22: Dependence of the decoding calibration on different operation conditions for rising edge trains.

3.3.2 Threshold Scan

The detection probability of an input signal depending on the input charge Q_{inj} follows a characteristic shape. In an ideal case without noise, no signal with a charge less than the threshold will be detected. Signals with a higher charge deposit are always detected. Therefore, the detection probability p in dependence on the injected charge follows a Heaviside function centred around the comparator threshold. A real signal however always contains a noise component which can be described by a Gaussian distribution. The convolution of the Heaviside function and a Gaussian with standard deviation σ centred around a mean μ leads then to an s-curve defined as:

$$p(Q_{inj}) = \frac{1}{2}\Big(1 - erf\Big(\frac{Q_{inj} - \mu}{\sqrt{2}\sigma}\Big)\Big) \tag{10}$$

In order to estimate the threshold of a pixel, a threshold scan can be performed. For this, the possibility to inject artificial test pulses into the pixel described in Section 3.2.2 is utilized. Within a threshold scan, the pulsing voltage VH is varied in a defined range around the expected pixel threshold in discrete steps. For every VH, the pixel is pulsed 25 times and the number of registered hits is recorded. The resulting dependency between VH and the registered number of hits follows a s-curve shape. Since the derivative of an s-curve is a Gaussian with the same μ and σ parameters, the s-curve's discrete derivative can be used in order to extract the respective values. While σ is directly proportional to the pixel‘s noise, and therefore can be used for its quantification, μ represents the threshold of the pixel. By obtaining the s-curves of all pixels on the sensor matrix, its threshold distribution can be determined. Its mean and RMS are used to estimate the sensor's threshold and threshold spread. Figure 23 shows an exemplary threshold extraction for the full matrix of the DPTS. In this work, the DACs VCASB and VCASN described in Section 3.2.2 are used to control the DPTS threshold.

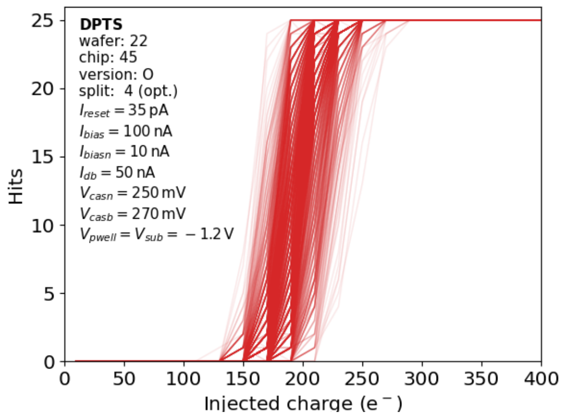

(a) Recorded s-curves. Each curve corresponds to one pixel.

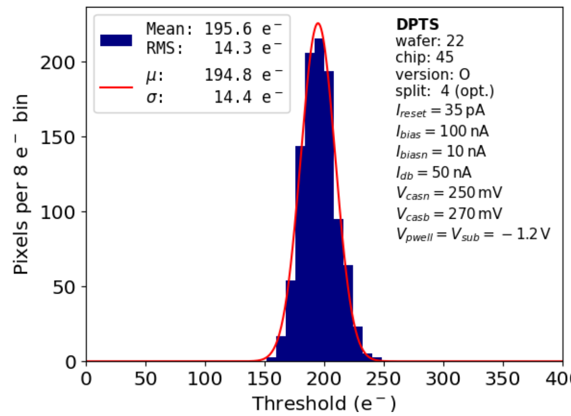

(b) Fitted threshold distribution. The thresholds are extracted from the mean of the s-curves depicted left.

Figure 23: Exemplary threshold extraction of the full DPTS matrix via charge injection.

3.3.3 Fake-hit Rate Scan

Another tool used in this work to ensure a stable operation of the DPTS at a certain operational point is the fake-hit rate scan. Here, a fake-hit is defined as a hit signal occurring on the CML output (see Section 3.2) even if no particle has traversed the sensor. The fake-hit rate (FHR) can be determined by an artificial device triggering with no external signal source. For the measurements conducted in the context of this work, a number of $n_{trig} = 100.000$ triggers is used with a readout time of $\Delta t = 40\mu s$ after the trigger. The FHR can then be calculated by:

$$FHR = \frac{n_{hits}}{n_{pix} \cdot n_{trig} \cdot \Delta t} \tag{11}$$

Here, n_{pix} represents the number of pixels on the sensor (1024 for the case of DPTS), and n_{hits} is the number of registered fake-hits. The sensitivity limit of the FHR scan can be obtained by setting $n_{hits} = 1$ in Equation 11.

3.3.4 ToT-calibration

The integrated pulse height of the amplifier output is proportional to the charge collected by the firing pixel. Since the ToT scales with the pulse height, it can be used as a measure of collected charge on the DPTS. Arising from fabrication uncertainties, the ToT response to a certain input charge varies from pixel to pixel. This effect is referred to as inter-pixel ToT variation. Figure 24 shows the recording of ToT values of DPTS at different values of pulsing voltage VH. As VH is the voltage used to charge the injection capacitance described in Section 3.2.2, it is directly related to the injected charge Q_{inj}. The measured ToTs of the full matrix at varying VH values are depicted in blue, while the recording of two specific pixels with a distinct ToT(VH) dependence are shown in red and green, respectively. The pixel dependencies show a non-linear behaviour for VH around the pixel threshold, which becomes linear for larger VH. Here, the inter-pixel ToT spread increases. To account for this, the $ToT(VH)$ dependency can be fitted using the empirical function [21]:

$$ToT = a \cdot VH + b - \frac{c}{VH - d} \tag{12}$$

Here a,b,c and d are the fit parameters. Performing the fit for all pixels provides a parameter set that can be used in order to convert the measured ToTs into the corresponding pulsing voltage. This way, the effect of inter-pixel variations can be compensated for. The Sections 4.4.1 and 5.3.3 are showing the effect of the ToT calibration on recorded $^{55}_{26}$Fe spectra and energy-straggling distributions, respectively.

3.4 Train Association and Clustering

A cluster is a group of adjacent pixels on the sensor matrix firing in the same event. This occurs whenever the charge released in the active region of a sensor is collected by neighbouring pixels. Here, the cluster-size (CS) is given by the number of pixels contributing to the cluster. The process of grouping pixels into a cluster is commonly referred to as clustering.

In DPTS's asynchronous readout, the pulse trains of all pixels in an event are multiplexed to one single readout line (see Section 3.2.3). Therefore, clustering requires the association of the rising edge train with the corresponding falling edge train for all pixels in the cluster. Only for associated train-pairs, the ToT can be extracted.

In the case of a single-pixel cluster event, just two pulse trains are expected on the readout line as sketched in Figure 25. Here, the association of trains is trivial and the ToT can be directly extracted. However, in the case of a two-pixel cluster, already four pulse trains are recorded on the readout line. A priori, it is not known which trains should be associated. Therefore, the trains need to be decoded into pixel positions following the procedure described in Section 3.3.1. Since it is also unknown which trains arise from the rising edge of a pulse and which ones arise from a falling edge, an assumption needs to be made for the decoding.

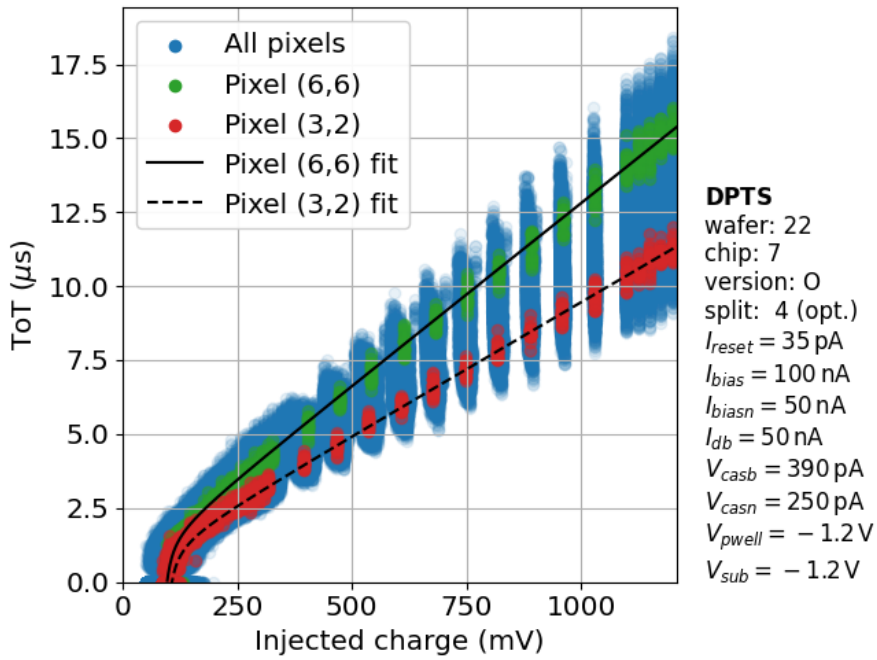

Figure 24: ToT dependence of a DPTS on the injected charge. Plotted with data published in [21].

It is assumed that the first half of the trains are rising edge trains and the second half are falling edge trains. This assumption is justified by the fact that the delay, introduced between pulse trains by the address-generator (see Section 3.2.2), is much smaller than the mean ToT of the device [21].

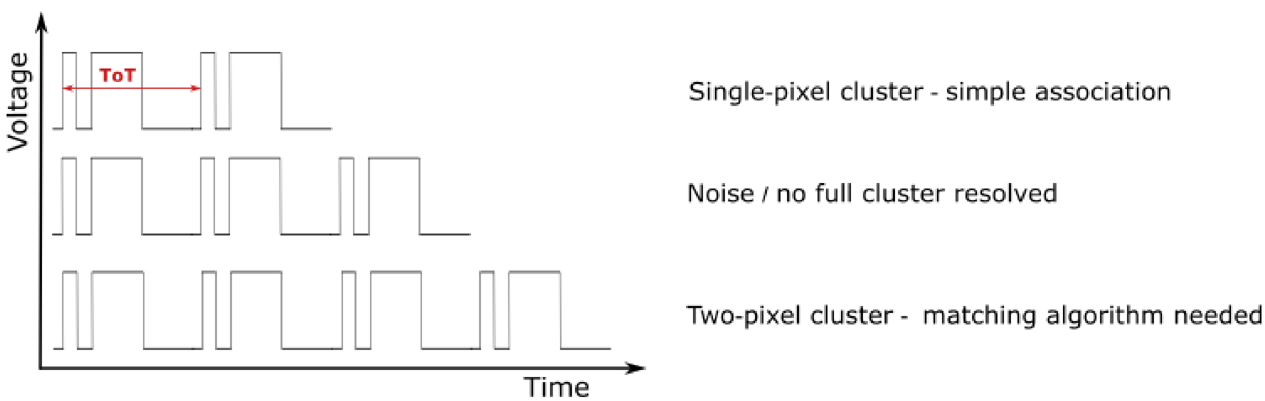

Figure 25: Sketch of the readout-line voltage for three exemplary DPTS events. Not to scale.

In the context of this work, an algorithm was developed in order to effectively match the corresponding trains from one pixel, and to extract all ToTs in a cluster. Its general functionality is explained in Section 3.4.2. Additionally, it features the detection and correction of possible decoding errors, which will be explained in Section 3.4.1.

3.4.1 Decoding Re-evaluation

If the hit-position decoding of a train, which is described in Section 3.3.1, is assumed to be wrong (see Section 3.4.2), its decoding can be re-evaluated. Here, a change in the decoding outcome is enforced.

To quantify the goodness of a certain train decoding, the Center of Gravity distance Δ_{CoG} can be used as indicated in Figure 26. It is defined as the difference of the train coordinate $(PID_{train}, GID_{train})$ to the associated calibration point $(PID_{calib}, GID_{calib})$ in GID/PID space:

$$\Delta_{CoG} = \sqrt{(PID_{train} - PID_{calib})^2 + (GID_{train} - GID_{calib})^2} \tag{13}$$

The larger Δ_{CoG}, the likelier the nearest-neighbour search in the hit-position decoding leads to a wrong pixel.

If the decoding of a train needs to be reevaluated, the corresponding calibration map will be modified such that the initially associated calibration point will be removed from the map. This leads to a change in the acceptance regions of the neighbouring calibration points as depicted in Figure 26 (dotted lines). By decoding the hit position of the train again using the modified calibration map, the train will result in another pixel position. This re-evaluation is utilized in the train association algorithm, which will be described in Section 3.4.2.

3.4.2 Train Association Algorithm

A sketch of the train-matching algorithm is provided in Figure 27. A DPTS event, which consists of a certain amount of pulse trains on the readout line, is recorded with the setup described in Section 4.3. The edges of the digital signal are saved.

At the beginning of the event processing, four cross-checks on the event quality are performed, shown in orange in the flow chart. First, the number of trains in the event is counted. If the event consists of zero or an odd number of trains, the assumption of decoding the first half of the trains with a rising edge calibration and the second half of the trains with a falling edge calibration can not be used. Therefore, the event will be discarded. Second, it will be checked if any trains in the event are not properly resolved. This is the case if not exactly four edges are resolved in any train of the event. Also in this case, the event will be discarded. Furthermore, a simple check for possible pile-up is carried out. Derived from Figure 18 in [21], an event is considered a possible subject to pile-up when the last edge of the first half

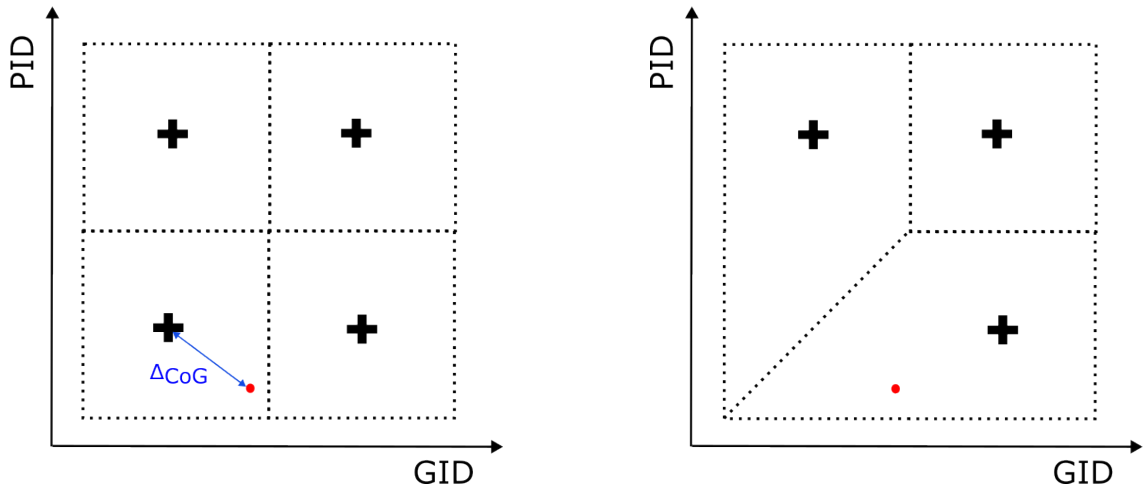

(a) Before re-evaluation

(b) After re-evaluation

Figure 26: Sketch of the decoding re-evaluation for an exemplary 2 × 2 pixel matrix.

of the trains arrives later than 3 μs after the trigger. In this case, this edge likely arose from another event captured in the same waveform. Those events are discarded as well. Last, it is detected if two or more trains possibly collided on the readout line. If the collision results in poorly resolved edges, the event is already discarded by failing the aforementioned condition of four edges per train. However, the collision can also lead to a merging of the pulse trains maintaining well-resolved edges. This way, the edges are not ordered by their corresponding train any more. Therefore, wrong PID and GID values are extracted. The determined values are then significantly smaller compared to events with correctly determined PID and GID. Thus, a lower cut on the PID and GID value can be applied. If a recorded PID value is smaller than the lowest PID value in the used calibration map (see Section 3.3.1) minus a safety margin, the event is discarded as a possible train clash. The margin is defined as the observed mean distance of the calibration points in the PID dimension. An analogue cut is applied to the GID values.

After the initial quality check of the recorded events, all trains of the remaining events are decoded with the corresponding calibration map (rising-edge or falling-edge calibration) into a pixel position. Here, errors in the position decoding of a train can occur (see Section 3.3.1). This way, it can happen that for the same signal, the rising edge train yields a different pixel position than the falling edge one. The algorithm differentiates the events now in three cases, depending on the relative number of matchable pixel positions: a full, a partial and no match.

An event is considered a full match if the rising-edge train yields the same pixel position as the corresponding falling-edge train for every signal in the event. For example, a two-pixel

cluster event is considered. Here, two rising-edge and two falling-edge trains will be observed on the output line. They are decoded into a set of four pixel positions. As described in Section 3.4, the first half of the trains is associated with rising edges, while the second half is related to falling edges. Representing the event as a set of decoded pixel positions a and b, a fully matched event would be e.g. $[a, b, b, a]$. Here, the rising and falling edge of pixels a and b can be matched directly and no further processing of the event is required.
A partly matched event has at least one firing pixel with exactly two corresponding trains, but also a number of trains which result in different pixel positions. In the above-mentioned representation, this would be e.g. $[a, b, c, a]$. Here, solely the rising and falling edge of pixel a can be matched directly. For the remaining trains b and c, a further processing is required.
An event with no match has just one train associated with every pixel, e.g. $[a, b, c, d]$. Here, no trains can be matched without further processing.

Partly matched events are likely to contain trains with a wrong hit-position decoding. To identify possible decoding errors, the structure of the partly matched event will be differentiated into events with a repetition and events without a repetition. Here, a repetition is defined as the case where two or more times the same pixel is decoded on either the first (rising edge) and/or the second (falling edge) half of the event, e.g. $[a, a, b, a]$. Other events (e.g. $[a, b, c, a]$) will be associated with no repetition. An event with no match will also be considered an event without repetition.

Non-repetitive events are checked for the trains most likely to be decoded wrongly. These are assumed to be the half of the unmatched trains with the highest Δ_{CoG}. Their decoding is re-evaluated as described in Section 3.4.1.

Repetitive events will likely contain a decoding error on the side where the repetition occurs since e.g. two rising edges are observed for the same pixel. Accounting for this, wrong decoding is suspected in the repetitive trains with the largest Δ_{CoG} among them. Those trains will then be re-evaluated. Only the repetitive train with the lowest Δ_{CoG} is not re-evaluated. If the re-evaluation of the repetitive trains leads to a full match, no further processing is required. However, if the repetitions are resolved, but unmatched trains still remain in the event, a second re-evaluation stage has to be carried out. For this, half of all unmatched trains will be re-evaluated again, whereby the trains with the highest Δ_{CoG} are chosen. Trains which were re-evaluated already to resolve a repetition are not re-evaluated again in this stage.

After the decoding re-evaluation of the non-repetitive as well as of the repetitive trains, it is checked if the event is now fully matched. If just one rising edge and one falling edge train are left unmatched, they are assumed to arise from the same pixel. Those trains will be associated to the hit-position of the train with lower Δ_{CoG}. If more than two trains remain unmatched, the event will be discarded.

The performance of the described train-matching algorithm for ${}^{55}_{26}$Fe and in-beam data will be shown in the corresponding Sections 4.4.3 and 5.3.4, respectively.

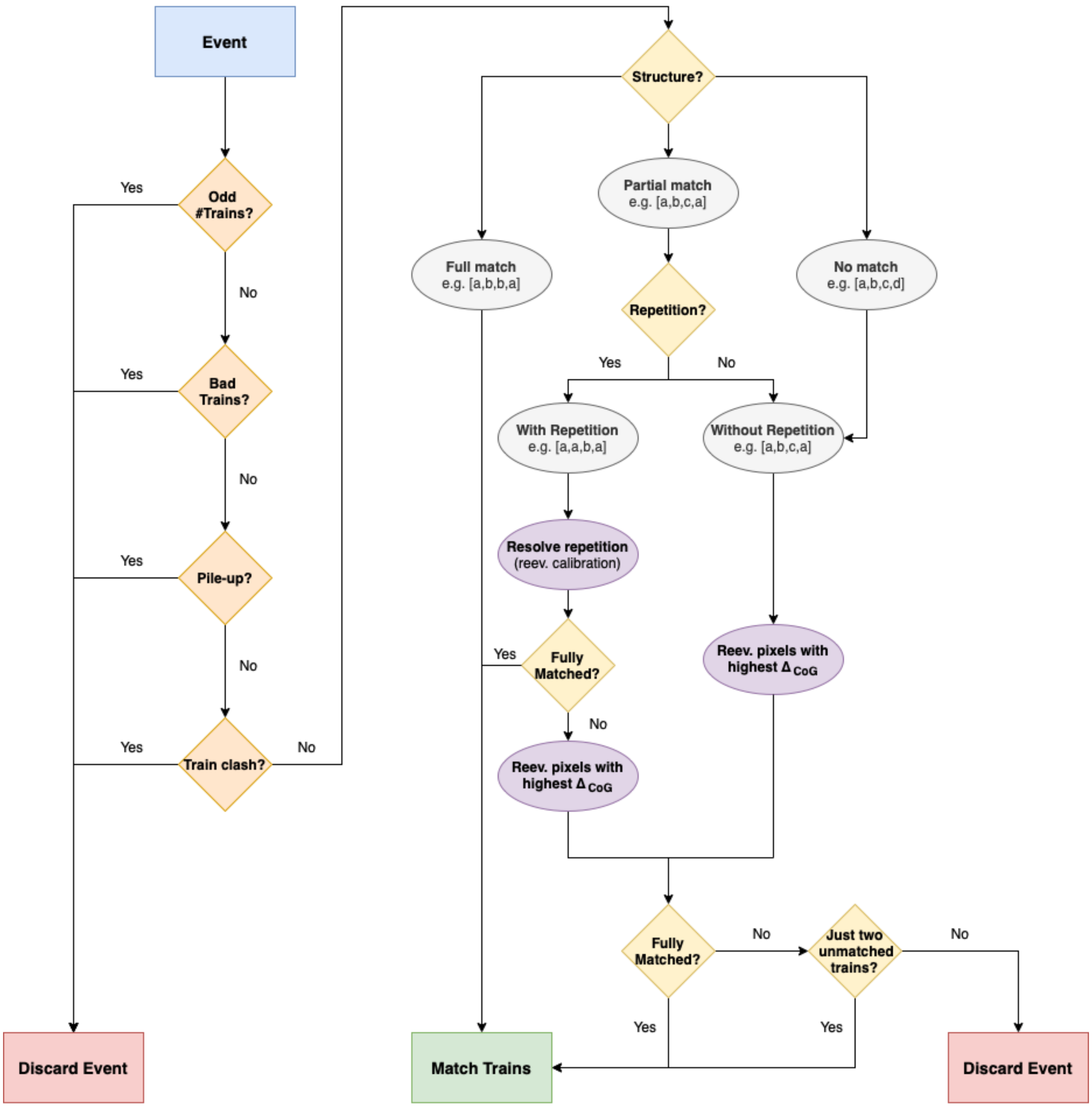

Figure 27: Flow chart of the DPTS train-matching algorithm.

4 $^{55}_{26}$Fe response

The particle response of MAPS can be studied, besides in-beam tests, also in a laboratory environment utilizing radioactive sources. An $^{55}_{26}$Fe-source is used in this work due to its X-ray emissions with energies well suited for the DPTS's operating range. Their well-known energies are expected to be fully deposited in the sensor. In the following sections, the $^{55}_{26}$Fe source characteristics and the detection of its X-rays in silicon will be discussed. Furthermore, measured $^{55}_{26}$Fe spectra for DPTS will be analyzed and an exemplary energy calibration of the sensor will be performed. Additionally, the $^{55}_{26}$Fe spectrum will be shown for different cluster-sizes of the DPTS. Moreover, the seed pixel spectra for non-irradiated and NIEL-irradiated devices will be compared. This analysis does not aim to provide a complete picture of DPTS's response to $^{55}_{26}$Fe, but will show the important methods and steps of the $^{55}_{26}$Fe spectrum analysis regarding the energy-straggling evaluation of DPTS exemplarily. Thereby, particular attention is paid to the so-obtained energy calibration. A more detailed analysis aiming at fully characterising DPTS's $^{55}_{26}$Fe response over a larger parameter space can be found in [8].

4.1 $^{55}_{26}$Fe Source Characteristics

For the source measurements in this work, an $^{55}_{26}$Fe source is used. It decays by electron capture with a half-life time of 2.73 years [23]. The decay follows the reaction:

$$^{55}_{26}Fe + e^- \rightarrow^{55}_{25} Mn + \bar{\nu}_e \tag{14}$$

The electron capture leads to a vacancy in the K-shell of the resulting $^{55}_{25}Mn$ atom. Via de-excitation of an electron from the L or M shell of $^{55}_{25}Mn$, a photon will be released. Depending on its origin shell L or M, it will be referred to as a Mn-K_α and Mn-K_β emission, respectively. Resulting from the spin-orbit characteristics of the de-exciting electron, both Mn-K_α or Mn-K_β have substructures, denoted here using the additional number indices, e.g. Mn-$K_{\alpha 1}$ or Mn-$K_{\alpha 2}$. Additionally, a continuous background is apparent due to Auger electrons originating from the K or L shell ($e_{Auger,K}$ or $e_{Auger,L}$) and Bremsstrahlung. A summary of the emitted energies together with their relative probability is given in Table 2. For the study with DPTS, the differences in energy levels due to spin-orbit characteristics can be neglected since they cannot be resolved.

4.2 $^{55}_{26}$Fe X-ray Detection in Silicon

In Silicon, the absorption of the in Table 2 reported X-Ray emissions is dominated by the photoelectric effect [8]. With a photoelectric absorption coefficient at 6 keV of $1.46 \cdot 10^2 \frac{cm^2}{g}$ [25] and a silicon density of $2.32 \frac{g}{cm^3}$ [20], the corresponding mean range is 30 μm. This is below DPTS's sensor thickness of 50 μm, and therefore it can be assumed that all photons

Transition	Energy (keV)	Emissions per 100 disintegrations
$Mn\text{-}K_{\alpha 1}$	5.90	16.57 ± 0.27
$Mn\text{-}K_{\alpha 2}$	5.89	8.45 ± 0.14
$Mn\text{-}K_{\beta 3}$	6.49	3.40 ± 0.01
$Mn\text{-}K_{\beta 5}$	6.54	
$e_{Auger,L}$	0.47 - 0.67	140.2 ± 0.8
$e_{Auger,K}$	4.95 - 6.53	60.1 ± 0.5

Table 2: Selection of $^{55}_{26}$Fe transition energies and the corresponding abundances. Values taken from [24].

are stopped within the device.

By the photoelectric effect, electrons of the silicon atoms are liberated. These electrons then have an energy equal to the energy difference between the incident X-ray and the binding energy of the respective atom shell. The here relevant energy levels of ^{14}Si are reported in Table 3. Due to the small stopping range of electrons in silicon (1.5 μm for a 10 keV electron with a mean range of $3.46 \cdot 10^{-4}\,\frac{g}{cm^2}$ [26]), it can be assumed that most of the released electrons deposit their full energy in the sensor.

Atom	K-1s (eV)	L-2s (eV)	L-2p (eV)	M (eV)
^{14}Si	1839	150	100	8

Table 3: Energy levels of the K, L and M shell of ^{14}Si. Values taken from [27, 28].

Photons interacting with electrons in the M-shell lose just a negligible amount of energy to free the electron. Therefore, they have approximately the same energy as the incident photon. In contrast, the amount of energy transferred to electrons of the L-shell is not negligible. However, the consecutive rearrangement of the remaining electrons in the atom produces additional X-rays. These ultimately lead to a total energy release in the sensor comparable to the incident photon energy [8]. Furthermore, the incident X-ray can interact with the K-shell, where the binding energy plays an even more important role. The state of the freed electron will be filled with an electron from the L_{2p} shell according to the angular momentum selection rule. By this, a fluorescence photon will be released creating a characteristic silicon fluorescence peak Si_{fl} at an energy of $Si\text{-}K_{1s} - Si\text{-}L_{2p} = 1.74\,\text{keV}$ [29]. In the case of the fluorescence photon escaping the active volume of the sensor, the detected energy will be decreased by 1.74 keV. This can in principle happen with initial energies of $Mn\text{-}K_{\alpha}$ or $Mn\text{-}K_{\beta}$. This leads to two additional peaks in the spectrum, which are here referred to as the silicon escape peaks $Si_{esc,\alpha}$ and $Si_{esc,\beta}$. However, due to the low abundance of $Mn\text{-}K_{\beta}$

emissions, only the $Si_{esc,\alpha}$ is visible in the $^{55}_{26}$Fe spectrum recorded with DPTS (see Section 4.4.2). Therefore, it will be simply referred to as Si_{esc} in this work.
A summary of the expected peaks in the DPTS $^{55}_{26}$Fe spectrum is provided in Table 4.

Peak	$Mn\text{-}K_\alpha$	$Mn\text{-}K_\beta$	Si_{esc}	Si_{fl}
Energy (keV)	5.90	6.51	4.16	1.74

Table 4: Expected peaks in the DPTS $^{55}_{26}$Fe spectrum.

4.3 Experimental Setup with an $^{55}_{26}$Fe Source

For measurements with a $^{55}_{26}$Fe source, the setup depicted in Figure A.1 in the Appendix is utilized. It adds an aluminium mockup to the setup described in Section 3.2.4. In this way, the source can be stably placed above the centre of the DPTS at a precise distance of 12 mm. Furthermore, it allows for easier light shielding and integrates water cooling for the chip.

4.4 $^{55}_{26}$Fe Spectrum Analysis

The following sections present the analysis of the $^{55}_{26}$Fe response of DPTS with a data set containing one million triggers recorded at a threshold setting of around 100 e^- at a controlled temperature of 20 $°C$, unless explicitly stated otherwise. After correcting for inter-pixel ToT variations, an exemplary energy calibration using the spectrum's peaks will be performed. This shows the linearity of DPTS's front-end regarding the ToT in the energy range of the $^{55}_{26}$Fe emissions. Further, a simplified method implemented to perform automatized energy calibrations will be explained and its result will be compared to the full energy calibration method validating the simplification. Additionally, an overview of the clustering performance of the DPTS on $^{55}_{26}$Fe data, and of the important cluster energy quantities used in this work is given. Besides this, the spectrum of a non-irradiated sensor and a 10^{15} 1MeV $n_{eq}\,cm^{-2}$ NIEL-irradiated device will be compared. Finally, a more academic but instructive view of the contribution of different cluster-sizes to the $^{55}_{26}$Fe spectrum will be provided.

4.4.1 ToT-calibration

Figure 28 shows in red the direct DPTS ToT response to $^{55}_{26}$Fe. Here, only single-pixel cluster events are shown. They provide the most direct view of the charge collected in the process and are expected to result in the best energy resolution. The uncalibrated spectrum features the $Mn\text{-}K_\alpha$ peak merged with the $Mn\text{-}K_\beta$ peak around a ToT value of 14.5 μs and a characteristic 'edge' just above the threshold value. The latter peak is expected to arise from substrate contributions and will be discussed in Section 4.4.5.

The resolution of the $^{55}_{26}$Fe peaks can be significantly increased by correcting for the interpixel ToT variations using the calibration method described in Section 3.3.4. This way, more peaks of the $^{55}_{26}$Fe spectrum become evident. The ToT calibrated distribution is shown in blue. In all $^{55}_{26}$Fe spectra shown in this thesis, the ToT calibration is applied unless explicitly stated otherwise.

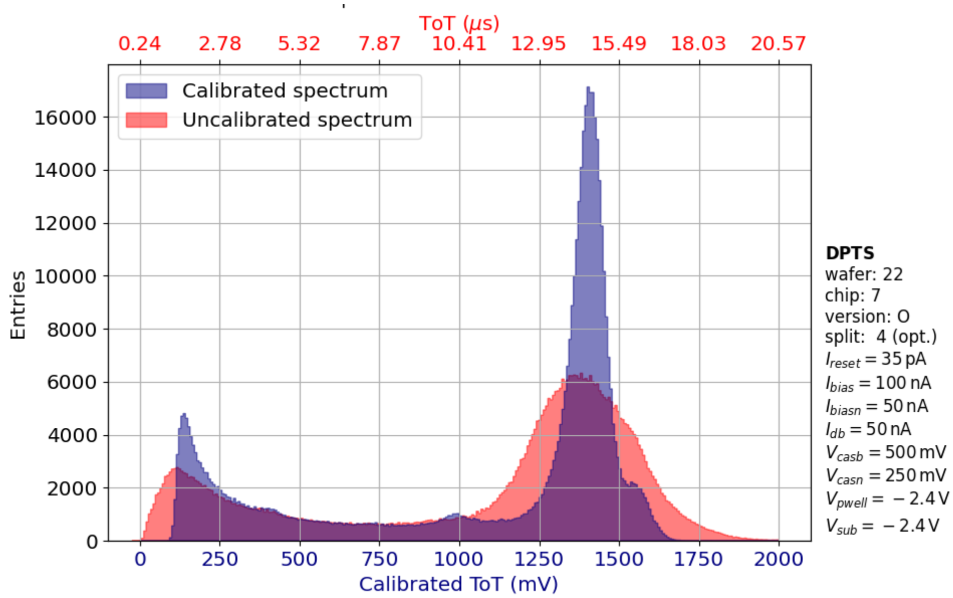

Figure 28: Comparison of the $^{55}_{26}$Fe ToT spectrum before and after ToT calibration.

4.4.2 Energy calibration

The ToT-corrected single-pixel cluster ToT spectrum provides, due to its prominent $^{55}_{26}$Fe peaks, good conditions to establish a ToT-to-energy calibration of the DPTS for a certain operating condition. Since single-pixel clusters are not affected by charge-sharing, they provide the cleanest view of the collected charge in the process. This makes them, after the application of the ToT calibration explained in the previous section, ideal for the extraction of the $^{55}_{26}$Fe peaks. The well-known emissions of an $^{55}_{26}$Fe source, as described in Sections 4.1 and 4.2, lie comfortably in the dynamic range of the DPTS and are therefore a useful tool to establish a relation between the ToT and the deposited energy within the DPTS at a certain operating condition.

To extract the peak positions of the recorded spectrum (depicted in blue in Figure 29), three fits (shown in red in the upper plot) have been carried out. The Si_{fl} as well as the Si_{esc} were empirically fitted with a Gaussian added to a first-order polynomial background:

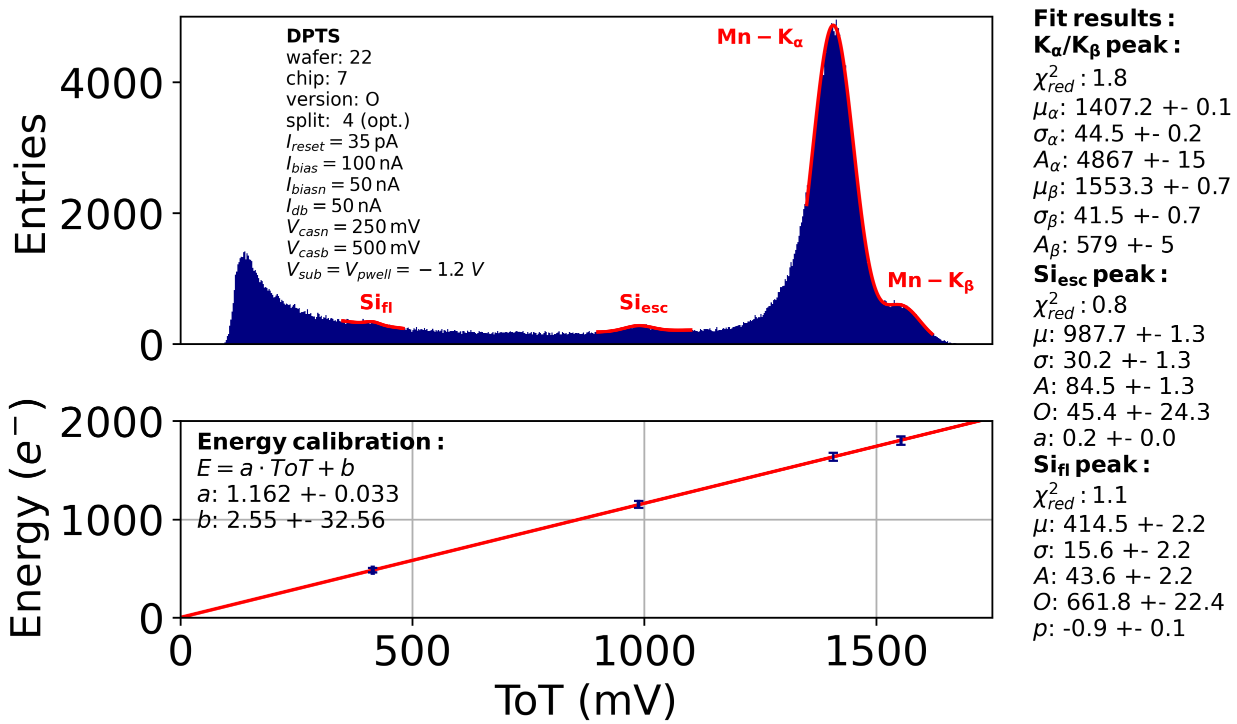

Figure 29: Exemplary ToT to energy calibration of the DPTS using an $^{55}_{26}$Fe source.

$$\#Entries = A \cdot exp\Big(-\frac{(ToT-\mu)^2}{2\sigma^2}\Big) + p \cdot ToT + O \tag{15}$$

Here, A is the amplitude of the Gaussian with mean μ and standard deviation σ. The variable p is the slope, while O represents the offset of the background. All variables except the ToT are treated as free fit parameters. A Poisson error is assumed for the number of entries of every bin. The fit results and the respective fit errors are written on the right side of Figure 29.

Since the energy resolution of the DPTS is too low to resolve the Mn-K_α and Mn-K_β peak completely separate, they are fitted empirically as a sum of two Gaussians. For these peaks, no distinct background contribution is applied. The following fit function was used:

$$\#Entries = A_\alpha \cdot exp\Big(-\frac{(ToT-\mu_\alpha)^2}{2\sigma_\alpha^2}\Big) + A_\beta \cdot exp\Big(-\frac{(ToT-\mu_\beta)^2}{2\sigma_\beta^2}\Big) \tag{16}$$

Here, the same symbols for the Gaussian fit parameters are used as in equation 15, with the additional indices α and β for the contributions of Mn-K_α and Mn-K_β, respectively. As before, the fit results are provided in Figure 29.

The extracted mean values μ_i can now be related to the energies provided in Sections 4.1 and 4.2. For converting the energies from keV to electrons, the mean energy needed to create an electron/hole pair in Silicon of 3.65 eV [20] is used. The resulting dependency is depicted on the lower plot of Figure 29. Using the corresponding fit-uncertainties of μ_i, and applying again a Poisson error on the number of detected electrons, the relationship was fitted linearly. The offset of the dependency was found to be compatible with zero and is therefore neglected in the following analyses. The energy conversion factor a, given by the slope of the relation was found to be for this specific sensor and operational conditions:

$$a = 1.16 \pm 0.03 \frac{e^-}{mV} \tag{17}$$

Since the energy conversion is specific to the used device and its operation conditions, a separate energy conversion is applied for every sensor and condition subject to this work. As the ToT-to-energy dependency was found to be linear across the energy range of the $^{55}_{26}$Fe emissions and its offset can be neglected, only the Mn-K_α peak is used for the following energy calibrations. It is fitted using a Gaussian fit with scalar offset. Pre-fit parameters are automatically determined using the position and height of the bin with maximum entries. The mean is estimated by the position of the maximum bin while the pre-fit values of the standard deviation and scalar offset of the Gaussian are estimated as 5 % and 10 % of the maximum bin height, respectively. The range between 1.5 σ below and 1 σ above the position of the maximum bin is fitted. An example of an automated fit on the same spectrum as shown for the full energy calibration is shown in Figure 29.

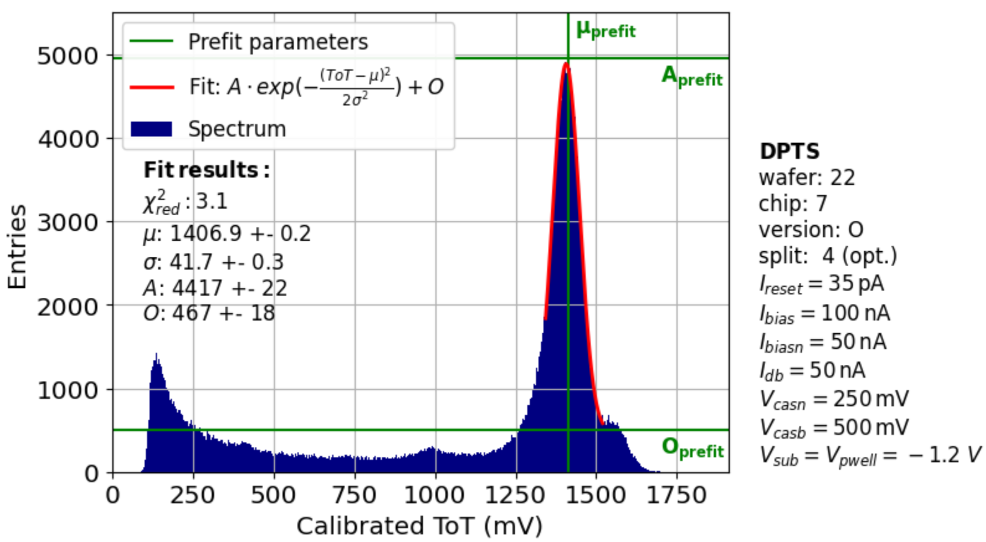

Figure 30: Example of an automatized energy calibration of the DPTS using an $^{55}_{26}$Fe source.

The energy conversion factor $\tilde{a}$ can then be simply obtained by calculating the supposed slope of the ToT-energy dependence using the obtained peak position μ and the origin:

$$\tilde{a} = \frac{E(Mn{-}K_\alpha)}{\mu} \tag{18}$$

Here, $E(Mn{-}K_\alpha)$ is the energy of the $Mn{-}K_\alpha$ emission in electrons. Using this simplified method the energy calibration factor is estimated to be:

$$\tilde{a} = 1.15 \pm 0.03 \,\frac{e^-}{mV} \tag{19}$$

The error is obtained by propagating the Poisson error of the number of released electrons and the fit error of the mean position. The result is in accordance with the result obtained by the full calibration within $1\,\sigma$.

4.4.3 Train Association and Clustering

For the analysis up to now, just single pixel cluster events have been considered. However, getting a more representative picture of the $^{55}_{26}$Fe response of the DPTS also requires accounting for higher cluster-sizes. For this reason, the train association algorithm described in Section 3.4.2 is applied to the $^{55}_{26}$Fe data set already discussed in the previous sections.
The corresponding numbers of trains of the data set are provided in Figure 31. As already explained in Section 3.3.1, two matched trains correspond to one pixel. Therefore, the cluster-size distribution is here implicitly given by the matched trains depicted in shades of green. One can directly see that the DPTS features rather small cluster-sizes mostly around one or two pixels. This characteristic directly results from the fabrication process of the DPTS optimized for single-pixel clusters as explained in Section 3.2.1. In the Figure, dark green refers to the native matching performance, i.e. the directly matched events without applied decoding re-evaluation. This matching usually accounts for around 80 % of the DPTS $^{55}_{26}$Fe events. However, as it can be seen in Figure 32, where the same distribution is shown normalized to the statistic of each number of trains, the native matching performance decreases drastically going to higher cluster-sizes. This is an expected behaviour on the DPTS, since its asynchronous readout is subject to more decoding errors for a higher number of trains. Additionally, the likelihood of train clashes increases. Pile-up is only registered for 4 trains or more, since the smallest event of this kind consists of two single-pixel cluster events with 2 trains each.
In the ideal case of providing a representative view of the DPTS response, including higher cluster-sizes, the matching performance should be similar also for a higher number of trains. Otherwise, the contribution of higher cluster-sizes is always biased by the readout. The train-matching algorithm (see Section 3.4.2), is the current method to at least mitigate the effect of the readout scheme on the clustering. As a result, the overall matching performance of the $^{55}_{26}$Fe dataset shown here was increased from around 80 to 90 %. More important however,

the relative contribution of 2, 3 and 4 pixel clusters can be increased by around 20 %, 25 % and 30 %, respectively.

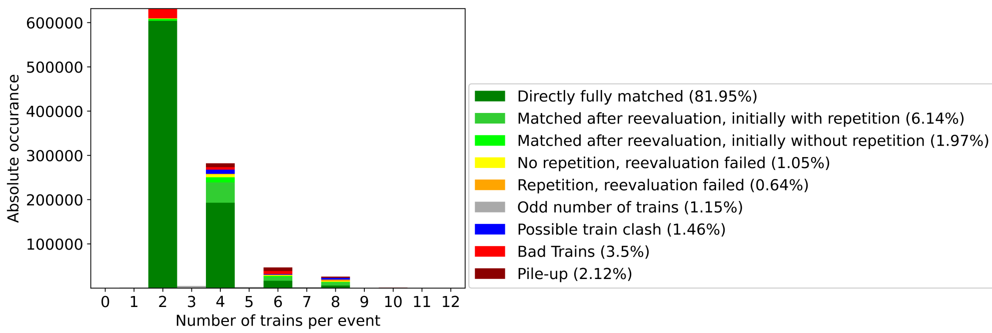

Figure 31: Exemplary train multiplicity distribution together with the absolute train-matching performance on $^{55}_{26}$Fe data.

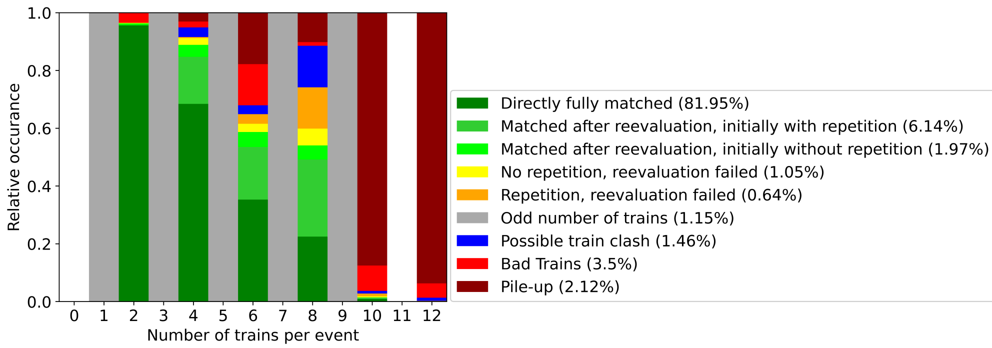

Figure 32: Exemplary relative train-matching performance on $^{55}_{26}$Fe data. Only bins with sufficient statistics of over 100 entries are plotted.

The clustering of the DPTS output provides the possibility to look at the cluster-dependent quantities of the charge collection. One quantity commonly used to consider higher cluster-sizes is the seed pixel ToT. It is defined as the largest ToT in a cluster. Figure 33 compares the seed pixel ToT and the single-pixel cluster spectrum. The difference between these spectra will be further investigated in Section 4.4.5. Another commonly used quantity shown in the figure is the cluster ToT sum, where the ToTs of all pixels in a detected cluster are summed. The cluster sum is per definition larger than the seed pixel ToT which is well visible from the comparison of the spectra. The seed pixel ToT is commonly used to compare the charge collection of different sensors since it is less affected by undetected charges due to a set pixel threshold. For the determination of the total collected charge in a sensor however, the cluster sum provides the better estimation. As already stated in Section 4.4.2, the single-pixel spectrum provides a view on the cleanest events mitigating effects arising from the sensor's pixel nature. This leads to a spectrum with the most defined peaks.

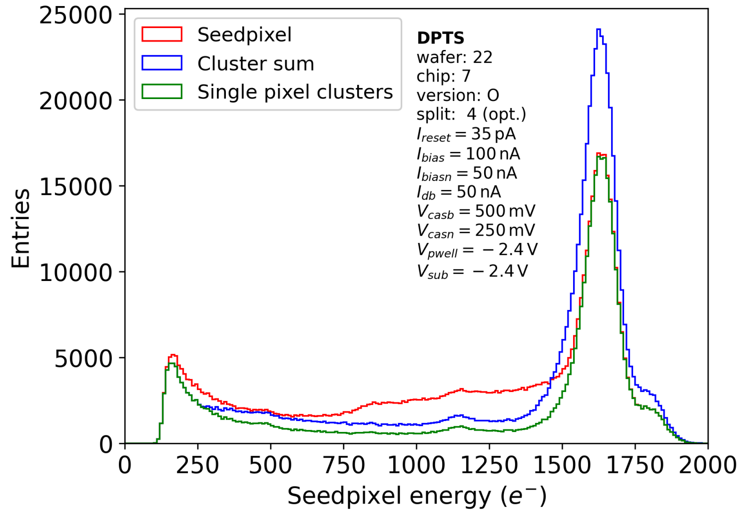

Figure 33: Comparison of an $^{55}_{26}$Fe ToT spectrum looking at different quantities of interest.

4.4.4 Comparison to NIEL Irradiated Sensors

A comparison between the normalized $^{55}_{26}$Fe seed pixel spectra of a non-irradiated device and a device with 10^{15} 1MeV $\mathrm{n}_{eq}\,\mathrm{cm}^{-2}$ NIEL irradiation is provided in Figure 34. To guarantee a non-noisy operation point also for the irradiated device, a threshold of around $200\,e^-$ was chosen for the comparison.
Although it is not possible to draw directly incontrovertible conclusions of the NIEL irradiation impact on the DPTS from this comparison, some effects of it become nevertheless evident. First, the lower tail of the Mn-K_α peak becomes more apparent for the irradiated sensor. Resulting from the NIEL-irradiation effects described in Section 3.1.4, this is an expected effect since lattice defects can lead for example to charge-trapping, preventing parts of the charge from being collected. Second, irradiation results in a poorer energy-resolution becoming evident from the fact that none of the $^{55}_{26}$Fe peaks described in Section 4.2, except for Mn-K_α, are visible in the irradiated spectrum. A reason for this is the fact that bulk damages distort the electric field in the depletion region, e.g. due to trapped charge clouds. Thus, the overall charge collection within the readout time can be reduced dependent on the location of the initially created electron-hole pairs, leading to larger variations in its amount. However, one has to keep in mind that the here shown irradiation level of 10^{15} 1MeV $\mathrm{n}_{eq}\,\mathrm{cm}^{-2}$ lies two orders of magnitudes over the requirement of ITS3 [18]. Following this point of view, the DPTS shows an excellent $^{55}_{26}$Fe response at a comparably high temperature of $20\,°C$,

despite the large irradiation level.

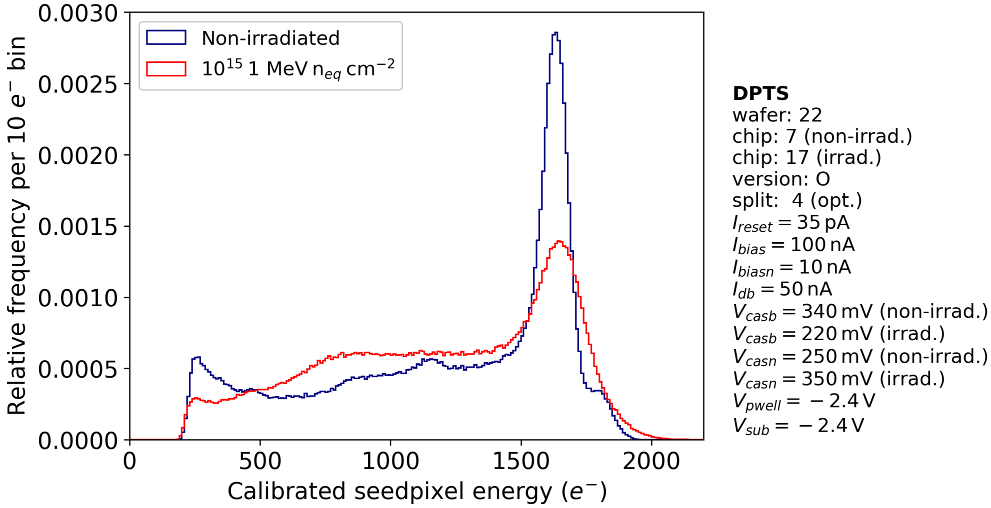

Figure 34: Comparison of $^{55}_{26}$Fe spectra between a non-irradiated and an irradiated device at 200 e^- threshold. The operational parameters shown in the legend are the same for both sensors unless stated otherwise.

4.4.5 Cluster Size Contributions

Using the clustered data set from Section 4.4.3, another instructive view on the $^{55}_{26}$Fe spectrum can be created. Figure 35 shows the corrected seed pixel ToT distribution for all occurring cluster-sizes. Here, the sum of all entries is additionally shown in black. From this representation of the data, a few effects of the charge collection of the pixel sensor become evident. First of all, this view shows that almost all events contributing to the Mn-K_α peak of the seed-pixel spectrum arise from single-pixel clusters. This is an expected behaviour, since larger clusters always imply a charge-sharing between the pixels, leading to smaller seed pixel charges. This tendency can be well seen by looking at the spectra corresponding to larger clusters. In order to explain the cluster contributions on the 'edge' on the left end of the sensor, as well as the shape of the 2 pixel cluster distribution, one has to take a look at the minimum seed pixel signal which can be obtained for a given cluster-size.
The minimum possible seed pixel signal S_{min} for a given deposited charge Q fully collected in the sensor can be for cluster-sizes ≥ 2 roughly and qualitatively modelled according to [7] as:

$$S_{min}(CS) = \frac{Q - Thr\,(CS_{max} - CS)}{CS} \tag{20}$$

Here, CS refers to the cluster-size of the distribution. CS_{max} is the maximum cluster-size observed in the data set. In this case, $CS_{max} = 4$. Thr is the sensor's threshold and accounts for the fact that no charge below Thr is collected. Here, $Thr \approx 100\,e^-$. For the collected charge Q, the in Section 4.4.2 obtained value for the most abundant peak, the Mn-K_α peak, is used ($\approx 1625\,e^-$). This way, $S_{min}(CS)$ was estimated to be approximately $715\,e^-$, $510\,e^-$ and $410\,e^-$ for the cluster-sizes 2, 3 and 4, respectively. Collected charge below $S_{min}(CS)$ can therefore not be explained by contributions from the epitaxial layer, but match such from the substrate, where the assumption of fully collected charge does not hold any more [7]. Substrate contributions also explain the 'edge' around the threshold value. Also here, single-pixel clusters mostly contribute to it. However, charge-sharing over larger clusters leads to too small contributions to overcome the pixel threshold and is therefore not visible in the spectrum.

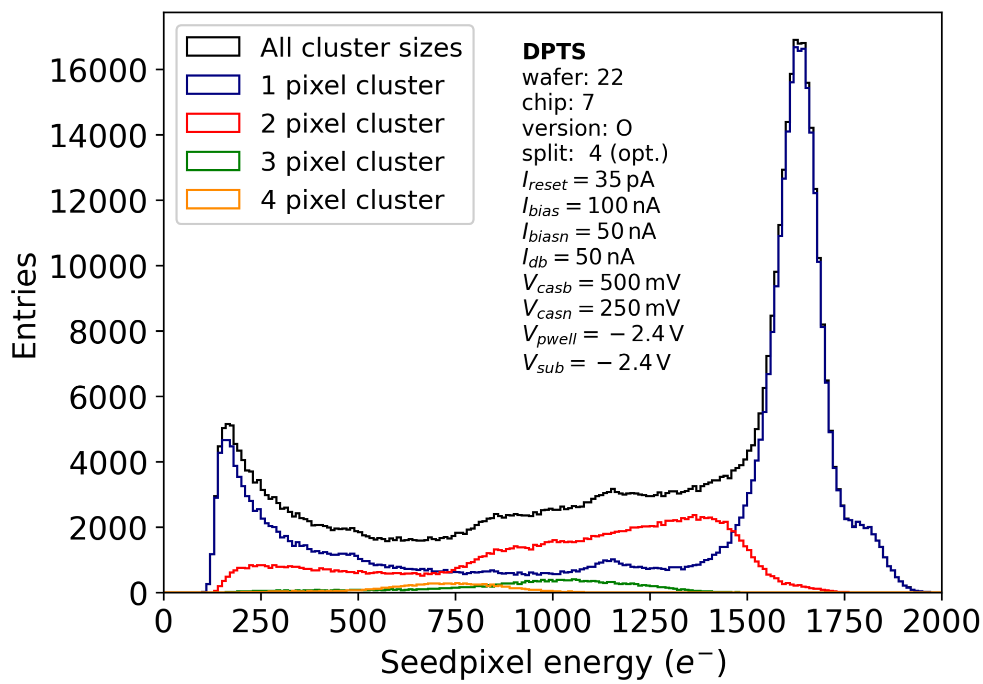

Figure 35: Seed pixel $^{55}_{26}$Fe ToT spectrum of the DPTS for all cluster sizes.

5 Study of In-beam Energy-straggling Distributions

Besides studying the charge collection of MAPS using radioactive sources, energy-straggling distributions can be obtained to investigate the sensor's response to a monoenergetic particle beam. In the following Sections, models for the mean energy loss of light and heavy particles are described briefly. Further, the commonly used models for energy-straggling in the case of different absorber thicknesses will be explained.
Afterwards, the analysis procedure will be described and demonstrated on an exemplary in-beam data set. Furthermore, energy-straggling distributions of a non-irradiated and a 10^{15} $1\mathrm{MeV}\,\mathrm{n}_{eq}\,\mathrm{cm}^{-2}$ NIEL irradiated device will be compared. Moreover, the active layer thickness of the DPTS will be estimated from the most probable value of the energy-straggling distribution. Finally, the energy-straggling distributions at different incident beam angles will be investigated. The result can be used to obtain an additional estimation of the active layer thickness.

5.1 Mean Energy Loss of Particles in Matter

A free particle traversing matter will interact with it in different ways. Charged particles predominantly lose their energy through processes such as ionization (or excitation) of surrounding atoms, emissions of Bremsstrahlung and Cherenkov radiation, or through strong interactions with the surrounding nuclei [20]. The amount of lost energy in a certain reaction depends on the type and energy of the charged particle and the absorber material. Since the energy loss is a statistical process, as it will be further discussed in Section 5.2, its amount can not be predicted particle-by-particle. However, the underlying processes are well understood and therefore, the statistical energy loss is described with a high accuracy. For simplification, it is often referred to as the mean energy loss when describing the deposited energy in the material. The following two Sections provide a brief overview of the common models for the mean energy loss $\langle \frac{dE}{dx} \rangle$ per unit length in matter, separately for heavy and light particles. The statistical energy-straggling will be discussed in Section 5.2.

5.1.1 Bethe-Bloch Model

For heavy charged particles in the region of $0.1 \lesssim \beta\gamma \lesssim 1000$, the mean energy loss traversing a medium is described by Equation 21 with an accuracy of a few percent [30].

$$-\left\langle \frac{dE}{dx} \right\rangle = (4\pi N_A r_e^2 m_e c^2)\, z^2 \frac{Z}{A} \frac{1}{\beta^2} \left[\frac{1}{2} ln \left(\frac{2 m_e c^2 \beta^2 \gamma^2 W_{max}}{I^2} \right) - \beta^2 - \frac{\delta(\beta\gamma)}{2} \right] \tag{21}$$

Here, the following parameters and constants are used:

- N_A: Avogadro's number
- r_e: classical electron radius

- m_e: rest mass of the electron
- c: light velocity in vacuum
- z: charge of the particle in terms of the electron charge
- $\frac{Z}{A}$: ratio of protons and nucleons in the material
- $\beta = \frac{v}{c}$: relative velocity of the particle
- γ: Lorentz factor
- I: mean excitation and ionisation potential of the absorber material
- $\delta(\beta\gamma)$: density-effect correction

The maximum energy transfer W_{max} for a point-like particle with mass $M \gg m_e$ due to kinematics is, according to [30], given by:

$$W_{max} = \frac{2m_e c^2 \beta^2 \gamma^2}{1 + 2\gamma m_e/M + (m_e/M)^2} \tag{22}$$

The Bethe-Bloch stopping power for different materials as a function of the $\beta\gamma$ value for a traversing particle is shown in Figure 36. The dependency decreases for $\beta\gamma \lesssim 3$ proportional to $\frac{1}{\beta^\alpha}$, where α is approximately 1.7-1.5 and diminishes with increasing atomic number Z of the material [30]. The function has a global minimum around $\beta\gamma \approx 3 - 4$. In this regime, particles are commonly referred to as Minimum Ionizing Particles (MIPs). As the logarithmic term of Equation 21 increases, the dependency rises accordingly. To this rise, two major effects contribute. Around two-thirds of the rise is introduced by the relativistic flattening of the electric field leading to an increasing lateral field component and thus to a higher energy loss [30]. Here, the density effect correction $\delta(\beta\gamma)$ accounts for polarization of the medium due to the higher fields counteracting the logarithmic rise towards higher energies [30]. The remaining third of the rise is explained by the increase of $W_{max}(\beta\gamma)$ [30]. A derivation of the Bethe-Bloch equation and a more detailed discussion of its components and terms is provided in [20].

5.1.2 Berger-Seltzer Model

For the determination of the mean energy loss of light particles, two additional effects not included in the Bethe-Bloch model have to be taken into account. First, Bremsstrahlung plays a significant role and needs to be included in the model. Second, incident electrons can be subject to Fermi pressure, while incident positrons annihilate with the surrounding electrons. Furthermore, scattered electrons are indistinguishable from the ones in the material, which is not the case for positrons. This leads to slightly different energy losses for electrons and positrons. According to [31], the energy loss for light particles can be modelled as:

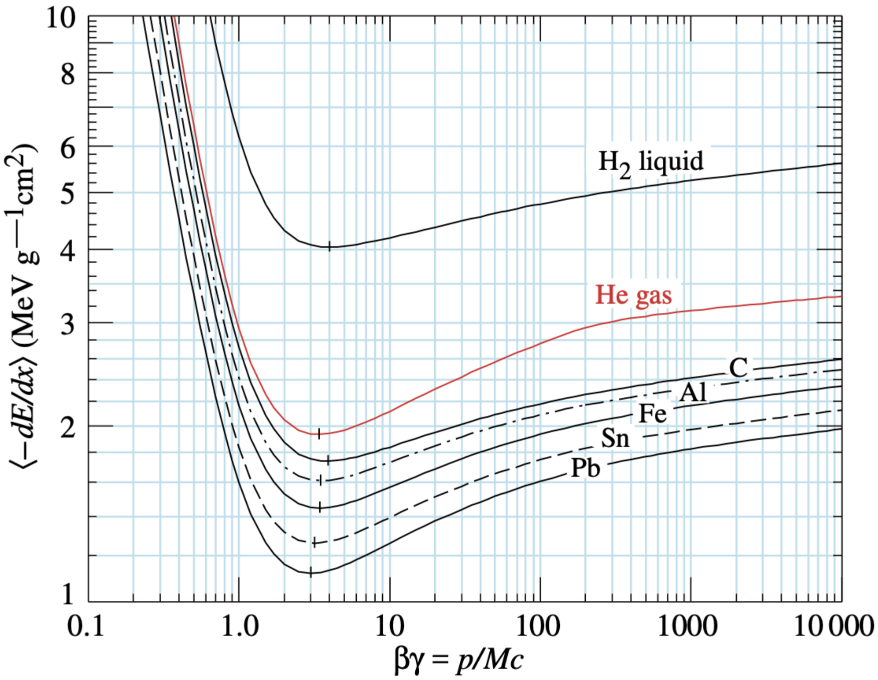

Figure 36: Mean energy loss of a particle in matter for different absorber materials as a function of $\beta\gamma$. Taken from [30].

$$-\left\langle \frac{dE}{dx} \right\rangle = \rho \frac{0.153536}{\beta^2} \frac{Z}{A} \left(B_0(E_{kin}) - 2log\left(\frac{I}{m_e c^2}\right) - \delta(\beta\gamma) \right) \tag{23}$$

with the momentum dependent stopping power $B_0(E_{kin})$. Further details on the model can be found in [31].

5.2 Energy-straggling of Particles in Matter

Up to now, solely the mean energy loss of particles in silicon was discussed. However, even a mono-energetic beam will not result in the same energy loss per particle. This effect arises due to statistical fluctuations in the number of interactions N taking place in the medium and in the transferred energy per process. The theoretical calculation of the underlying distribution, in this work referred to as energy-straggling distribution, is not trivial and the chosen method usually depends on the absorber thickness. The following Section aims to provide an overview of commonly used approximations for three cases: thick, thin and very thin detectors. It has to be noted that these three cases are not strictly defined to certain thickness ranges. Rather, they will use different approximations based on N to derive their model. The explanations of the Gaussian and Landau theory in the following two Sections are mainly based on [32].

5.2.1 Gaussian Model

In the case of relatively thick absorbers, the total number of interactions N of a traversing particle in the detector is very large. Based on this, the energy-straggling can be approximated as a Gaussian. This is justified by the application of the Central Limit Theorem (CLT). It states that for N random variables with the same underlying distribution, their sum approaches a Gaussian limit for $N \to \infty$. In this case, the total energy deposited in the sensor will be treated as the sum of N single collisions with energy loss δE. Here, the assumption of a negligible velocity change in every collision is made to fix the velocity-dependent collision cross-section. According to this, the energy-straggling distribution f_G will be of the form:

$$f_G(\Delta, \epsilon) \propto \left(\frac{-(\epsilon - \bar{\epsilon})^2}{2\sigma^2} \right) \tag{24}$$

Here Δ denotes the thickness of the absorber, while ϵ and $\bar{\epsilon}$ refer to the overall and mean energy loss, respectively. The standard deviation σ for heavy particles is given through:

$$\sigma^2 = \left(\frac{1 - \beta^2/2}{1 - \beta^2} \right) \cdot \left(4\pi N_A r_e^2 (m_e c^2)^2 \rho \frac{Z}{A} \Delta \right) \tag{25}$$

The first term relates to relativistic kinematics with β being the relative velocity of the particle with respect to the speed of light c. N_A represents Avogadro's Number, m_e the mass of the electron and r_e the classical Bohr Radius. The relevant material-dependent parameters are ρ, Z and A and denoting the material's density, its atomic number and atomic weight, respectively. The absorber thickness is denoted as Δ.

5.2.2 Landau Model

For the case of relatively thin detectors, the assumption of $N \to \infty$ does not hold any more and therefore the CLT can not be applied. For this reason, the energy-straggling distribution can not be easily calculated any more. The probability of large energy transfers W in a single collision (cf. Equation 22), leads to an asymmetric distribution with a long tail towards large deposited energies. As a result, the peak of the distribution no longer represents the mean energy loss. Instead, it resembles the most probable value of energy loss (MPV). Theoretical calculations for the case of $k \to 0$, where k is defined as

$$k = \frac{\bar{\epsilon}}{W_{max}} \tag{26}$$

were carried out by L. Landau. [33]. In his calculations, he assumed sufficiently large energy transfers such that the electrons of the absorber can be treated as free. Also, he assumed a constant velocity of the incoming particle. He started his derivation of the energy-straggling by solving the following integral transport equation:

$$\frac{df_L}{dx}(\Delta,\epsilon) = \int_0^\infty P(\delta E)[f(\Delta,\epsilon-\delta E) - f(\Delta,\epsilon)]\, d(\delta E) \tag{27}$$

Here, the term $P(\delta E)\, d(\delta E)$ is introduced as the probability per unit path length to transfer an energy δE to the absorber material. For the generally not known probability distribution P, Landau approximated the following form based on the free electron Rutherford cross-section:

$$P(E) = \frac{\eta}{\Delta} \cdot \frac{1}{E^2} \tag{28}$$

with:

$$\frac{\eta}{\Delta} = 0.1535 \frac{z^2 Z}{A\beta^2}\rho \tag{29}$$

Here, z is the charge of the incoming particle. The Landau distribution is then given by:

$$f_L(\Delta,\epsilon) = \frac{\Phi(\lambda)}{\eta} \tag{30}$$

with the solely on λ dependent function:

$$\Phi(\lambda) = \frac{1}{\pi}\int_0^\infty exp[-u\, ln(u) - u\lambda]\, sin(\pi u)\, du \tag{31}$$

where λ is defined as:

$$\lambda = \frac{1}{\eta}\left[\epsilon - \eta\, (ln(\eta) - ln(\delta E_{min}) + C_{euler}\right] \tag{32}$$

The assumed minimum energy transfer is denoted as δE_{min} and C_{euler} referrs to Euler's constant. The integral function $\Phi(\lambda)$ needs to be evaluated numerically to calculate the respective Landau distribution. A dedicated algorithm for this has been developed in [34].

5.2.3 Bichsel Model

For the case of very thin detection layers, where the total energy loss of a particle in an absorber is comparable to the binding energies of the absorber material, H. Bichsel developed in [35] a dedicated energy-straggling model briefly described in this Section. According to the convolution theory of the respective work, the energy-straggling arises mainly from two sources: the number of collisions n the traversing particle undergoes in the absorber and the energy-dependent cross section $\sigma(E)$ of a single collision.

The probability distribution of n follows a Poisson distribution [36]:

$$P(n) = \frac{(\Delta/\ell)^n}{n!} e^{-\Delta/\ell} \tag{33}$$

Here, the mean free path length ℓ is calculated using $\sigma(E)$ and the number of scattering centers per unit volume N:

$$\ell^{-1} = N \int dE\, \sigma(E) \tag{34}$$

The energy-straggling distribution for the energy loss ϵ after n collisions can be then obtained by the n-fold convolution of the single collision cross section $\sigma(E)^{*n}$:

$$\sigma(\epsilon)^{*n} = \int_0^\epsilon \sigma(E)\sigma^{*(n-1)}(\epsilon - E)\, dE \tag{35}$$

The full energy-straggling function f_B according to the Bichsel-theory is then given by:

$$f_B(\Delta, \epsilon) = \sum_0^\infty P(n)\, \sigma(\epsilon)^{*n} \tag{36}$$

In the Bichsel-theory, the total cross-section $\sigma(E)$ is treated by superimposing contributions from low momentum longitudinal transfers $\sigma_L(E)$, low momentum traversal transfers $\sigma_T(E)$ and large momentum transfers $\sigma_U(E)$:

$$\sigma(E) = \sigma_L(E) + \sigma_T(E) + \sigma_U(E) \tag{37}$$

Explicit forms and the respective derivations of the partial cross sections $\sigma_L(E)$, $\sigma_T(E)$ and $\sigma_U(E)$ are provided in [35].

The total cross-section and its partial contributions are depicted in Figure 37 for 45 GeV/c pions in solid silicon. From here, an important difference between the Bichsel-theory and the in Section 5.2.2 described Landau-theory becomes evident. The Rutherford cross-section, utilized for the Landau theory, is proportional to $1/E^2$ (Equation 28) and appears therefore as a constant in Figure 37. In contrast, the cross-section employed in the Bichsel theory, as stated in Equation 37, takes into account the shell effects of the silicon atom. This consideration results in the presence of three distinct maxima, which are evident in Figure 37.

It becomes evident that the Bichsel cross-section converges to the Rutherford cross-section for larger energy transfers. However, for lower energy transfers, the Rutherford cross section can be just an approximation since the shell-effects start to contribute significantly. Therefore, the energy-straggling in very thin devices ($\mathcal{O}$ ∼10 μm), where the number of collisions is small and thus small energy transfers play statistically a more important role, is found to agree better with the Bichsel model [35]. However, it has to be noted that the energy-straggling distribution according to the Bichsel model in Equation 36 does not obey a closed analytical form. Nevertheless, numerical solutions are provided in [35].

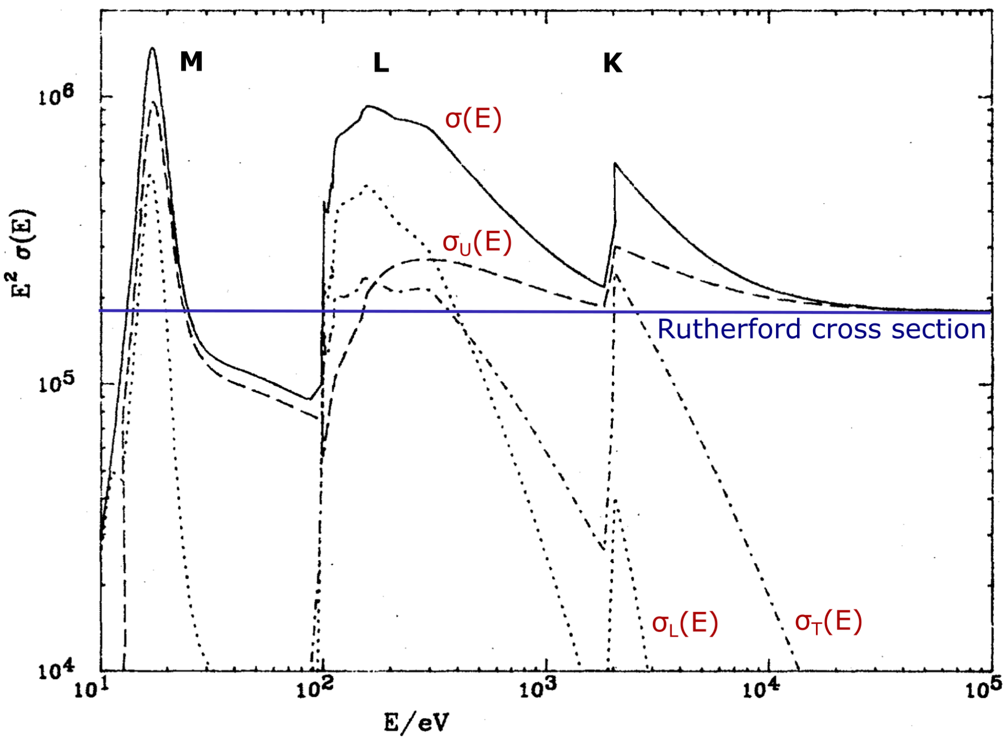

Figure 37: Total and partial cross sections for single collisions of pions with 45 GeV/c momentum in solid silicon. Modified from [35].

5.2.4 Fitting of the Energy-straggling Distributions

For very thin silicon sensors, such as the DPTS with an active layer thickness of approximately 10 μm, the Bichsel theory is more complete than the Landau theory and has shown to reproduce measured energy losses [36, 35]. However, as already stated in Section 5.2.3, the model provides no closed analytical form and can just be approximated numerically. At the time of the conduction of this thesis work, no dedicated software package for fitting data with the Bichsel model was publicly available. Since this thesis does not aim for a physically complete description of the measured energy-straggling distributions but rather focuses on the extraction of the most probable energy loss, the implementation of a numerical approach to approximate the Bichsel model is out of the scope of this thesis.

The Landau model, while being just approximately valid for the active layer thickness of DPTS, can provide nevertheless a sufficient empirical description of the observed energy-straggling (cf. Figure 46). For pions and protons at 10 GeV/c momentum absorbed in silicon (matching the circumstances which will be described in Section 5.3.1), Landau's assumption of $k \to 0$ (cf. Equation 26 & 22) is a valid approximation. To account for the model differences and unwanted underlying sensor effects such as noise, a Landau distribution convoluted with a Gaussian is used. For its numerical approximation, the 'pylandau' software package [37] based on the algorithm described in [34] is utilized in all energy-straggling fits shown in this work.

For all energy-straggling histograms included in this work (e.g. Figure 46), a Poisson error of $\sqrt{n_{bin}}$ is assumed for each bin, where n_{bin} denotes its number of entries. For very low values of n_{bin}, this error is also very small and can bias the fit of the measured data [38]. Here, the fit is very constrained e.g. on the lower and upper end of the distribution, and in consequence not very robust in terms of varying the fit-range as well as the number of bins. This robustness can be improved by iterating the fit procedure [38]. First, a pre-fit of the distribution is carried out using the $\sqrt{n_{bin}}$ error. For the main fit, the $\sqrt{n_{bin}}$ error is replaced by the typically larger $\sqrt{f_{bin}}$ error, where f_{bin} is the value of the pre-fit at the respective bin centre. This way, the bias of the $\sqrt{n_{bin}}$ error on the fit can be mitigated by increasing its robustness. This iterative method is applied for all fits of energy-straggling distributions in this work. The plotted errors in this work always refer to the error of the measured data $\sqrt{n_{bin}}$.

5.3 Data taking and Correction

In the following sections, the analysis steps in order to get from a raw ToT distribution of DPTS to an energy-straggling distribution will be shown. These steps will be demonstrated using in-beam data obtained at CERN's Proton Synchrotron. The raw ToT spectrum will be corrected for inter-pixel ToT variations and afterwards energy calibrated, employing the procedure described in Section 4.4.2. For this, $^{55}_{26}$Fe spectra recorded in the same operational conditions as during the in-beam test are utilized. The data will be clustered, employing the pulse-train-matching algorithm described in 3.4.2. Finally, the algorithm's performance on the in-beam data set will be discussed.

5.3.1 Testbeam Setup at the Proton Synchrotron

The Proton Synchrotron (PS) is part of CERN's accelerator complex and is mainly used as a pre-accelerator for the Super-Proton-Synchrotron (SPS). It has a circumference of 628 m and accelerates not only protons but also various nuclei as well as electrons and antiprotons up to 26 GeV [39]. Besides its usage as a pre-accelerator and host of several experiments, it also provides in-beam test areas e.g. for the characterization of hardware prototypes for future experiments and experiment upgrades.

In July 2022, the in-beam performance of DPTS was measured using a secondary, 10 GeV positive hadron beam mostly consisting of pions. The measurement setup, depicted in Figure 38, consisted of a beam telescope inside a light-tight metal box with taped cut-outs for the beam entrance and exit. The telescope itself consisted of a DPTS Device-Under-Test (DUT), which is the sensor to be characterized, accompanied by five ALPIDE (see Section 2.3.2) reference planes for tracking purposes. Two reference planes were mounted upstream of the DUT, while three reference planes were mounted downstream of it. For triggering, an additional DPTS was placed upstream of the DUT. For a pixel-precise alignment with the DUT, the trigger was mounted on a motorized moving stage. To control the temperature of the DUT, a chiller was installed in the setup. As depicted in Figure A.2 in the Appendix, a cooling jig was mounted on the backside of the DUT. It has to be noted that the tracking information, provided by the ALPIDE planes, is used for efficiency and spatial resolution measurements of the DUT, but is not used for the analyses of this work.

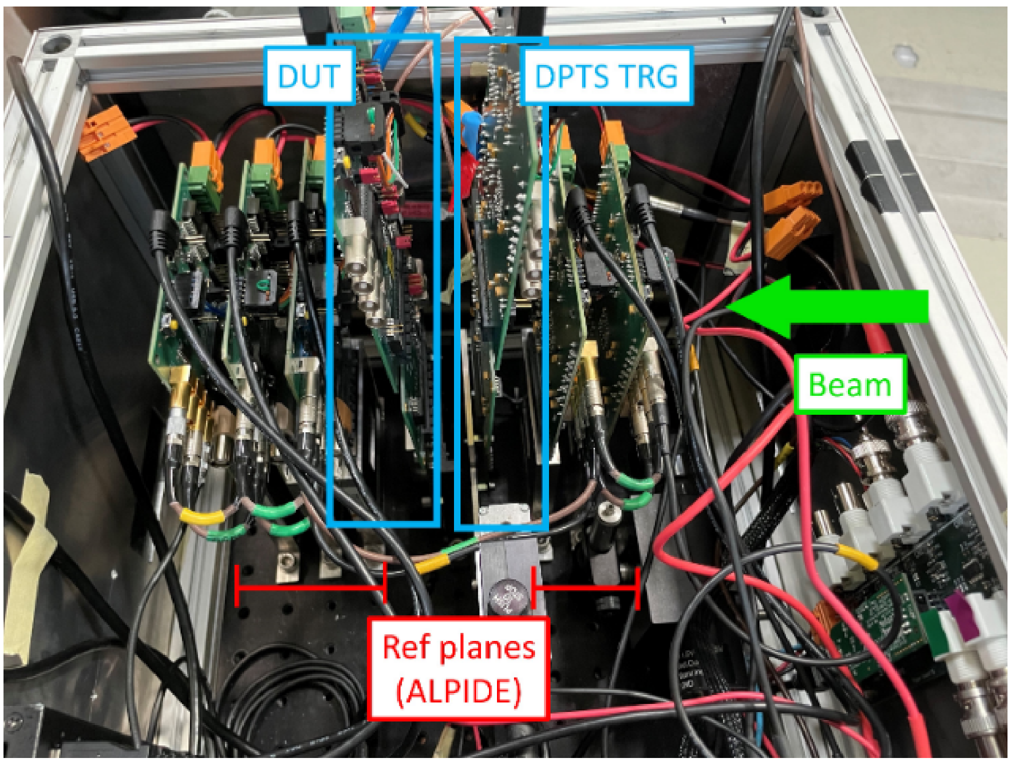

Figure 38: DPTS beam telescope at the PS Testbeam.

5.3.2 Uncorrected Single-pixel cluster ToT Spectrum

The ToT spectra at three different thresholds of $100 \pm 10\,e^-$, $150 \pm 10\,e^-$ and $200 \pm 10\,e^-$ (notation: mean ± RMS), recorded during the beam test at the PS (see Section 5.3.1), are depicted in Figure 39. The thresholds are adjusted by setting V_{casb} (see Section 3.2.2) to values of 500 mV, 420 mV and 340 mV, respectively. The reported threshold values and the respective RMS are determined using the threshold scan method explained in Section 3.3.2.

Since at this step of the analysis, no train association for multi-pixel clusters (see Section 3.4.2) is performed, solely single-pixel clusters are plotted. While the raw ToT spectra provide the most direct view of the DPTS energy output, they do not allow for direct conclusions on the charge collection. For this, the ToT spectrum has to be corrected for variations in the ToT response between the pixels and converted to the collected charge.

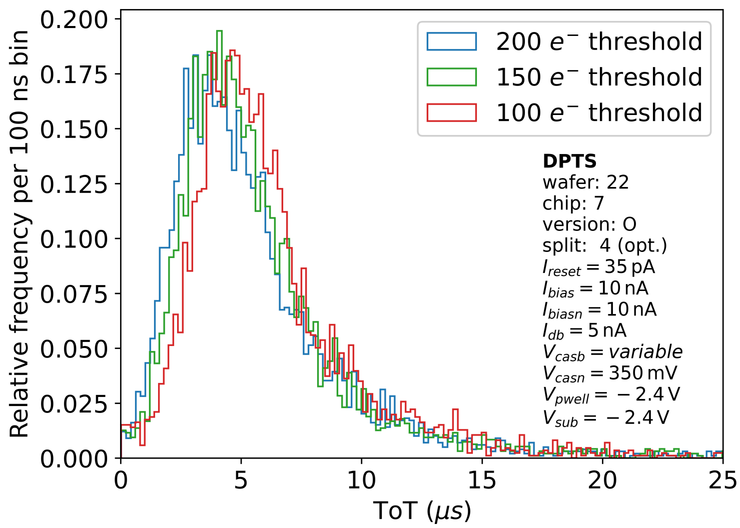

Figure 39: Single pixel cluster ToT spectrum at different threshold values

5.3.3 Single-pixel cluster Energy-straggling Distribution

Analogue to the $^{55}_{26}Fe$ ToT spectra in Section 4.4.1, the raw distribution shown in Figure 39 can be corrected for inter-pixel ToT variations. Additionally, the spectrum can be energy-calibrated utilizing an $^{55}_{26}Fe$ spectrum recorded in the laboratory at the same operating conditions as during the test beam. First, this is important due to the ToT and threshold dependence on the operational parameters as illustrated in [21]. Second, a temperature effect of $0.5\,e^-$ decrease of the sensor's mean threshold (see Section 3.3.2) per degree Celsius in the range of 15 - 40 $°C$ is prominent on non-irradiated DPTSs [21]. To mitigate the latter effect, the sensor was chilled to 20 $°C$ in both, in-beam (Section 5.3.1) and laboratory correction measurements (Section 3.2.4). Using the so-recorded $^{55}_{26}Fe$ spectrum, an energy calibration factor is derived for the specific operating conditions of the corresponding in-beam data. This calibration factor is obtained analogously to the automatized method described in Section 4.4.2.

The resulting single-pixel cluster energy-straggling distributions are depicted in Figure 40a. One can see here that the three distribution shapes agree for values well above the largest threshold of $200\,e^-$, which again underlines the frontend linearity of DPTS in this regime.

From the magnified version of the distribution's lower end, it becomes evident that no energy is detected below the sensor's threshold, substantiating the applied method of ToT-correction (see Section 3.3.4).

However, as already stated for the $^{55}_{26}$Fe spectrum, a view on the single-pixel cluster energy distribution provides only a limited picture of the DPTS's charge collection properties. Clustering is required to obtain cluster-energy distributions, which will provide a better estimate of the total charge collected in the sensor.

5.3.4 Train Association and Clustering

The performance of the train association algorithm, described in Section 3.4.2, on the in-beam distribution with $100\,e^-$ threshold, is shown in the Figures 41 and 42. The general characteristics of the cluster-size distributions and the train-matching performance are similar to the ones already explained for the $^{55}_{26}$Fe data clustering in Section 4.4.3. The native matching performance, i.e. the fraction of events which can be directly matched without applying a decoding re-evaluation, is around 25 % lower for the in-beam data than for the $^{55}_{26}$Fe set. The apparent abundance of higher train numbers for $^{55}_{26}$Fe data arises solely from the difference in the statistics. Here, a number of events which is two orders of magnitude higher than the one collected during the PS July 2022 in-beam test is utilized. The total association performance for the in-beam data was increased from around 60 to 70 % in this example, while the more important relative performance increase for 1, 2, 3 and 4 pixel clusters lies around 5 %, 30 %, 20 % and 20 %, respectively.

5.3.5 Seed Pixel and Cluster Energy-straggling Distribution

The in Section 5.3.4 performed train association enables the view on the seed pixel and cluster sum distribution, as explained in Section 4.4.3 for the example of $^{55}_{26}$Fe data. In Figure 43, the resulting seed pixel energy-straggling distributions are given. As for the single-pixel distribution, one can see a good agreement of the distributions above the threshold as expected from a linear sensor frontend. At their lower end, the distributions are again cut off at the respective threshold value.

5.4 Energy-straggling Analysis for NIEL-irradiated Sensors

Additional to the in Section 5.3 analysed energy-straggling distributions, also a device irradiated to 10^{15} 1MeV $\mathrm{n}_{eq}\,\mathrm{cm}^{-2}$ NIEL-irradiation (see Section 3.1.4) was measured during the PS July 2022 in-beam test (see Section 5.3.1) at the corresponding operating conditions. The data was ToT-corrected, energy calibrated and clustered analogue to the non-irradiated data in Section 5.3. The train-matching performance for irradiated data is provided in Appendix A.3. The resulting distributions are shown in Figure 44.

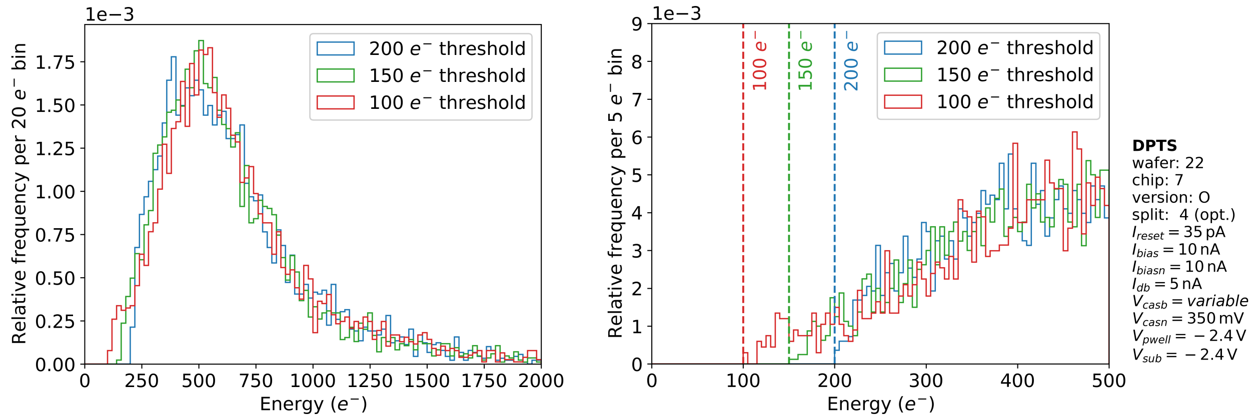

(a) Distribution up to 2000 e^-

(b) Lower end of the distribution up to 500 e^- with the corresponding threshold values highlighted

Figure 40: Single pixel cluster energy-straggling distributions at different threshold values. The operation parameters on the right side are valid for both plots.

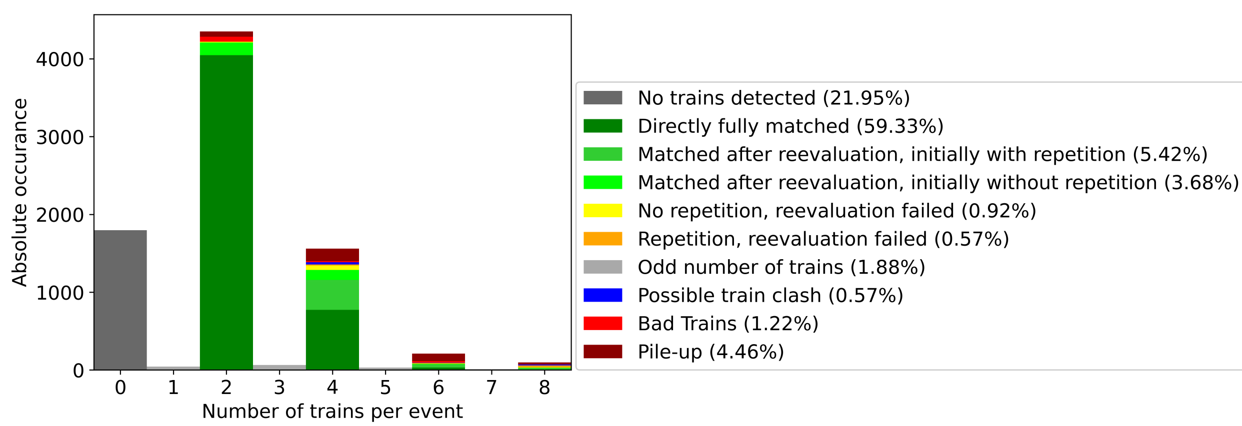

Figure 41: Exemplary train multiplicity distribution together with the absolute train-matching performance on in-beam data for $100\,e^-$ threshold. Only bins with more than 10 entries are plotted

A comparison between the seed-pixel energy-straggling distributions of a non-irradiated and an irradiated device at a threshold of $200\,e^-$ is shown in Figure 45. As already observed and described for the comparison of the non-irradiated and irradiated $^{55}_{26}$Fe spectra in Section 4.4.4, the overall charge-collection reduces with a higher irradiation level. One can see that this effect plays a more important role for charge releases close to the MPV and becomes less evident at higher charge deposits. However, it has to be stressed that the rather low impact of such a high total NIEL-irradiation dose on the energy-straggling distribution at a comparably high room temperature of $20\,°C$ strongly underlines the radiation hardness of

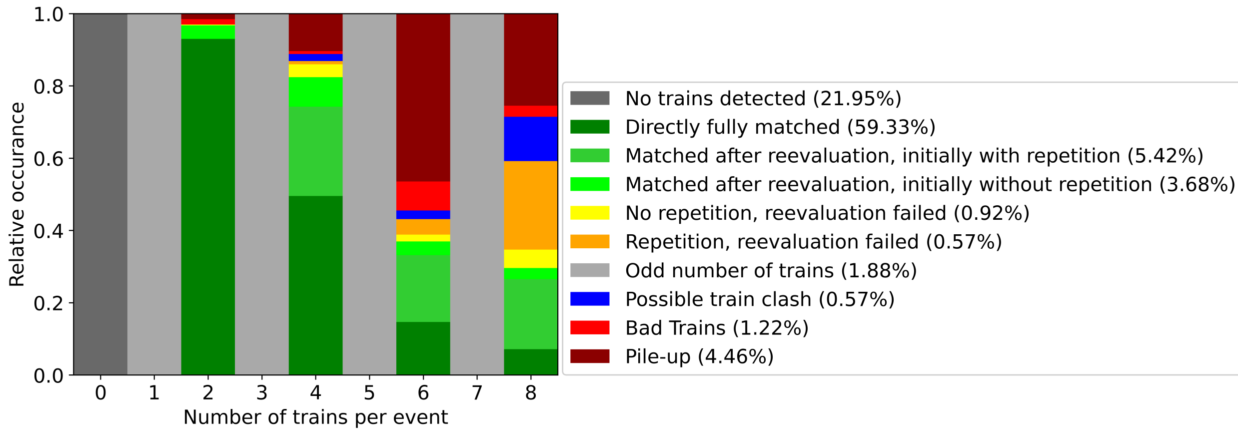

Figure 42: Exemplary relative train-matching performance on in-beam data for $100\,e^-$ threshold. Only bins with sufficient statistics over 10 entries are plotted.

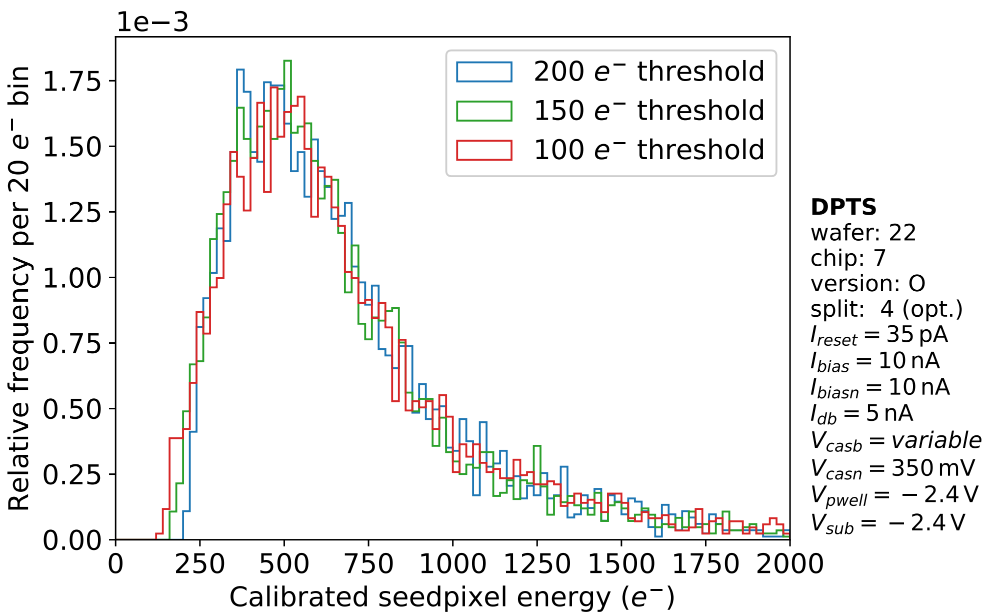

Figure 43: Seed pixel energy-straggling distribution

the TPSCo 65 nm technology (see Section 3.2.1).

5.5 Estimation of the Active Layer Thickness

Figure 46 shows the energy-straggling distribution measured at a threshold of around $100 \pm 10\,e^-$ for a non-irradiated DPTS at the PS July 2022 beam test (see Section 5.3.1). Since we are now interested in an estimation of the total energy deposited in the sensor, the cluster

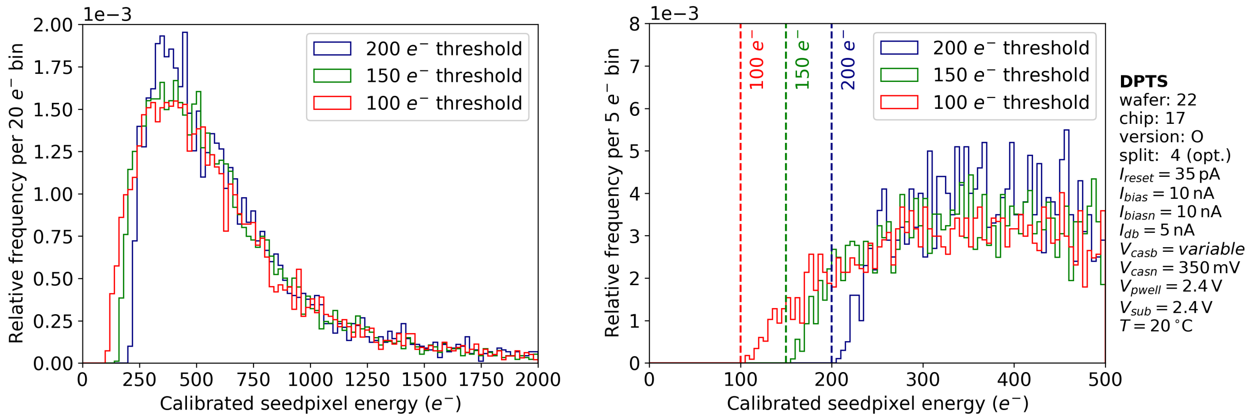

(a) Distribution up to 2000 e^-

(b) Lower end of the distribution up to 500 e^- with the corresponding threshold values highlighted

Figure 44: Seed pixel energy-straggling distributions at different threshold values for a 10^{15} 1MeV $\mathrm{n}_{eq}\,\mathrm{cm}^{-2}$ NIEL irradiated device. The operation parameters on the right side are valid for both plots.

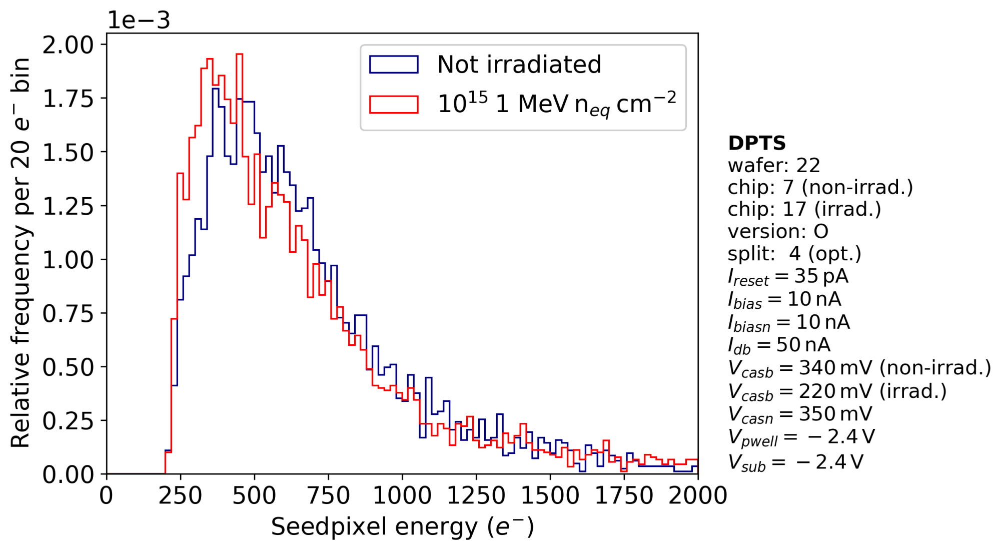

Figure 45: Comparison of in-beam seed pixel energy-straggling distributions between a non-irradiated and an irradiated device at 200 e^- threshold. The operational parameters shown in the legend are the same for both sensors unless stated otherwise.

energy is utilized, as defined in Section 4.4.3.

The distribution is fitted as described in Section 5.2.4. The fit results are also provided in Figure 46. Here, MPV refers to the most probable value of the energy loss, whereas the definition of η can be found in Equation 29. A denotes the height of the distribution and σ is the standard deviation of the Gaussian component of the fit. On the lower plot of Figure 46, the corresponding fit residuals are provided. They follow no clear trend and thus show that data and fit are compatible. This underlines that the data is well described by the fitting method explained in Section 5.2.4.

In order to validate the fit robustness in terms of the extracted MPV, a scan over the fit range as well as over the utilized number of bins was carried out. The result can be found in Appendix A.20.

From the resulting MPV, the active layer thickness Δ_{act} of the DPTS can now be estimated as explained in the following paragraphs.

The total energy E which is deposited in a silicon sensor with fully depleted Δ_{act} can be calculated using:

$$E = \left(\frac{dE}{dx}\right)_{Si} \Delta_{act} \tag{38}$$

Here, $\left(\frac{dE}{dx}\right)_{Si}$ is the most probable energy loss of a particle in a thin silicon detector. According to [35], its value for a layer thickness of 10 μm for charged particles ($\pm 1e^-$) can be estimated as 1.86 keV/μm. Given that the energy released by a traversing charged particle predominantly arises from ionization, it can be written as:

$$E = n_{e/h}\, W_{Si} \tag{39}$$

Here, $n_{e/h}$ represents the number of electron-hole pairs released, while $W_{Si} = 3.65\,\text{eV}$ [20] is the mean energy needed in order to create an electron-hole pair. Inserting 39 to Equation 38 gives the following expression for the active layer thickness:

$$\Delta_{act} = n_{e/h}\, W_{Si} \left(\frac{dE}{dx}\right)^{-1} \tag{40}$$

For $n_{e/h}$ we can assume the MPV of the cluster energy-straggling distribution. This gives us the following approximation of the active layer thickness:

$$\Delta_{act} \approx 10.5\,^{+1.2}_{-1.2}\,\mu m \tag{41}$$

Here, the errors are calculated following the derivation of Section 5.5.1 accounting for the underestimation of the MPV due to the applied threshold. The upper and lower error of the MPV were treated separately. However, it becomes apparent that the uncertainty is dominated by the fitting error, leading ultimately to no significant difference between the upper and the lower error. The result is further discussed in Section 6.

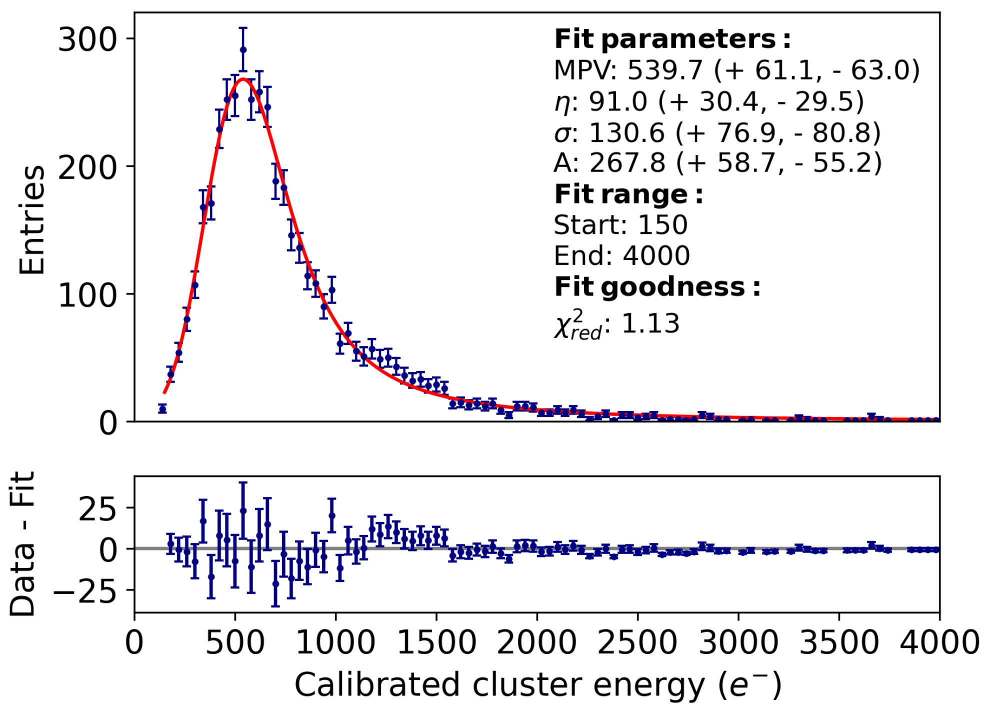

Figure 46: Calibrated cluster energy spectrum at a threshold of 100 e^- fitted using a Landau distribution convoluted with a Gaussian. Below, the respective fit residuals are provided.

5.5.1 Error Estimation of the MPV

In this work, the error on the determined most probable value of the energy loss is expected to arise predominantly from two sources. First, since the MPV is determined using the fitting method described in Section 5.2.4, the error will always be dependent on the asymmetric fitting error Γ_{fit}, separated in the upper and lower error $\Gamma_{fit,up}$ and $\Gamma_{fit,low}$, respectively. Second, there is always a systematic underestimation of the MPV due to the applied threshold on the sensor. As a result of undetected charges below the threshold, the detected cluster charge is most of the time smaller than the actual deposited energy. The corresponding error arising from this will be referred to as Γ_{thr}. To mitigate the effect, the lowest threshold with a reasonable FHR (cf. Section 3.3.3) was applied. Nevertheless, this effect is accounted for by estimating the systematic error Θ arising from the threshold.

For this, it is assumed that for every firing pixel, i.e. a pixel collecting a charge above the threshold, there is exactly one pixel collecting a significant, yet undetected, charge $\tilde{Q}$ below the threshold.

With a charge collection time of about 2 ns [40], here for a central hit in a pixel fabricated in the modified process with gap (see Section 3.2.1), and the diffusion constant of electrons in silicon ($3.6\,\mu\mathrm{m}^2/\mathrm{ns}$ [41]), it is roughly expected that most of the released charge will stay within an area of $7.2\,\mu\mathrm{m}^2$. This is less than half of the pixel area of the DPTS (see Section 3.2). Thus, for a track e.g. passing the centre of a pixel, no significant charge release is expected in a neighbouring pixel. Therefore, the aforementioned assumption is expected to overestimate the error arising from the threshold.

The additionally collected charge $\tilde{Q}$ from a non-firing pixel will be between 0 and the applied threshold Thr. The underlying distribution of $\tilde{Q}$ is approximated in the first order to be uniform with an expectation value of $\left\langle\tilde{Q}\right\rangle = (\frac{Thr}{2})$.

With the aforementioned assumption that, on average, for each firing pixel, one additional pixel will collect $\left(\frac{Thr}{2}\right)$ of charge, the systematic underestimation of the MPV can be estimated utilizing the mean cluster size $\left\langle CS\right\rangle$ of the respective data set:

$$\Theta = \left(\frac{Thr}{2}\right) \cdot \left\langle CS \right\rangle \tag{42}$$

The value of $\left\langle CS\right\rangle$ is determined from all usable events of the respective data set, i.e. events with all train-pairs matched (either directly or after a reevaluation of the position decoding) by the train-association algorithm described in Section 3.4.2.

Since the error of the MPV will be further used for the fitting of the MPV dependency on different incident beam angles in Section 5.6.5, the fitting error Γ_{fit} and the systematic underestimation Θ need to be added. For this, the systematic error has to be converted to a statistical-like error as following [42]:

$$\Gamma_{thr}^2 = \sigma^2 = \frac{\Theta}{\sqrt{12}} \tag{43}$$

where σ represents the standard error. The upper error on the MPV $\Gamma_{MPV,up}$ is now obtained by:

$$\Gamma_{MPV,up} = \sqrt{\Gamma_{fit,up}^2 + \frac{\Theta}{\sqrt{12}}} \tag{44}$$

The lower error $\Gamma_{MPV,low}$ is assumed to be given through the fitting error:

$$\Gamma_{MPV,low} = \Gamma_{fit,low} \tag{45}$$

5.6 Energy-straggling Analysis for Inclined Sensor Illumination

The following Sections provide the energy-straggling analysis of a DPTS inclined from 0° to 60° with respect to the beam. First, the corresponding in-beam test setup at DESY will be briefly described. The so-obtained energy-straggling distributions will then be fitted and the results will be provided and shortly discussed. Further, the theoretical shift of the MPV of the energy loss with increasing incident beam angle α will be derived. Finally, the derived function will be utilized to fit the $MPV(\alpha)$ dependency. From the fit parameters, an additional estimation of DPTS's active layer thickness will be obtained.

5.6.1 Testbeam Setup at the Deutsches Elektronen Synchrotron II

The Deutsches Elektronen Synchrotron II (DESY II) [43] is a particle accelerator located in Hamburg-Bahrenfeld. It hosts a test-beam facility providing electron or positron beams with user-selectable momenta ranging from 1 - 6 GeV/c. In December 2022, a test beam was carried out aiming for the study of the DPTS performance under inclined beam illumination. For this reason, the DPTS DUT was mounted on a motorized rotational stage of the type 'Zaber X-RSW Series' with an angle accuracy of $< 0.1\,°$ [44]. An image of the setup can be seen in Figure A.12 in the Appendix. For tracking purposes (relevant for efficiency as well as time and position resolution measurements), 3 ALPIDE sensors were mounted upstream, and additional 3 ones downstream of the DUT. The tracking information will not be used for the energy-straggling analysis described in this work.

5.6.2 Energy-straggling Distributions at Different Illumination Angles

Figure 47 shows energy-straggling distributions at different incident beam angles measured with the setup described in Section 5.6.1. From here, two major effects on the distributions of an increased incident angle become evident. First of all, the overall number of events in the respective data set decreases. This can be explained by the fact that higher inclination leads geometrically to larger cluster-sizes. As explained in Section 3.4.2, this results in more trains on the DPTS readout that have to be matched. In consequence, more matching errors occur, leading to a lower number of usable events. The train-matching performances for each sensor inclination angle α with respect to the beam are provided in Appendix A.4. Second, the distributions shift towards a higher energy loss. The accompanying increase of the most probable energy loss will be discussed theoretically in Section 5.6.4 while fitting results will be provided in Section 5.6.5.

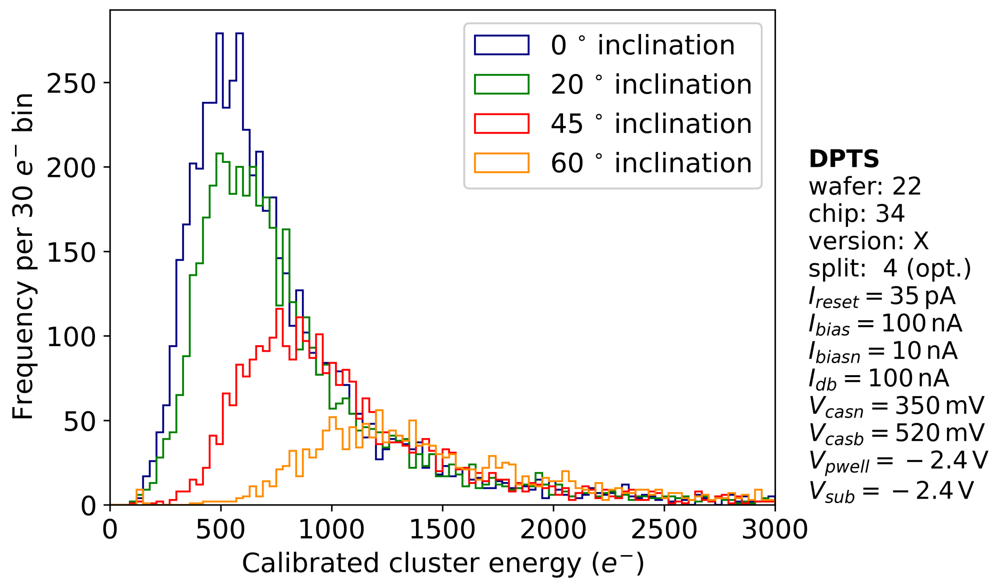

Figure 47: Energy-straggling distributions with variation of the incident beam angle α

5.6.3 Fitting of the Energy-straggling Distributions for different Illumination Angles

To quantify the influence of incident beam angles on the energy-straggling distributions, they are fitted with the same method as already described in Section 5.2.4. Additional to the distributions depicted in Figure 47, inclinations of $\alpha = 5°$ and $\alpha = 10°$ are included. For higher α, the binning was adjusted to maintain always a sufficient statistic of over 200 entries per bin around the MPV, ensuring a stable fitting. The fits together with their full results and residuals can be found in Appendix A.6. The extracted MPVs of the energy-straggling distributions are shown in Section 5.6.5. In the next Section, a derivation of the theoretically expected shift of the MPV is given.

5.6.4 Theoretical Expectation of the MPV shift

As already mentioned in Section 5.5, the energy deposited by an ionizing particle in the active layer Δ_{act} in a silicon sensor can be described by Equation 38. For sensors positioned in an angle α with respect to the incident beam, the distance δ that a beam particle traverses through the active layer of the sensor is no longer equal to Δ_{act}. Therefore, Equation 38 needs to be adapted as following:

$$E_{deposited} = \left(\frac{dE}{dx}\right)_{Si} \delta(\alpha) \tag{46}$$

From the geometry sketched in Figure 48, it follows:

$$\delta(\alpha) = \Delta_{act} \, \frac{1}{cos(\alpha)} \tag{47}$$

Inserting Equation 39 and 47 into Equation 46 leads to:

$$n_{e/h} = \left(\frac{dE}{dx}\right)_{Si} \Delta_{act} \, \frac{1}{W_{Si} \, cos(\alpha)} \tag{48}$$

Since the MPV of the energy-straggling distribution directly corresponds to $n_{e/h}$, Equation 48 gives the theoretical expectation for a measured $MPV(\alpha)$ dependence.

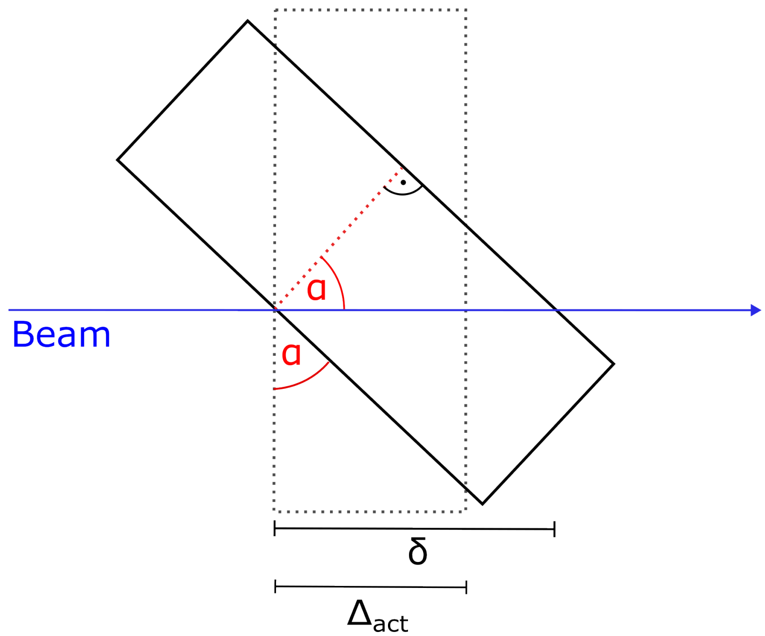

Figure 48: Sketch of the geometrical scaling of the particle path length through the active layer with a variation of the incident beam angle α. The dashed line refers to an active layer of an orthogonally placed device, while the solid line represents a sensor inclined with respect to the beam.

5.6.5 Active Layer Thickness Estimation from the MPV Shift

The theoretical expectation of the MPV shift with increasing α (Equation 48), which is derived in Section 5.6.4, can be utilized to fit the measured $MPV(\alpha)$ dependency.

The error on α, which is mechanically set by the motorized rotational stage (see Section 5.6.1) can be neglected for this analysis. Nevertheless, a constant angular offset arising from the mounting of the rotational stage as well as from a rotation of the whole telescope with respect to the beam is possible. To account for this, an angular offset α_0 was introduced to Equation 48 and is treated as a free fit parameter. The fit, together with the respective results, is shown in Figure 49. The theoretically described fit function is observed to agree with the data within the errors. Since the active layer thickness Δ_{act} is treated as a free fit parameter, an additional estimation to the one performed in Section 5.5 can be obtained:

$$\Delta_{act} = 10.1 \pm 0.6\,\mu m \tag{49}$$

From the fit, the angular offset of the telescope (cf. Section 5.6.1) with respect to the beam is estimated to:

$$\alpha_0 = 3.4 \pm 3.1^\circ \tag{50}$$

The value of α_0 lies in the expected accuracy range from the mechanical installation and is compatible with zero, considering the respective errors.

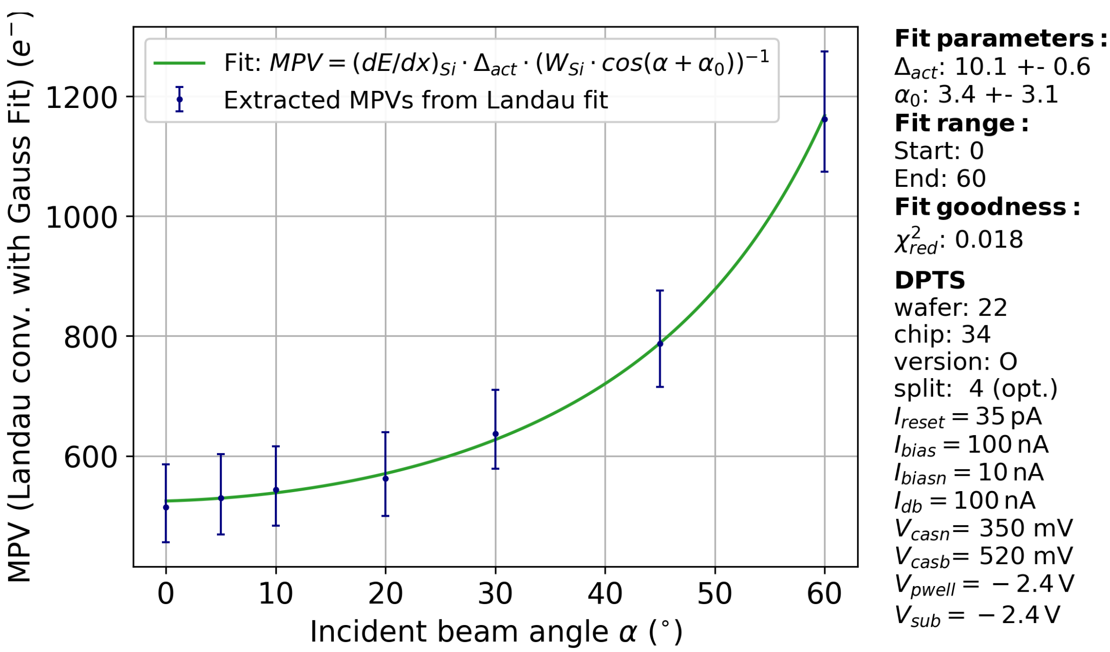

Figure 49: Fitted dependence of the MPV on the incident beam angle α.

By converting the incident beam angle α using Equation 47, the MPV is shown in Figure 50 in dependence of the relative active layer thickness $\delta(\alpha)$. For Δ_{act}, the in Equation 49 determined value is utilized. The error of the active layer thickness is derived from the corresponding error on Δ_{act} using Gaussian error propagation. As expected, the MPV of the detected energy loss rises with a longer path through the active layer. The dependency is fitted here, as a first-order approximation of the underlying function, with a linear dependency. The fit and the corresponding fit results are provided in Figure 50.

For the shown range of the active layer thickness, an energy loss of $63 \pm 12\,\frac{e^-}{\mu m}$ corresponding to $230 \pm 40\,\frac{eV}{\mu m}$ is estimated. This value agrees with the in [35] reported values for silicon thicknesses of $10\,\mu$m and $20\,\mu$m according to the Bichsel model (see Section 5.2.3).

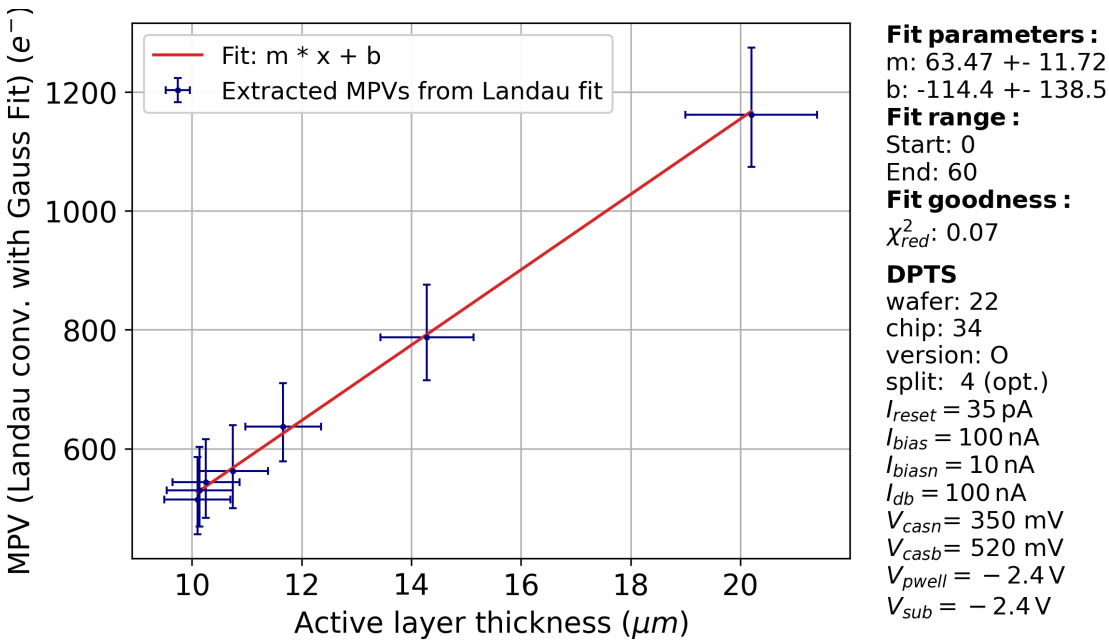

Figure 50: Fitted dependence of the MPV on the active layer thickness δ.

6 Summary & Outlook

The addressed topics and results of this work will be summarized and discussed in the following paragraphs.

ALICE and ITS3 During the next long shutdown period of the LHC (LS3, 2026 - 2028), the Inner Tracking System of the ALICE experiment will be upgraded to the ITS3 (Section 2.4). With a progressive R&D approach, featuring ultra-thin, wafer-scale and truly cylindrical MAPS, fabricated in 65 nm TPSCo technology, the material budget is expected to be reduced from $0.36\,\%\,X_0$ to $0.05\,\%\,X_0$ per layer (Section 2.4.1). Furthermore, the distance of the first tracking layer will be brought about 5 mm closer towards the interaction point. Consequently, the tracking efficiency and pointing resolution are expected to improve significantly, especially at low transverse momenta (Section 2.4.3). As a result, several benefits for the probing of QGP are foreseen, particularly for the study of heavy-flavour production and low-mass dileptons. (Section 2.4.4).

DPTS The novel 65 nm TPSCo fabrication process is foreseen to be employed for the ITS upgrade, due to larger commercially available wafer sizes and higher expected radiation tolerance. Additionally, it provides the possibility to achieve a reduced power consumption due to a smaller feature size with respect to the previously utilized 180 nm process (cf. Section 2.3.2). The novel technology needs to be well characterized and understood in terms of its charge collection performance when exposed to radiation sources and to charged-particle beams. This requires an extensive R&D program, including the study of the technology's robustness in terms of radiation. Additionally, the influence of the operational parameters and environmental conditions on its performance has to be probed, for example in terms of detection efficiency and spatial resolution.

Among the first prototypes fabricated in the novel process is the DPTS, aiming at investigating the technology for a 32×32 pixel matrix with a digital readout (Section 3.2). In this work, the functionality and technology of the device are explained. Further, the basic analysis methods, e.g. to determine the sensor's threshold, fake-hit rate and hit positions, are described (Section 3.3).

For the sensor, a simplified design for the readout was chosen, where hit and ToT information of all firing pixels are digitally time-encoded and multiplexed to a single output line (see Section 3.2.3). Despite providing more direct access to the sensor's output and lowering the power consumption by driving solely one output line, the readout leads to challenges in the characterization and data analysis. Hit-position decoding calibrations must be performed right before or after each measurement due to the influence of the sensor's frontend parameters and environmental conditions on the decoding. Despite this, errors in the position decoding can occur, leading to hits being associated with a wrong pixel position (see Section

3.3.1). These errors do not affect the total detection efficiency of the sensor, since the hits are still being registered. However, these errors limit the device's position resolution. Despite the resulting characterization challenges, the simplified readout principle proved its functionality.

Train-matching algorithm Due to the special asynchronous readout architecture of the DPTS (Section 3.2.3), the extraction of ToT information for multi-pixel clusters is not trivial. It requires the matching of pulse train pairs arising on the single output line. In the context of this work, a dedicated algorithm for the required pulse train-matching was developed, including the detection and correction of possible position decoding errors (Section 3.4.2). It is based on the key assumption that an event, containing n_T pulse trains, consists of solely rising edge trains in the earliest $n_T/2$ trains, and solely falling edge trains in the last $n_T/2$ trains. In this way, only events with even n_T are matched.

For $^{55}_{26}$Fe and in-beam data recorded at CERN's Proton Synchrotron (Sections 4.4.3 and 5.3.4), the total fraction of well-extracted ToTs is increased from about 80 to 90 % for $^{55}_{26}$Fe data and from about 60 to 70 % for in-beam data. More importantly, the relative fraction of well-extracted ToTs per cluster size ≥ 2 was observed to be increased by around 20 - 30 %. This way, the algorithm allows for extracting more representative seedpixel distributions for $^{55}_{26}$Fe and in-beam data. Here, the seedpixel is defined as the pixel with the highest ToT in a cluster.

A possible optimization of the developed algorithm could include the processing of events with odd n_T, achieved by filtering out trains arising from noise. However, due to the low FHR reached by the DPTS [21], just a marginal improvement is expected. In addition, alternative approaches to the here-utilized categorization of events could be studied. However, this is expected to increase the algorithm's complexity.

The implementation of the train-matching algorithm, developed in the context of this work, into the beam test analysis chain of the DPTS is foreseen. By the extraction of the ToT of every pixel in a cluster, charge-weighting can be applied to obtain an improved position resolution with the device.

$^{55}_{26}$Fe response The response of the DPTS to radioactive sources is studied within this work utilizing an $^{55}_{26}$Fe source. Its disintegration reaction and the underlying mechanisms leading to the characteristic X-ray emissions are explained. Further, the mechanisms leading to the silicon-escape as well as the silicon-fluorescence peaks are described, and their expected energies are derived (Section 4.2).

The measured ToT spectrum in response to $^{55}_{26}$Fe is corrected for inter-pixel ToT variations. For this, the dependence of the ToT on the pulsing voltage was measured (see Section 3.2.2) and fitted for each pixel individually utilizing an empirically determined function (see Section

3.3.4). This way, the ToT is converted to the corresponding injection voltage, eliminating inter-pixel ToT variations. The ToT-calibration showed to increase the spectrum's resolution significantly.

In the single-pixel ToT spectrum, four distinct peaks are observed: $Mn\text{-}K_{\alpha}$, $Mn\text{-}K_{\beta}$, Si_{esc} and Si_{fl}. The peaks are fitted using Gaussian distributions added to 0th and 1st-order polynomial background approximations. Here, the fitting could be optimized by conducting a dedicated background analysis to get a better motivated fit function. However, the scope of the fitting was here solely the extraction of the peak positions for the following energy calibration of the sensor. Correlating the expected well-known energies with the peak positions, a ToT-to-energy calibration was established for the specifically chosen sensor and operational conditions. At a temperature of $20\,°C$, a back-bias voltage of $-2.4\,V$ and a threshold of $100 \pm 10\,e^{-}$ (notation: mean $\pm$ RMS), the devices energy calibration factor was found to be around $1.16 \pm 0.03\,\frac{e^{-}}{mV}$. Here, just the fitting error is accounted for.

Since the ToT response is dependent on the sensor as well as on the device's operating point and temperature, a separate energy calibration needs to be carried out for different operational conditions. To accelerate the procedure, an automized fit of the $Mn\text{-}K_{\alpha}$ peak with a data-driven pre-fit parameter estimation was implemented (see Section 4.4.2). The automized method resulted in an energy calibration factor of $1.15 \pm 0.03\,\frac{e^{-}}{mV}$ for the above-mentioned conditions. With a discrepancy below one standard deviation from the first method, the automized method is validated.

The analyzed $^{55}_{26}$Fe spectrum was compared to the equivalent spectrum from a sensor at a NIEL-irradiation level of 10^{15} 1MeV $\mathrm{n}_{eq}\,\mathrm{cm}^{-2}$ (see Section 4.4.4). From the comparison, a decrease in the collected charge as well as in the energy resolution becomes evident. However, the $Mn\text{-}K_{\alpha}$ is still resolvable at this level and thus the aforementioned energy calibration can still be performed. Hereby, the excellent radiation hardness of the novel 65 nm TPSCo technology operating at comparably high temperatures of $20\,°C$ is stressed.

For an instructive insight on the clustered $^{55}_{26}$Fe data recorded with the DPTS, the contributions of different cluster-sizes on the seedpixel spectrum are investigated (see Section 4.4.5). It was shown that larger cluster-sizes lead to smaller seedpixel charges, as expected from charge-sharing. Furthermore, an estimation of the minimum expected seedpixel charge was carried out, identifying charge contributions originating from the substrate. Despite the simplicity of the applied model, a good agreement with the observed edge in the two-pixel cluster spectrum became evident. Further verification of the model could be performed utilizing a high-statistic data set, selecting events around the estimated minimum seedpixel charge for a given cluster-size ≥ 2. The distribution of collected charges per neighbour-pixel would then verify the model by showing a distinct peak at the provided threshold.

Energy-straggling Within this thesis, the theory of energy loss of charged particles in matter is summarized. Concerning the mean energy loss, the Bethe-Bloch model for heavy particles, as well as the Berger-Seltzer model for light particles, are briefly addressed. For the description of energy-straggling, three models applicable for different thicknesses of the absorber material, are discussed: the Gaussian model for thick absorbers, the Landau model for thin absorbers, and the Bichsel model for very thin absorbers.

Although the Bichsel model has shown in [35] to reproduce observed energy-straggling distributions more accurately for very thin detection layers of $\mathcal{O}(10\,\mu\text{m})$, it provides no closed analytical form and has to be approximated numerically. By the time this analysis was conducted, no software package performing the required numerical approximation to fit the measured distributions was publicly available. Nevertheless, tight constraints in the material budget of future experiments lead to the requirement of thinner and thinner sensors. The development of a dedicated and publicly available tool to numerically approximate and fit energy-straggling distributions, utilizing the Bichsel model, would be advisable. However, its implementation was not in the scope of this work, since here solely a good empirical description of the measured data is desired. This is already provided by the Landau model convoluted with a Gaussian distribution.

Within the work of this thesis, an analysis chain for extracting energy-straggling distributions from in-beam data was developed (Section 5.3). The raw ToT distributions were corrected for inter-pixel variations. The utilized calibration method was validated by reproducing the lower end of the respective ToT distributions at the applied threshold value. Moreover, the energy-straggling distributions were energy-calibrated using a corresponding $^{55}_{26}$Fe data set. The resulting seedpixel energy-straggling distributions showed a good agreement for values well above the respective threshold, underlining the linearity of the DPTS's frontend. Additionally, the linearity was shown to hold for large charge deposits in the case of a 10^{15} $1\text{MeV}\,\text{n}_{eq}\,\text{cm}^{-2}$ NIEL irradiated sensor.

Section 5.5 shows an energy-straggling distribution recorded during the in-beam test at CERN's Proton Synchrotron (see Section 5.3.1) at a temperature $20\,°C$, a back-bias voltage of -2.4 V (full depletion) and a threshold of $100 \pm 10\,e^-$. The distribution was fitted according to the method described in Section 5.2.4. The active layer's thickness was determined from the distribution's MPV to $10.5^{+1.2}_{-1.2}\,\mu$m. The uncertainty was estimated accounting for the asymmetrical fitting error of the MPV and the systematically smaller collected charge due to the applied threshold (Section 5.5.1). For the latter contribution, it was assumed that for every firing pixel there is one additional pixel collecting undetected charge $\tilde{Q}$ below the threshold Thr. This likely overestimates the number of pixels collecting additional charge, but leads to a valid upper limit estimation of the error. Additionally, the expectation value of $\tilde{Q}$ was assumed to be $\langle\tilde{Q}\rangle = (\frac{Thr}{2})$ in a first-order approximation. A possible optimization of the estimation of $\langle\tilde{Q}\rangle$ could be obtained by a dedicated simulation of DPTS's charge collection. However, the fitting error of the MPV dominates here the systematic uncertainty arising from the applied threshold. Thus, no major influence on the determined uncertainties is expected from an optimized estimation of $\langle \tilde{Q} \rangle$.

The active layer at full depletion is not to be confused with the epitaxial layer thickness (Section 3.2.1). It is expected that also parts of the substrate contribute to the charge collection and thus to the active layer. This contribution can be estimated by performing a detailed simulation of the charge collection, which was not in the scope of this work.

The energy-straggling distributions are also studied for inclined sensor illumination at the DESY beam test facility (see Section 5.6.1). The obtained and corrected distributions were fitted following the same procedure as the aforementioned fit. The binning was adjusted here such that sufficient statistics of at least 200 entries around the MPV are ensured. A data set with higher statistics could help here to use the exact same fit conditions for all illumination angles. Nevertheless, the applied fits describe the data well as visible from Appendix A.6. The obtained dependency of the MPV on the sensor's inclination angle was then fitted using the in Section 5.6.4 derived relation. A linear dependency of the deposited energy on the active layer thickness is assumed, which is validated for the thickness range from $10\,\mu$m - $20\,\mu$m through Figure 50. The fit showed a good agreement with the measured data. As a result, the active layer thickness was estimated to $10.1 \pm 0.6\,\mu$m with an assessed inclination of the beam telescope of $3.4 \pm 3.1\,^\circ$ with respect to the beam. Both estimations of the active layer thickness agree within one standard deviation.

The estimations of the active layer thickness could be improved by obtaining data sets with higher statistics. This way, the dominating fitting errors of the MPV could be reduced. Further, instead of using the telescope inclination as a free fit parameter, it could be estimated by analysing tracking information. The information could also be used to cut solely on events with a track passing one pixel centrally. By this, the effect of charge-sharing can be mitigated and the systematic uncertainty arising from the applied threshold could be reduced. However, the investigation of the MPV dependency on the beam inclination is more of academic interest and the further improvement of the active layer thickness estimation is not of high priority for DPTS's R&D program.

Finally, the MPV was plotted in dependence of the active layer thickness, using the conversion in Equation 47. Here, the energy loss per unit absorber length is estimated in a first-order approximation to $230 \pm 40\,\frac{eV}{\mu m}$ in the range of $10\,\mu$m to $20\,\mu$m. The estimation agrees with the values reported in [35].

Conclusion The DPTS has shown excellent performance regarding charge collection and radiation hardness. Exposed to radiation sources and during beam test studies, the novel TPSCo 65 nm process was validated for the application within ITS3 [21].

Within this work, the charge collection properties in terms of $^{55}_{26}$Fe response and in-beam performance were studied. Hereby, the linearity of the DPTS's in-pixel frontend was validated for energies well above the applied threshold. Moreover, the robustness of the DPTS exposed to NIEL-irradiation up to 10^{15} $1\,\mathrm{MeV\,n}_{eq}\,\mathrm{cm}^{-2}$ has been underlined for the response to $^{55}_{26}$Fe and in-beam data. Furthermore, the train matching algorithm, developed in the context of this work, is expected to increase the spatial resolution of the DPTS reported in [21] by enabling charge-weighting.

The excellent results of the DPTS pave the way for the next milestone towards the ITS3: the creation of large active areas up to $270{\times}90\,\mathrm{mm}^2$ in the 65 nm technology using stitching [45] (Section 2.4.2).

A Appendix

A.1 $^{55}_{26}$Fe Setup

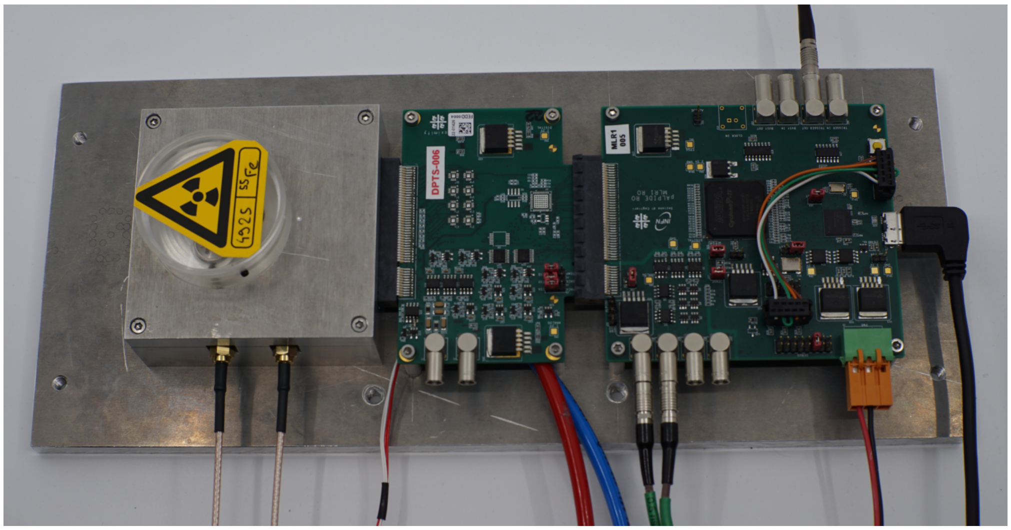

Figure A.1: DPTS setup for measurements with attached $^{55}_{26}$Fe source.

A.2 DUT cooling in at PS

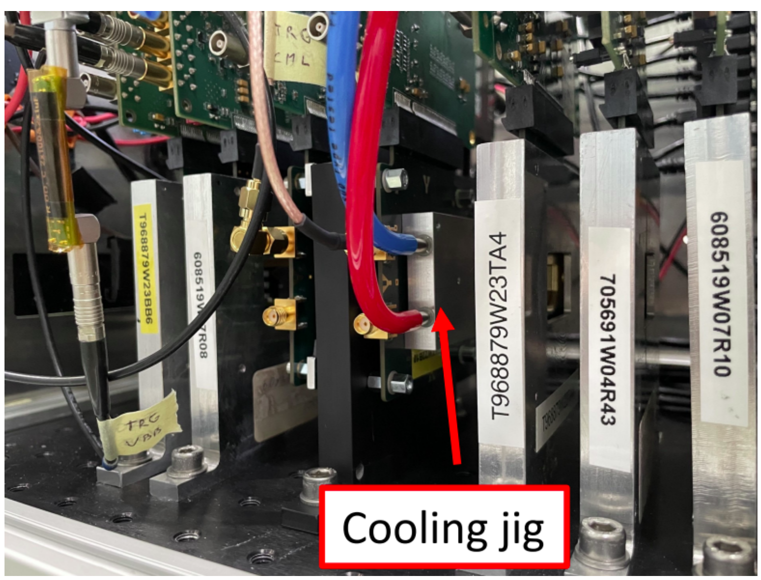

Figure A.2: Water cooling jig mounted on the backside of the DUT.

A.3 Train matching performance for a NIEL-irradiated DPTS

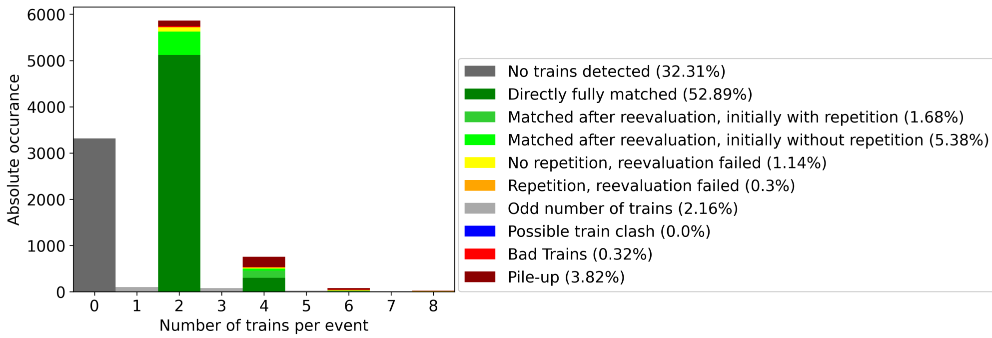

Figure A.3: Exemplary train multiplicity distribution together with the absolute train matching performance on in-beam data recorded with an 10^{15} $1\mathrm{MeV}\,\mathrm{n}_{eq}\,\mathrm{cm}^{-2}$ device at $200\,e^{-}$ threshold. Just bins with sufficient statistics over 10 entries are plotted

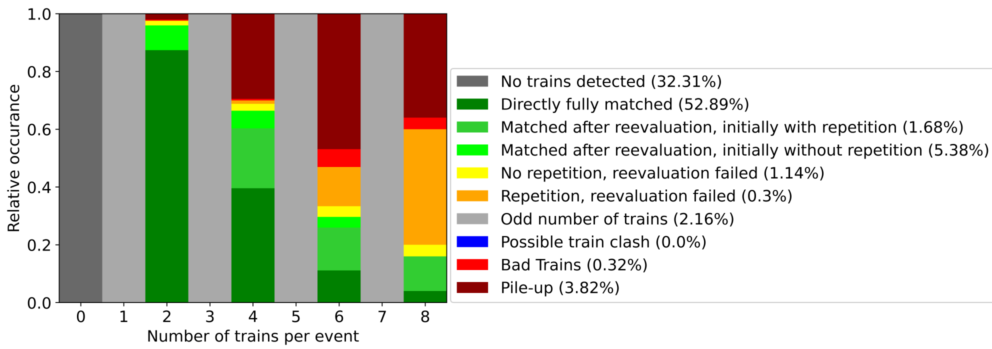

Figure A.4: Exemplary relative train matching performance on in-beam data recorded with an 10^{15} $1\mathrm{MeV}\,\mathrm{n}_{eq}\,\mathrm{cm}^{-2}$ device for $200\,e^{-}$ threshold. Just bins with sufficient statistics over 10 entries are plotted.

A.4 Train Matching for Inclined Illumination

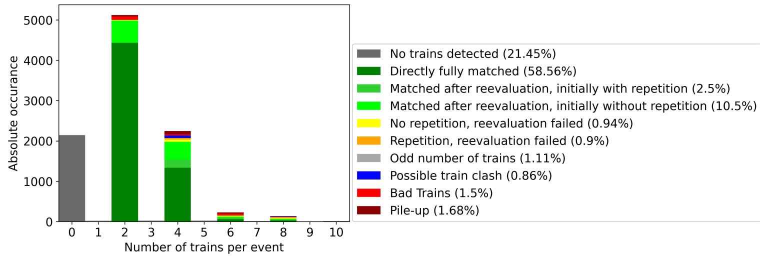

(a) Absolute performance

(b) Relative performance

Figure A.5: Train matching performance for inclined illumination with $\alpha = 0°$

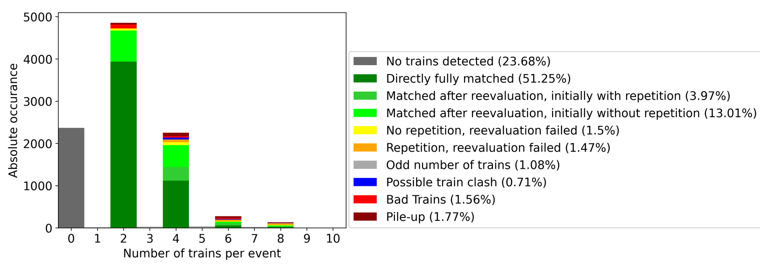

(a) Absolute performance

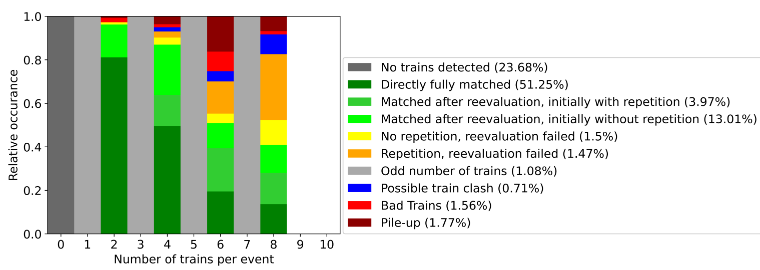

(b) Relative performance

Figure A.6: Train matching performance for inclined illumination with $\alpha = 5°$

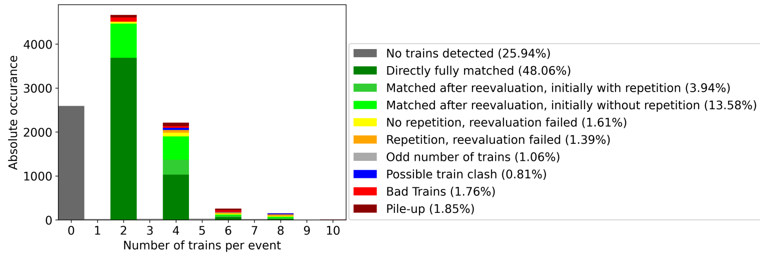

(a) Absolute performance

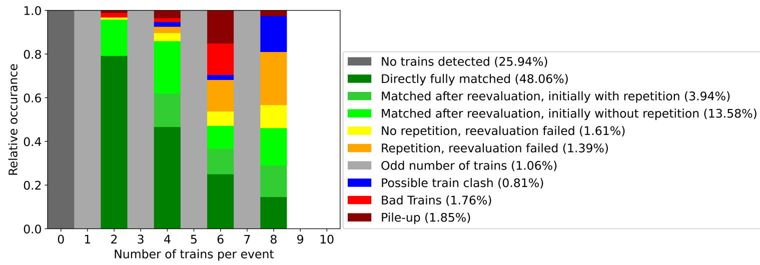

(b) Relative performance

Figure A.7: Train matching performance for inclined illumination with $\alpha = 10°$

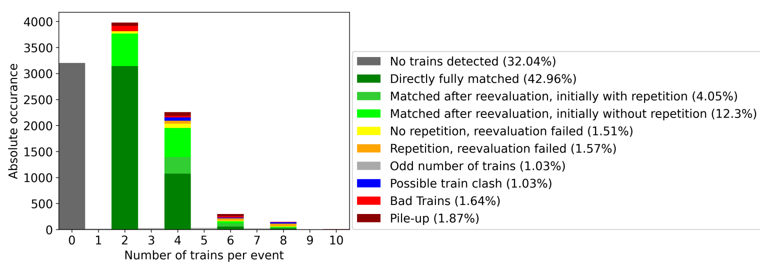

(a) Absolute performance

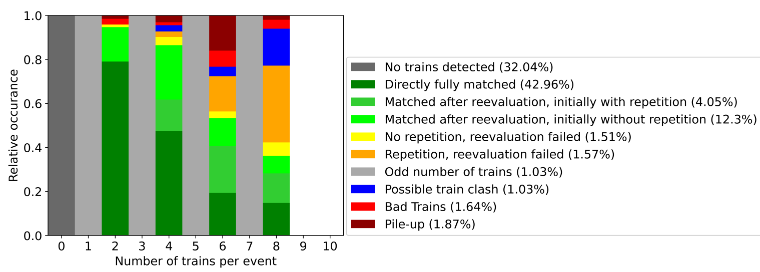

(b) Relative performance

Figure A.8: Train matching performance for inclined illumination with $\alpha = 20°$

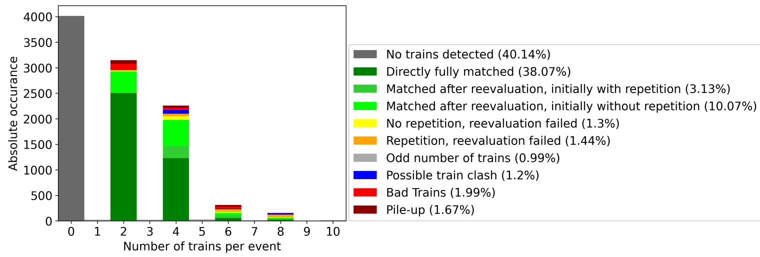

(a) Absolute performance

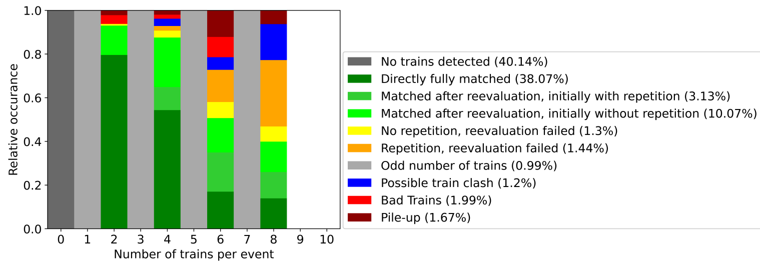

(b) Relative performance

Figure A.9: Train matching performance for inclined illumination with $\alpha = 30°$

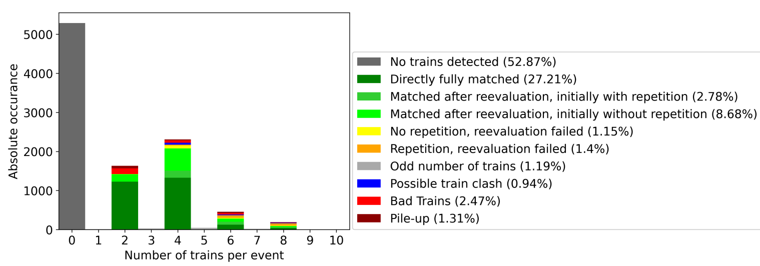

(a) Absolute performance

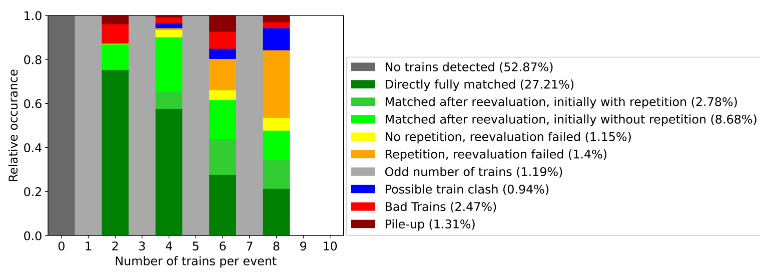

(b) Relative performance

Figure A.10: Train matching performance for inclined illumination with $\alpha = 45°$

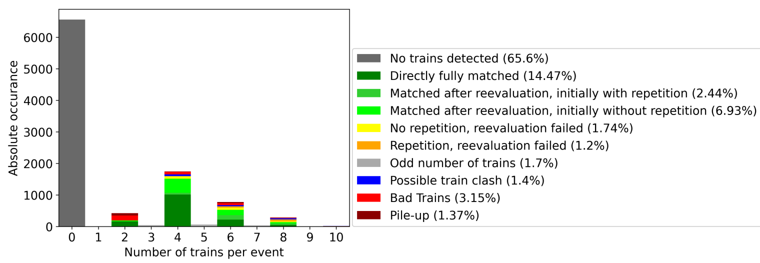

(a) Absolute performance

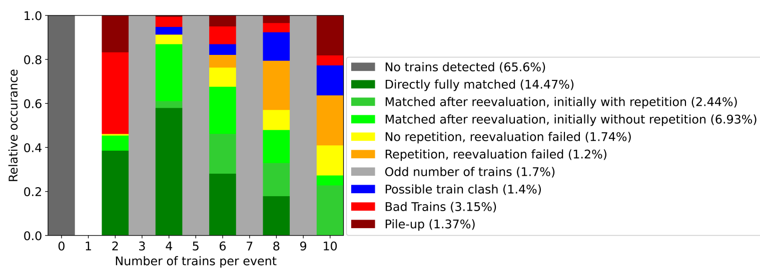

(b) Relative performance

Figure A.11: Train matching performance for inclined illumination with $\alpha = 60°$

A.5 In-beam test setup for inclined illumination

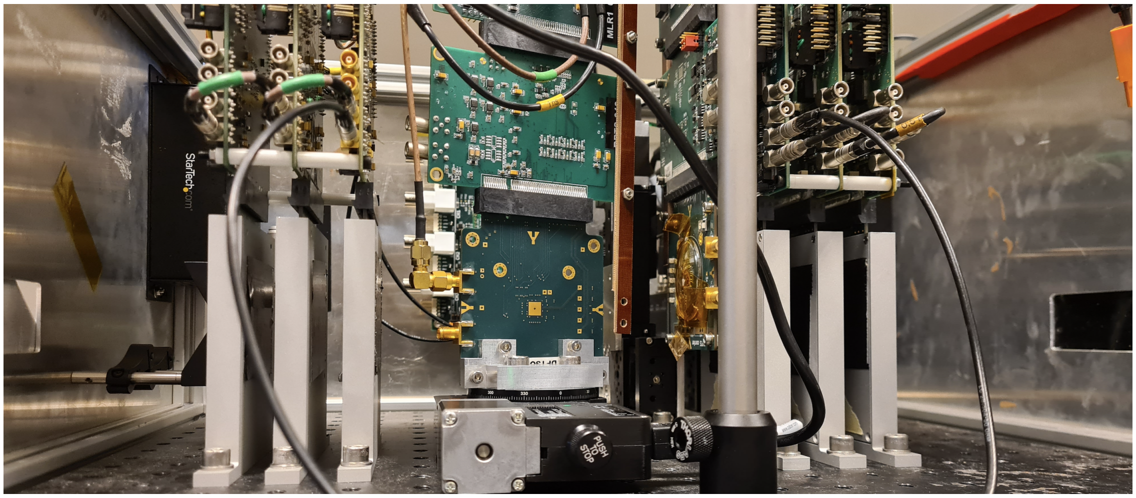

Figure A.12: In-beam test setup for inclined illumination. The DPTS DUT is mounted on a rotational motorized stage between the ALPIDE reference planes.

A.6 Energy-straggling Distributions for Inclined Illumination

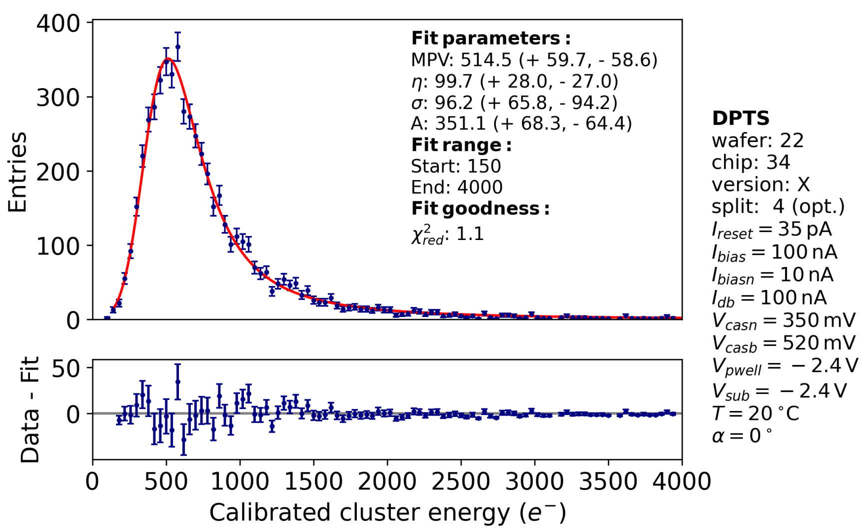

Figure A.13: Fitted calibrated cluster energy spectrum at an incident beam angle of $\alpha = 0°$ together with the respective fit residuals.

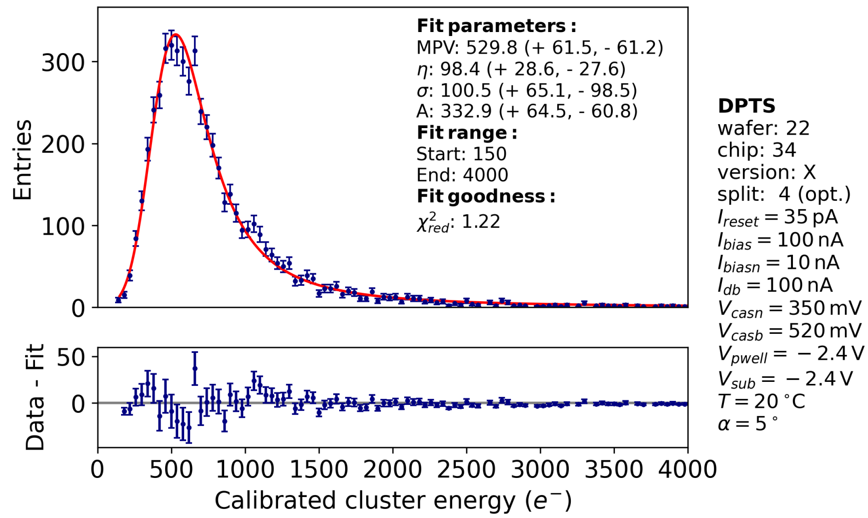

Figure A.14: Fitted calibrated cluster energy spectrum at an incident beam angle of $\alpha = 5°$ together with the respective fit residuals.

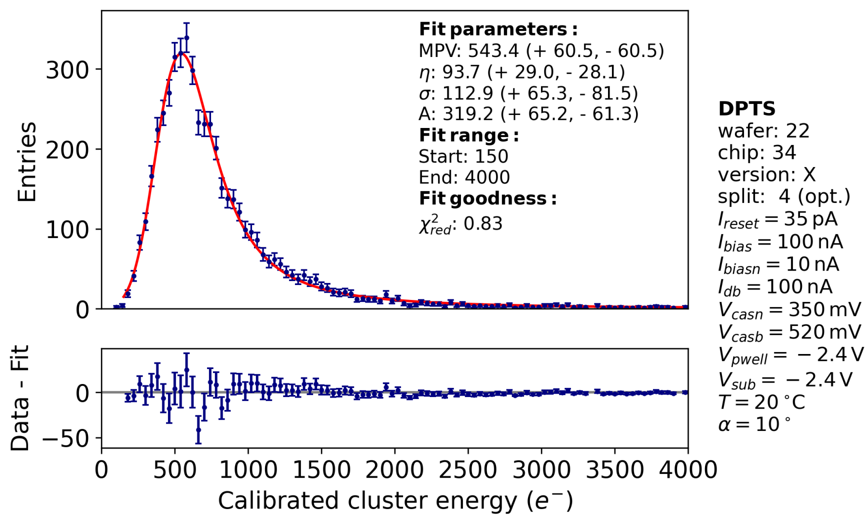

Figure A.15: Fitted calibrated cluster energy spectrum at an incident beam angle of $\alpha = 10°$ together with the respective fit residuals.

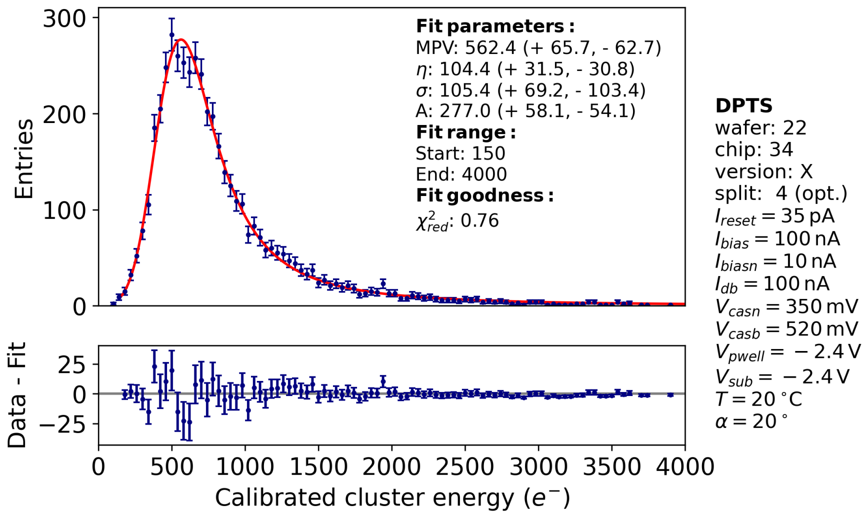

Figure A.16: Fitted calibrated cluster energy spectrum at an incident beam angle of $\alpha = 20°$ together with the respective fit residuals.

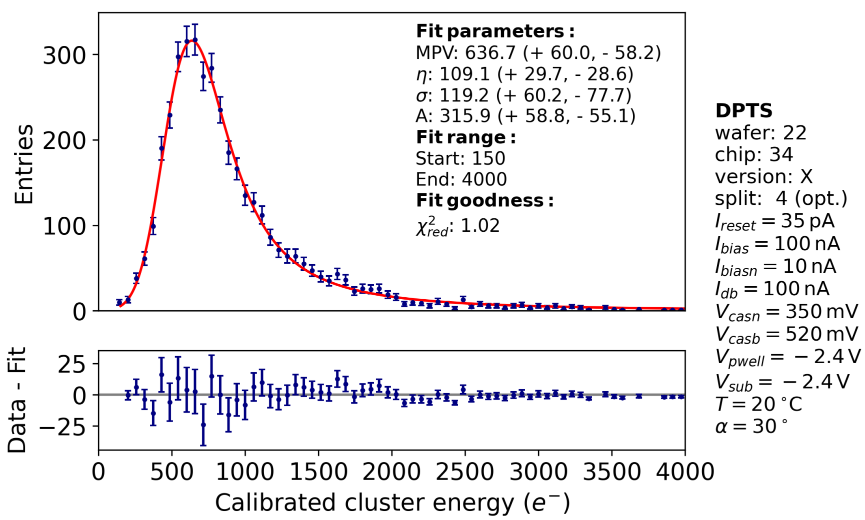

Figure A.17: Fitted calibrated cluster energy spectrum at an incident beam angle of $\alpha = 30°$ together with the respective fit residuals.

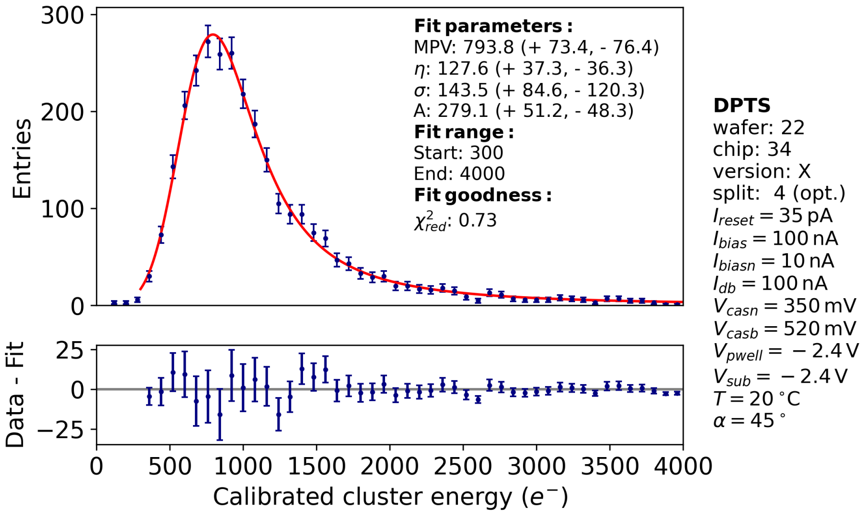

Figure A.18: Fitted calibrated cluster energy spectrum at an incident beam angle of $\alpha = 45°$ together with the respective fit residuals.

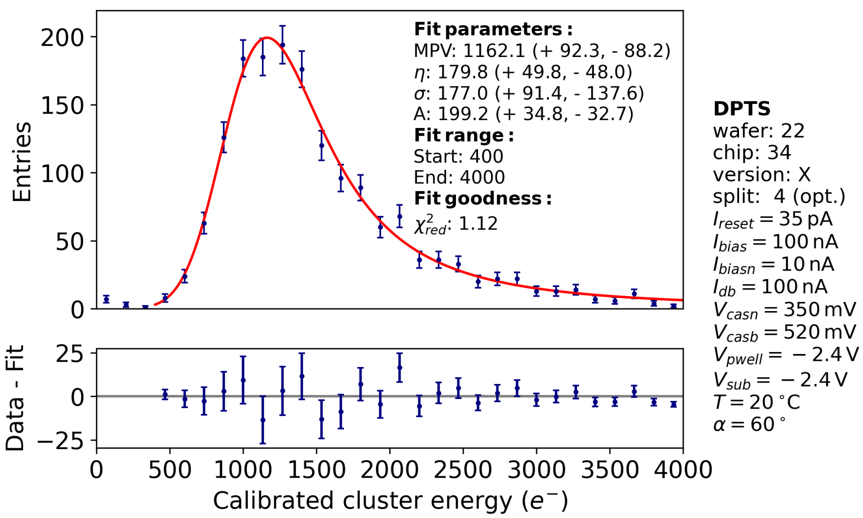

Figure A.19: Fitted calibrated cluster energy spectrum at an incident beam angle of $\alpha = 60°$ together with the respective fit residuals.

A.7 Fit Robustness

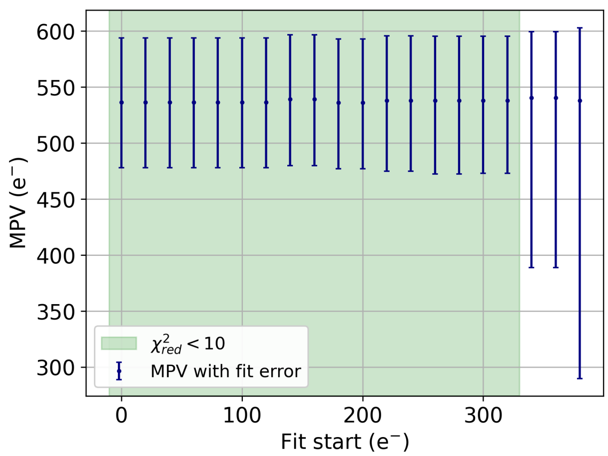

(a) Extracted MPV from the fit with 100 bins varying the start value of the fit.

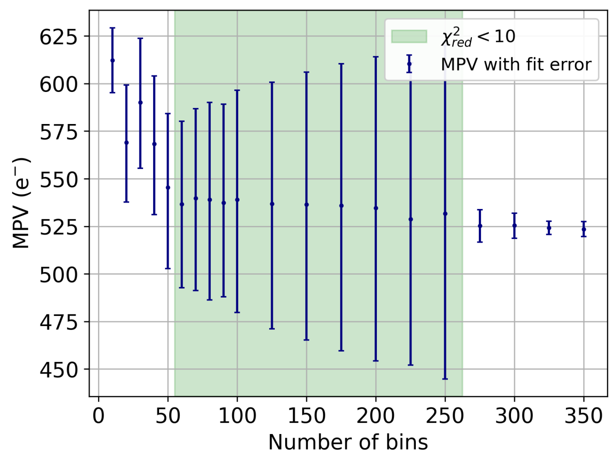

(b) Extracted MPV from the fit with a fit start value of 150 e^- varying the number of bins in the histogram.

Figure A.20: Exemplary checks on the fit robustness in terms of the MPV. Here, the recorded energy-straggling distribution shown in Figure 46 is fitted with the method described in Section 5.2.4. The extracted MPV values in dependence of the fit start as well as the number of bins are compatible within the errors in the $\chi^2_{red} < 10$ region. Also in dependence of the fit end value (not depicted), the extracted MPV values were observed to be compatible.

References

[1] J. W. Harris and B. Müller. THE SEARCH FOR THE QUARK-GLUON PLASMA. *Annual Review of Nuclear and Particle Science*, 46(1):71–107, dec 1996.

[2] ALICE Collaboration. The ALICE experiment at the CERN LHC. *Journal of Instrumentation*, 3(08):S08002, aug 2008.

[3] M. Thomson. *Modern Particle Physics*. Cambridge University Press, 2013.

[4] F. Mandl and G. Shaw. *QUANTUM FIELD THEORY*. 1985.

[5] S. Sarkar et al. *The Physics of the Quark-Gluon Plasma*. Springer Berlin, Heidelberg, 210.

[6] G. Baym et al. From hadrons to quarks in neutron stars: a review. *Reports on Progress in Physics*, 81(5):056902, mar 2018.

[7] M. Šuljić. *Study of Monolithic Active Pixel Sensors for the Upgrade of the ALICE Inner Tracking System*. PhD thesis, Universit'a degli Studi di Trieste, 2018.

[8] A. Villani. Complete characterization of the first digital monolithic pixel structures in 65 nm CMOS technology. Master's thesis, Universit'a degli Studi di Trieste, 2022.

[9] A. Tauro. ALICE Schematics. General Photo, 2017.

[10] ALICE Collaboration. Technical Design Report for the upgrade of the ALICE Inner Tracking System. *Journal of Physics G: Nuclear and Particle Physics*, (8):087002, jul.

[11] ALICE Collaboration. ALICE upgrades during the LHC Long Shutdown 2, 2023.

[12] M. Mager. ALPIDE, the Monolithic Active Pixel Sensor for the ALICE ITS upgrade. *Nuclear Instruments and Methods in Physics Research Section A: Accelerators, Spectrometers, Detectors and Associated Equipment*, 824:434–438, 2016. Frontier Detectors for Frontier Physics: Proceedings of the 13th Pisa Meeting on Advanced Detectors.

[13] Tower Semiconductor. CMOS image sensors. `https://towersemi.com/technology/cmos_image_sensor/`, accessed May 10, 2023.

[14] V. Raskina and F. Křížek. Characterization of Highly Irradiated ALPIDE Silicon Sensors. *Universe*, 5(4):91, Apr 2019.

[15] G. Aglieri Rinella. The ALPIDE pixel sensor chip for the upgrade of the ALICE Inner Tracking System. *Nuclear Instruments and Methods in Physics Research Section A: Accelerators, Spectrometers, Detectors and Associated Equipment*, 845:583–587, 2017. Proceedings of the Vienna Conference on Instrumentation 2016.

[16] M. Šuljić. ALPIDE: the Monolithic Active Pixel Sensor for the ALICE ITS upgrade. *Journal of Instrumentation*, 11(11):C11025, nov 2016.

[17] M. Buckland. Development of the ITS3: A bent-silicon vertex detector for ALICE in the LHC Run 4. *Nuclear Instruments and Methods in Physics Research Section A: Accelerators, Spectrometers, Detectors and Associated Equipment*, 1039:166875, 2022.

[18] L. Musa. Letter of Intent for an ALICE ITS Upgrade in LS3. Technical report, CERN, Geneva, 2019.

[19] G. Aglieri Rinella et al. First demonstration of in-beam performance of bent monolithic active pixel sensors. *Nuclear Instruments and Methods in Physics Research Section A: Accelerators, Spectrometers, Detectors and Associated Equipment*, 1028:166280, 2022.

[20] H. Kolanoski and N. Wermes. *Particle Detectors: Fundamentals and Applications*. Oxford University Press, jun 2020.

[21] G. Aglieri Rinella et al. Digital Pixel Test Structures implemented in a 65 nm CMOS process. Technical report, 2022.

[22] Pico Technology. PicoScope® 6000ESeries. `https://www.picotech.com/download/datasheets/picoscope-6000e-series-data-sheet.pdf`, accessed March 17, 2023.

[23] R. L. Workman et al. *Review of Particle Physics*. Particle Data Group, 2022.

[24] M. M. Be et al. *Table of radionuclides (Vol3 - = 3 to 244)*. Table de radionucleides. Editions Bureau International des Poids et Mesures, France, 2006.

[25] M. Berger et al. XCOM: Photon Cross Sections Database. nov 2010.

[26] M. Berger et al. Stopping-Power & Range Tables for Electrons, Protons, and Helium Ions. oct 1998.

[27] M. Berger et al. Binding energy table. `https://xdb.lbl.gov/Section1/Table_1-1.pdf`, accessed April 17, 2023.

[28] A. Kramida et al. Atomic Spectra Database. mar 1995.

[29] R. Deslattes et al. X-ray Transition Energies Database. sep 2005.

[30] R. L. Workman et al. Review of Particle Physics. *PTEP*, 2022:083C01, 2022.

[31] S. M. Seltzer and M. J. Berger. Evaluation of the collision stopping power of elements and compounds for electrons and positrons. *The International Journal of Applied Radiation and Isotopes*, 33(11):1189–1218, 1982.

[32] W. Leo. *Techniques for Nuclear and Particle Physics Experiments*. Springer Berlin, Heidelberg, ju 1994.

[33] L. Landau. On the energy loss of fast particles by ionization. *J. Phys.*, 8(4):201–205, 1944.

[34] K.S. Kölbig and B. Schorr. A program package for the landau distribution. *Computer Physics Communications*, 31(1):97–111, 1984.

[35] H. Bichsel. Straggling in thin silicon detectors. *Rev. Mod. Phys.*, 60:663–699, Jul 1988.

[36] F. Wang et al. The impact of incorporating shell-corrections to energy loss in silicon. *Nuclear Instruments and Methods in Physics Research Section A: Accelerators, Spectrometers, Detectors and Associated Equipment*, 899:1–5.

[37] D. Pohl. Pylandau 2.2.1. `https://pypi.org/project/pylandau/`, accessed February 16, 2023.

[38] G. Quast D. Savoiu. Karlsruhe Fit Environment - Fit examples, utilities, tips and tricks. `https://etpwww.etp.kit.edu/~quast/kafe/htmldoc/examples.html`, accessed June 4, 2023.

[39] CERN. The Proton Synchrotron. `https://home.cern/science/accelerators/proton-synchrotron`, accessed February 4, 2023.

[40] M. Alejandro Del Rio Viera. Transient Simulation Studies using TCAD and Allpix Squared. `https://indico.cern.ch/event/1232761/contributions/5320361/attachments/2631410/4551740/TANGERINEProjectTransientStudies.pdf`, accessed June 8, 2023.

[41] Silicon - electrical properties. `https://www.ioffe.ru/SVA/NSM/Semicond/Si/electric.html`, accessed June 8, 2023.

[42] BIPM, IEC, IFCC, ILAC, ISO, IUPAC, IUPAP, and OIML. Evaluation of measurement data — Guide to the expression of uncertainty in measurement. Joint Committee for Guides in Metrology, JCGM 100:2008.

[43] R. Diener et al. The DESY II test beam facility. *Nuclear Instruments and Methods in Physics Research Section A: Accelerators, Spectrometers, Detectors and Associated Equipment*, 922:265–286, apr 2019.

[44] Zaber Technologies Inc. X-RSW Series User's Manual. `https://www.zaber.com/manuals/X-RSW#m-14-specifications`, accessed June 6, 2023.

[45] G. Aglieri Rinella. Developments of stitched monolithic pixel sensors towards the ALICE ITS3. *Nuclear Instruments and Methods in Physics Research Section A: Accelerators, Spectrometers, Detectors and Associated Equipment*, 1049:168018, 2023.

Acknowledgements

First and foremost, I would like to thank Prof. Dr. Silvia Masciocchi for providing me with the outstanding opportunity to join the ALICE collaboration at CERN for my master's research phase and for supervising this thesis.

Further, I would like to thank my second corrector, Prof. Dr. André Schöning, for taking the time to read this thesis and for my time in his Mu3e team teaching me the essentials of working with silicon pixel detectors.

My sincerest thanks also to Dr. Magnus Mager for welcoming me in his R&D team at CERN and for entrusting me with the pioneering and challenging work on the DPTS.

I owe my gratitude to Dr. Miljenko Šuljić, who guided my research work at CERN and helped me to sort my thoughts in times of confusion.

Moreover, I acknowledge the whole ALICE ITS3 team, especially at CERN, Trieste and Heidelberg for the great and fruitful collaboration and for supporting my work.

Furthermore, I would like to express my heartfelt appreciation to all people who proofread this thesis and provided me with valuable feedback.

I would also like to thank my parents Dipl.-Ing. Ralf W. Menzel and Sabine M. Menzel for their love and support before and during the time of my studies.

Finally, I would also like to express my heartfelt appreciation to my partner Marie C. Mühlnikel for her love and encouragement.

Declaration

I certify that I have written this thesis independently and have not used any sources or aids other than those indicated.

Erklärung

Ich versichere, dass ich diese Arbeit selbstständig verfasst und keine anderen als die angegebenen Quellen und Hilfsmittel benutzt habe.

Heidelberg, den 08.07.2023,